POLITECNICO DI MILANO

Facoltà di Ingegneria Industriale

Corso di Laurea Magistrale in
Ingegneria Energetica

UNCERTAINTY QUANTIFICATION OF TURBULENT STATISTICS FROM HOT-WIRE MEASUREMENTS APPLIED IN A HIGH PRESSURE TURBINE STAGE

Relatore: Prof. Paolo Gaetani
Co-relatori: Dr. Fabrizio Fontaneto
Dr. Sergio Lavagnoli

Tesi di Laurea di:
Roberto Cosentino
matricola 824009

Anno Accademico 2015 – 2016

To my Mother, my Father
and the two women of my life, Cristina and Nataliia
for their support and encouragement

"*As far as the laws of mathematics refer to reality, they are not certain; and as far as they are certain, they do not refer to reality.*"
– Albert Einstein

Acknowledgements

Lots of people have left their trace on my path up to this intermediate step of my life; many of them have helped me overcoming all difficulties, others have made these difficulties even harder to deal with. I owe a *thank you* to all of them.

In particular, I owe a sincere gratitude to Professor Paolo Gaetani, whose lectures have been the reason because of which I wish to keep working in this fascinating field.

I owe a huge thanks to Fabrizio and Sergio for their advices and teaching at the Von Karman Institute for Fluid Dynamics. Thanks to them, not only I learnt academic concepts, but especially I've gained self-esteem.

During my time in Belgium at the VKI, I found an extremely friendly environment and the nicest people who were always ready to help and to guide me. Thank you, Elissavet, Giulia, Bogdan, Diego, Ruzbeh and Mauro.

The VKI would have never been the same without *Little Italy*, among which a particular thanks goes to Alessandro *Bella Vita*.

In these last years I spent at Polimi, I met not only journey companions but real friends. There will always be time for a beer with you, Enrico, Simone, Mario and Rachele.

Finally the biggest acknowledgement goes to my family: my parents, my sister, Nataliia, you all have been and will be sails in windy days and harbour during storms. Thanks to all my uncles, aunts and those crazy folks of my cousins, the only who were and will always be there, no matter what.

Ad Maiora!

Sommario

Il presente progetto di tesi si colloca nell'ambito di una più ampia campagna sperimentale condotta dal Von Karman Institute for Fluid Dynamics (VKI) per la valutazione delle performance aerodinamiche e termodinamiche di uno stadio di turbina di alta pressione al fine di testare diverse geometrie dell'apice delle pale.

Gli obbiettivi specifici del lavoro svolto sono la caratterizzazione dell'inlet della turbina in termini di grandezze turbolente, quali turbulence intensity, length scales e spettri turbolenti, e lo sviluppo di uno studio statistico non parametrico per la valutazione dell'incertezza delle grandezze misurate col fine di conferire ai parametri turbolenti accurati intervalli di confidenza.

Lo stadio di alta pressione di una turbina rappresenta uno dei componenti più onerosi di un moderno turbo-gas. La ricerca attuale è volta, infatti, allo sviluppo di motori sempre più efficienti che permettano la riduzione di costi e di emissioni di CO_2. Per raggiungere questo obiettivo si mira all'ottenimento di temperature di ingresso in turbina sempre più elevate e di riduzione di perdite aerodinamice, soprattutto riguardanti il tip-leakage.

Per testare performance aerodinamiche e, soprattutto, per simulare lo scambio termico nelle condizioni rappresentative di un turbo-gas, si ricorre spesso a blow-down test rigs. La transient CT3 facility del VKI opera secondo il principio dell'isentropic light piston compression tube. Quando il flusso viene rilasciato nella test section, esso si stabilizza per circa 0.15 secondi, nei quali il segnale viene acquisito e post-processato.

Le misurazioni del campo di velocità sono state effettuate grazie a un hot-wire anemometry in configurazione single-probe, ipotizzando che il flusso sia prettamente monodimensionale all'ingresso dello stadio di turbina.

L'uso dell'hot-wire risulta essere più problematico nella CT3 rispetto a un test-rig a ciclo chiuso, che garantisce un flusso con intervalli di stabilità di gran lunga superiori. Inoltre, la temperatura totale del flusso è soggetta a grandi variazioni durante le misurazioni. Per questo motivo la calibrazione dell'hot-wire deve essere adeguata per permettere la riduzione dei dati in condizioni di flusso instabile e fortemente non isotermo. La metodologia utilizzata è stata sviluppata presso il VKI (Chukurel 2012) e consiste in un'analisi adimensionale del principio fisico che

guida il funzionamento dell'hot-wire, ovvero lo scambio termico.

L'hot-wire è operato secondo il principio di Constant Temperature, per cui la temperatura del filo è mantenuta costante da un feedback amplifier ad alta risposta in frequenza che reagisce a una variazione della potenza di raffreddamento del flusso che circonda il filo caldo. Il bilancio energetico dello scambio termico in condizione di temperatura costante è uguale a

$$\frac{\mathrm{E}_w^2}{\mathrm{R}_w} = \pi l_w d_w h\big(\mathrm{T}_w - \eta \mathrm{T}_0\big) \tag{1}$$

dove E_w è il voltaggio ai capi del filo, per cui la potenza termica ceduta dal filo al flusso è uguale alla potenza elettrica circolante nel filo. Di conseguenza, essendo la temperatura del filo T_w e, quindi, la sua resistenza R_w costante, una variazione di scambio termico tra fluido e filo è letta in output come una variazione di bridge top voltage.

Lo scambio termico al sensore può essere trattato con un'analisi dimensionale esprimendo il numero di Nusselt Nu come funzione delle fluttuazioni di voltaggio e della temperatura totale del flusso.

$$Nu = \frac{\mathrm{E}_b^2}{\mathrm{T}_w - \eta \mathrm{T}_0} \frac{\mathrm{R}_w}{\pi \kappa l_w \big(\mathrm{R}_t + \mathrm{R}_l + \mathrm{R}_w\big)^2} \tag{2}$$

Le fluttuazioni in termini di voltaggio, e quindi in termini di Nusselt, sono poi correlate a fluttuazioni di velocità, e quindi turbolenza, tramite un fitting polino-

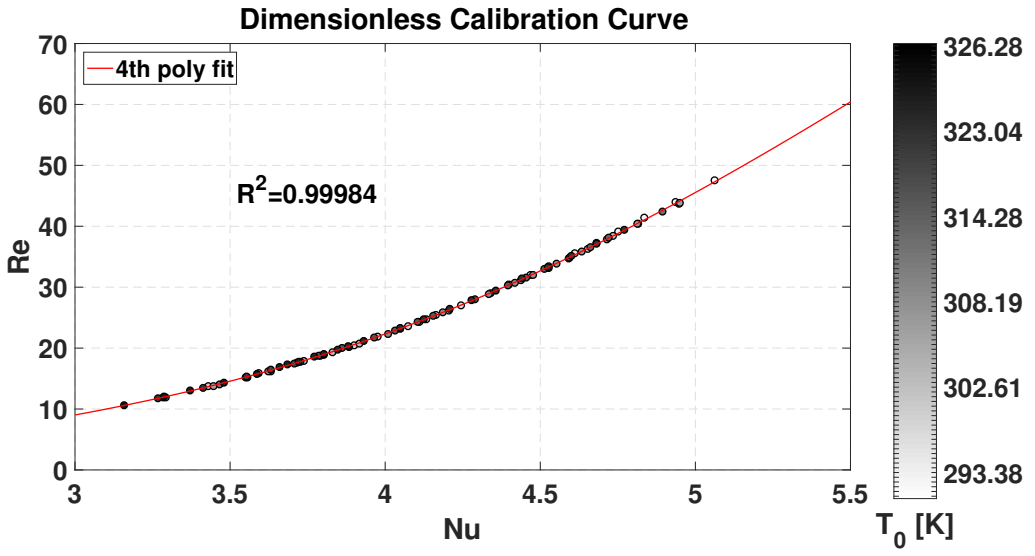

Figure 1: Curva di calibrazione dell'hot-wire

miale al quarto ordine sul piano Nu-Re (figura 1). L'analisi dimensionale permette di utilizzare un'unica curva di calibrazione per condizioni di flusso fortemente non isoterme, al contrario della ormai nota King's Law che è valida solo per flussi isotermi. Inoltre, questa metodologia permette di evitare una calibrazione in-situ e di operare su un jet freddo, purchè le condizioni di similitudine con quelle attese in facility vengano rispettate.

Una volta effettuata la calibrazione, l'hot-wire è stato inserito all'interno della facility a monte della NGV (Nozzle Guide Vane) come mostrato in figura 2. I test effettuati all'inlet della turbina di alta pressione hanno evidenziato un andamento lungo lo span della pala, per quanto riguarda turbulence intensity e integral length scales, come in figura 3.

La turbulence intensity raggiunge il suo massimo in prossimità della parete (intorno al 5÷10% e 90÷95% dello span) a causa della maggiore anisotropicità del flusso e a causa dell'interazione tra flusso principale, strutture vorticose e strato limite che si traduce in un elevato sforzo di taglio in quella zona. La length scale è valutata a partire dallo spettro turbolento calcolato tramite Fast Fourier Transform (FFT). Il massimo cade in un intorno della metà dell'altezza di pala (0.03 m) e rappresenta la massima lunghezza caratteristica delle più grandi strutture vorticose del flusso.

Per fornire un riferimento affidabile alla CFD (Computational Fluid Dynam-

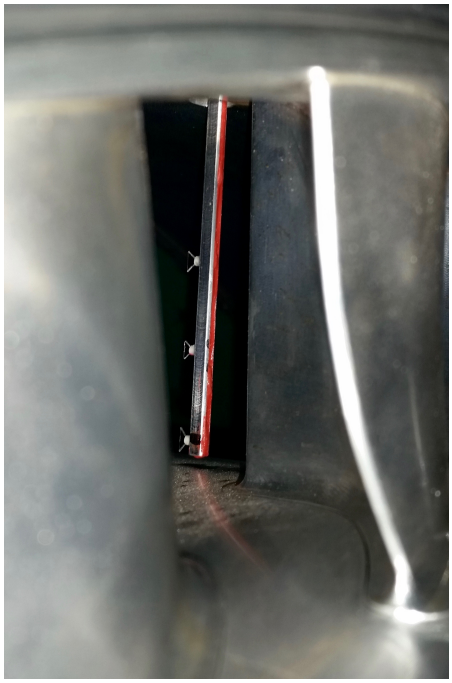

Figure 2: Sensore hot-wire inserito all'ingresso dello stadio di turbina

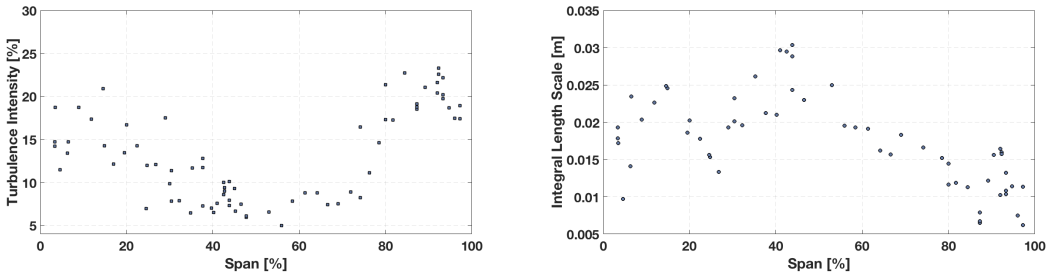

(a) (b)

Figure 3: Turbulence Intensity (a) e Integral length scale (b) lungo l'altezza di pala

ics), i dati forniti devono, quindi, essere accompagnati da una buona analisi dell'incertezza delle misure effetuate. Quando, però, si ha a che fare con grandezze turbolente, si ricorre spesso ad assunzioni più o meno forti sulla loro distribuzione statistica.

I parametri turbolenti sono, a tutti gli effetti, momenti statistici di ordine $k \geq 1$, per cui non si conosce a priori una distribuzione di probabilità. Comunemente, si ipotizza che le statistiche turbolente seguino una funzione di probabilità Gaussiana per cui il teorema del limite centrale è valido. Questa è una forte assunzione, specialmente per campionamenti con un alto grado di correlazione e, spesso, porta a sottostimare gli intervalli di confidenza.

Il presente lavoro di tesi, invece, propone l'uso di un metodo statistico, introdotto in principio in campo econometrico (Efron 1979), noto come Bootstrap. In questo caso è stata utilizzata la versione Moving Block Bootstrap (Künsch 1989), più adeguata al trattamento di campioni correlati tra loro. Questa versione permette infatti di preservare l'autocorrelazione, informazione importante per le grandezze turbolente.

Il metodo consiste in un ricampionamento casuale delle osservazioni acquisite con l'hot-wire. Il set di dati originario viene ricomposto un determinato numero di volte e la statistica di interesse è calcolata per ognuna delle serie ottenute.

Il metodo è basato sull'assunzione che se il campionamento rappresenta una buona approssimazione della reale distribuzione della popolazione originaria, allora la serie *bootstrappata* è una buona approssimazione della distribuzione dei campionamenti. Più formalmente, se il numero di campionamenti N è sufficientemente grande, al crescere del numero di serie ricostruite B, la stima della distribuzione ottenuta dalla serie *bootstrappata* tende asintoticamente alla distribuzione dei campionamenti originali.

La figura 4 descrive il procedimento per la realizzazione delle serie *bootstrappate*. La serie originaria è ricampionata in modo random, attraverso un metodo simile

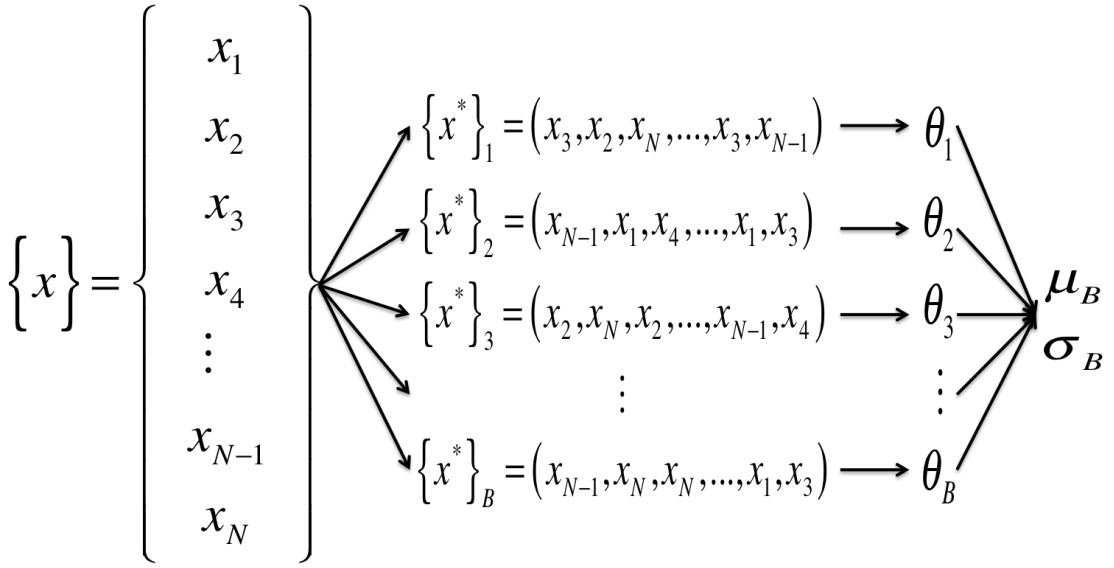

Figure 4: Procedura per la costruzione della serie *bootstrappata*

al Monte-Carlo, B volte. Per ogni serie ricostruita, la statistica di interesse θ è calcolata e dai B valori di θ, la distribuzione può essere stimata costruendone l'istogramma. Da esso la media e la deviazione standard possono essere calcolate.

Il MBB genera le B serie muovendo i campioni in blocchi di lunghezza b. I blocchi devono essere lunghi a sufficienza da mantenere la correlazione dei campionamenti intatta.

Una volta ottenuta la distribuzione *bootstrappata*, è possibile ricavare l'inferenza statistica in due modi diversi:

1. Attraverso una tabella simile a quella della distribuzione di Student-t, per cui per ogni serie si calcola un errore standard e si costruisce la distribuzione dell'errore stesso. In questo modo è possibile costruire la funzione pivotale da cui si ricavano gli intervalli di confidenza

2. Attraverso il metodo delle percentuali, per cui si prendono i valori limite della distribuzione cumulativa delle statistiche *bootstrappate*. Questi valori limiti rappresentano gli intervalli di confidenza

Il secondo metodo è più semplice e non ha bisogno di calcolare l'errore standard, la cui formulazione analitica non è presente in letteratura per momenti statistici di ordine elevato, come le length scales. Lo svantaggio del secondo metodo è che dà una buona stima dell'errore solo se la distribuzione *bootstrappata* è simmetrica, al contrario del primo metodo.

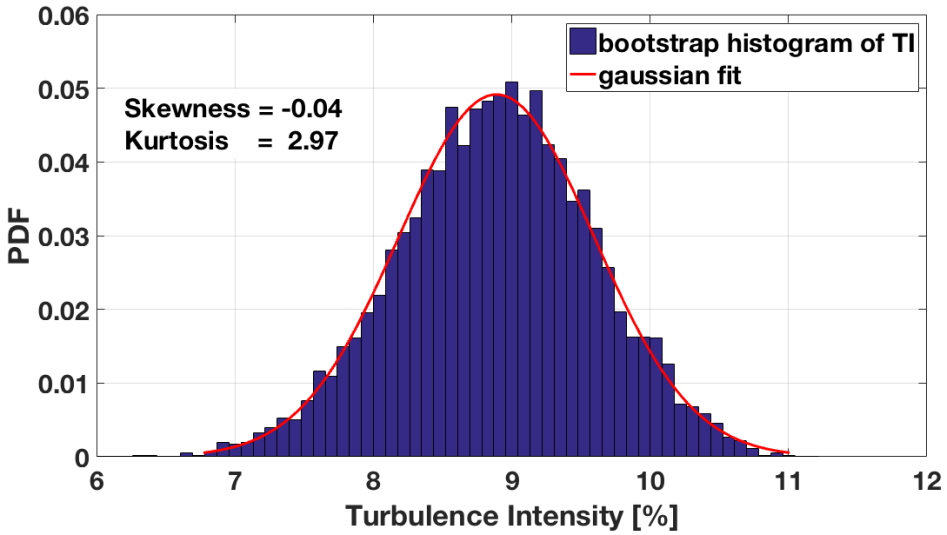

Figure 5: Istogramma della Turbulence Intensity *bootstrappata*

Le grandezze calcolate durante il progetto di tesi hanno mostrato una tendenza asintotica alla normalità al crescere di B, come rappresentato, a titolo di esempio, nella distribuzione della turbulence intensity in figura 5. Data la simmetria riscontrata, risulta più immediato calcolare l'inferenza statistica con il secondo metodo descritto (metodo delle percentuali) da cui è possibile ricavare gli intervalli di incertezza al 95% di livello di confidenza.

Nonostante sia preferibile una ulteriore verifica con un metodo non parametrico più validato, come per esempio il metodo Monte-Carlo, il presente lavoro ha dimostrato che il bootstrap è un metodo efficace e potente per il calcolo dell'inferenza statistica per grandezze turbolente quali integral length scale, micro length scale e turbulence intensity. Queste sono a tutti gli effetti momenti statistici di ordine superiore al primo, di cui non si conosce a priori una distribuzione di probabilità. Essendo un metodo non parametrico, non è stata necessaria alcuna ipotesi sulla stessa distribuzione, che viene ricostruita grazie alle proprietà asintotiche del Bootstrap descritte in precedenza.

Parole Chiave

Turbina AP; turbolenza; hot-wire anemometry; incertezza; statistiche turbolente; bootstrap; moving block bootstrap.

Abstract

The present work aims to characterize the flow field at the inlet of a high pressure (HP) turbine stage in terms of turbulence parameters such as turbulence intensity, time and length scales and turbulent spectra. Furthermore, a non-parametric statistical approach is proposed in order to confer all turbulent statistics with error bars representing 95% confidence intervals.

In order to test aerodynamic and thermal performance in engine representative conditions, the Von Karman Institute (VKI) CT3 blow-down test rig is used, operating with the principle of isentropic light piston compression tube.

Hot-wire anemometry (HWA) technique is employed to acquire velocity signal up to high frequency fluctuations representing the smallest scales of a turbulent flow. However, due to the step-wise evolution of temperature and pressure in blow-down facilities and due to the not feasibility of the flow to maintain a stable condition for a large time period (the test time in CT3 wind tunnel is around 0.15 seconds), the use of HWA is not simple. A non dimensional calibration technique (Cukurel 2012) allows to reduce HWA data also for strongly non-isothermal flows with a single curve fit.

For measurements concerning turbulence, the parameters of interest are high order statistical moments, for which no conventional methods are available in order to quantify their uncertainty. The objective of this thesis is to present a standard method for the estimation of uncertainties of turbulent statistics by means of a re-sampling technique, the Moving Block Bootstrap (MBB). Thanks to this non-parametric approach, based on a straightforward algorithm, it is possible to perform statistical inference on high order moments without any assumption on their distribution.

The blocks length is selected either by an automatic algorithm (Politis 2004) or by a sensitivity analysis. The latter method resulted to perform better for highly correlated structures and for flow presenting a high oscillating autocorrelation function around zero.

Keywords

HP turbine; turbulence; hot-wire anemometry; uncertainty; turbulent statistics; high order statistical moment; bootstrap; moving block bootstrap.

Contents

Acknowledgements **iii**

Sommario **v**

Abstract **xiii**

List of Figures **xvii**

List of Tables **xix**

List of Symbols **xxi**

1 Introduction **1**
1.1 Motivation 1
1.2 Objectives 3
1.3 Background 4
1.3.1 State of the Art for Turbulence Measurement 4
1.3.2 Uncertainty in Turbulence 6

2 Hot-Wire Calibration **9**
2.1 Physical Principle of Operation 9
2.1.1 Constant Temperature Anemometry 10
2.2 Mass Flux Calibration 11
2.3 Calibration Set-Up 15
2.3.1 The Dantec Anemometer Frame 15
2.3.2 The Hot-Wire Probe 16
2.3.3 Total Temperature and Total Pressure 17
2.3.4 The National Instrument Acquisition System 17
2.4 Calibration Methodology 18
2.4.1 The Effective Wire Temperature T_w 22
2.5 Results 23
2.6 Validation 25

3 Measurement Campaign **29**
3.1 The VKI Anular Cascade Facility CT3 29
3.2 Plane 1 Set-Up 35
3.3 Post Processing 36

4 Results and Discussion **43**
4.1 Statistical Description of Turbulence 43
4.2 Inlet Characterisation 47
4.3 Time and Length Scales 50

5 Uncertainty Analysis **57**
5.1 Calibration Uncertainty 59
5.2 Measurements Uncertainty 62
5.2.1 General Principle of Bootsrtapping 64
5.2.2 The Moving Block Bootstrap 68
5.2.3 Bootstrapped Confidence Interval 74
5.2.4 Uncertainty Results 75

6 Conclusions **79**
6.1 Future Recommendation 80

A Appendix A **81**
A.1 Thermocouple Uncertainty 81
A.2 Validyne Pressure Transducer Uncertainty 82
A.3 Error Propagation Analysis for Hot-Wire Calibration 83

References **87**

List of Figures

2.1 Constant Temperature Anemometry (CTA) 11
2.2 CFD prediction for Reynolds and Mach number at stator inlet . . . 13
2.3 Range of T_0 and Mach number for Reynolds similitude in hot-wire calibration 14
2.4 Dantec CTA frame 15
2.5 The DAO111A hot-wire probe 16
2.6 Validyne amplifier with differential pressure transducer (a) and Thermocouple amplifier with K-type thermocouple (b) 17
2.7 16-bit National Instrument Acquisition System 18
2.8 Schematic of the Calibration Jet Facility 19
2.9 DPI 610 pressure calibrator pump (a) and Thermibel oil bath (b) . 20
2.10 Validyne calibration curve for total pressure measure (a) and Thermocouple calibration curve for total temperature measure (b) . . . 20
2.11 Raw calibration data cloud 23
2.12 R-square evolution with guessed wire temperature 24
2.13 Collapsed data in a single curve 24
2.14 Probe location with respect to the nozzle 25
2.15 Time resolved measurements at different probe position for $M = 0.095$ 26
2.16 Power Spectral Density for different probe position and $M = 0.095$. 27

3.1 Picture of the VKI's CT3 facility 31
3.2 Stator (a) and Rotor (b) of the VKI's CT3 facility 31
3.3 General layout of the VKI's CT3 facility 32
3.4 Test Section of VKI's CT3 facility with measurements location . . . 33
3.5 Evolution of $T_{0,1}$, $p_{0,1}$, p_{tube} and rotational speed in a typical test sequence 34
3.6 Plane 1 Set-Up and Instrumentation 36
3.7 Total Pressure sequence and signal fraction used for the post processing 37
3.8 Hot-wire raw voltage signal during the blow down 38
3.9 Normalized total Temperature along the Span 39

3.10 Total Temperature sequence during a test for different rakes 39
3.11 Comparison between two methodology of total Temperature computation 40
3.12 Velocity comparison between the one computed by the hot-wire and the one computed by pneumatic rakes 41

4.1 Typical turbulent spectra 45
4.2 Mean Velocity distribution along the blade height 48
4.3 Turbulence Intensity distribution along the blade height 49
4.4 Autocorrelation factor 51
4.5 Power Spectral Density and the averaged energy at frequency tending to zero for integral time scale computation 53
4.6 Integral Length Scale distribution along the blade height 54
4.7 Micro Length Scale distribution along the blade height 55

5.1 Deviation of calibrated points from the fitting calibration curve . . 60
5.2 Hot-wire calibration curve with 95% confidence level 62
5.3 Histogram of velocity samples 63
5.4 Skewness of velocity samples distribution along the span 63
5.5 Principle of Bootstrap re-sampling technique 67
5.6 Mean and Standard Deviation of Turbulence Intensity depending on the number of Bootstrap series 68
5.7 Skewnees and Kurtosis of Turbulence Intensity depending on the number of Bootstrap series 69
5.8 Histogram of bootstrapped mean velocity 70
5.9 Histogram of bootstrapped turbulence intensity 70
5.10 Mean of Integral Length Scale sensitivity depending on the Bootstrap blocks' length relative to an original signal sampled at 1 Mhz for the 0.1 seconds of test resulting in 100000 samples 72
5.11 Histogram of bootstrapped Integral Length Scale 73
5.12 Histogram of bootstrapped Micro Length Scale 73
5.13 Mean Velocity distribution along the blade height with its uncertainty at 95% confidence level 76
5.14 Turbulence Intensity distribution along the blade height with its uncertainty at 95% confidence level 76
5.15 Integral Length Scale distribution along the blade height with its uncertainty at 95% confidence level 77
5.16 Micro Length Scale distribution along the blade height with its uncertainty at 95% confidence level 77

List of Tables

2.1 Nominal inlet flow condition predicted with CFD for some characteristic points of the Span 12
2.2 Comparison between mean velocity measured by hot-wire at different wire positions and by pneumatic quantities at the nozzle exit . . 26

3.1 Similarity test condition at midspan 33

5.1 Comparison between Student-t distribution and percentile Bootstrap to compute confidence interval with 95% confidence level for mean velocity, turbulence intensity, integral and micro length scale . 75

List of Symbols

Acronyms

CFD	Computational Fluid Dynamics
CTA	Constant Temperature Anemometry
DNS	Direct Numerical Simulation
FFT	Fast Fourier Transformation
HW	Hot-Wire
HWA	Hot-Wire Anemometry
LDA	Laser Doppler Anemometry
MBB	Moving Block Bootstrap
NS	Navier-Stokes
PDF	Probability Density Function
PSD	Power Spectral Density
PIV	Particle Image Velocimetry
TI	Turbulence Intensity
TKE	Turbulent Kinetic Energy
VKI	Von Karman Institute (for fluid dynamics)

Dimensionless numbers

Gr	Grashof number
Kn	Knudsen number
M	Mach number
Nu	Nusselt number
Pr	Prandtl number
Re	Reynolds number
St	Strouhal number

Roman symbols

c	Specific heat	$J/(kgK)$
E	Voltage	V
E	Spectral Energy	$(m/s)^2/Hz$
f	Frequency	Hz
L	Integral length scale	m
h	Convective heat transfer coefficient	$W/(m^2K)$
p	Pressure	Pa
P	Electrical Power	W
Q	Heat Power	W
R	Resistance	Ω
R	Gas constant	$J/(kgK)$
t	Time	s
T	Temperature	K
T	Integral time scale	s
T_u	Turbulence Intensity	%
U	axial-component of velocity	m/s
U	Uncertainty	$various$
V	Velocity	m/s

Greek symbols

α	Temperature coefficient of resistance	-
γ	Heat capacity ratio	-
ϵ	Rate of dissipation of TKE	m^2/s^3
η	Temperature recovery factor	-
η	Kolmogorov length scale	m
λ	Micro length scale	m
μ	Dynamic viscosity	Pas
μ	Statistic mean value	$various$
ν	Kinematic Viscosity	m^2/s
κ	Thermal conductivity	$W/(mK)$
ρ	Density	kg/m^3
σ	Standard deviation	$various$
ϕ	Flow angle	$^\circ$
τ	Kolmogorov time scale	s
τ	Over-heat factor	-

Sub- and Superscripts

ad	adiabatic
eff	effective
hw	hot-wire measure
n	normal direction
$pneum$	pneumatic measure
ref	reference
w	wire
0	stagnation property
95	with 95% confidence level
$'$	fluctuating component

Chapter 1

Introduction

1.1 Motivation

Gas turbines provide propulsion to most of the modern aircraft and drive a large share of world's power unit. These are mainly fossil-fuel based and will keep their central position for many years and decades in both aircraft powering and global energy production. This and the actual needs for reducing carbon dioxide emissions has led to endeavours by researchers all over the world to find new technologies and methodology of designs to improve efficiency.

Blow-down test rigs are often used in order to test aerodynamic and, especially, thermal performances of turbo-machinery under engine representative condition. Current researchers' efforts to improve efficiency are focused on new highly performing designs of high pressure (HP) turbine stage, which is one of the most critical component of the engine due to the highly hostile flow field.

Although efficiency increase may be achieved through a combination of methods, one of the most significant is to increase the turbine inlet temperature (TIT), which may reach in modern turbines values higher than 1800 K and there is a continuous push to increase it.

Furthermore, the flow field within high pressure (HP) turbine passages is quite complex, involving strong secondary flows and transverse pressure gradients, which are even more affected by necessary cooling systems. These events strongly alter the aerodynamic efficiency. For instance, one of the most important aerodynamic losses in HP turbines is due to the tip flow-leakage.

Therefore, for both energy production and aviation industries, gas turbine designers have to face many aspects in the design process, in which the HP turbine stage represents one of the most challenging components. Indeed, increasing efficiency of the high pressure stage has a significant influence on the overall efficiency of the engine.

At the inlet of HP turbine stages, the flow is typically highly turbulent and unsteady. It is, thus, difficult as well as essential to have a detailed knowledge of the flow field. Concerning the heat transfer, wide varieties of factors are deemed to contribute to the complexity of this phenomena inside a turbo-machine, e.g. combustor exit hot streak, unsteadiness, rotational effects, and mainstream turbulence.

In order to help the design process, aerodynamic and thermal investigations are essential to obtain useful informations about the flow physics and to gain knowledge about the complex relation and interaction between turbulent flow-field, heat transfer and turbine efficiency. Nowadays, computational fluid dynamics (CFD) has been widely used in order to provide a large number of data and flow characteristic which would not be possible to obtain otherwise. Nevertheless, although many primary designs can be achieved with a good level, many aspects concerning turbulent flows inside a complex geometry and flow structure as the one through a turbo-machine can not be solved even with the most powerful computers available. Indeed, when it is required to simulate a turbulent flow field, this is commonly modelled based on Reynolds Averaged Navier Stokes equations (RANS). Although these models may be advanced, they are still far from being completely reliable. Only Direct Numerical Simulation (DNS) of Navier-Stokes (NS) equations gives an accurate prediction of all quantities for the totality of turbulent flows, however high computational cost is required and only few calculators in the world can afford it for complicated geometry and flow conditions. Furthermore, even DNS models are very sensitive to boundary and initial conditions and must be validated with experiments. Therefore, experimental investigations still remain a priority for better understanding the flow physics.

The main and most known consequences of turbulence in turbo-machines are related, among the others, to [1]:

- Boundary layer interaction along the blade, leading to a more energized flow near walls and, hence, to a delay in detachment;

- Enhance in mass and heat transfer between the flow and a solid surface, due to a higher mixing of the flow;

These aspects are of paramount importance for turbo-machine efficiency and, in order to be accurately simulated, a thorough experimental investigation is required. Hence, the main purpose of an experimental campaign is to validate CFD codes used for design analysis or to improve brand new concept of design as well as to provide accurate boundary conditions for simulating models.

1.2 Objectives

This project is part of a broader research activity carried forward the Von Karman Institute for Fluid Dynamics (VKI) and supported by SNECMA S.A., the final goal of which is the experimental analysis of the aero-thermal performance of a high-pressure turbine stage with particular interest in validating and verifying different geometries of the blade tip. Indeed, one of the most important limiting factor in high pressure turbine efficiency is the tip leakage flow. The spilling fluid crossing the pressure side to the suction side causes aerodynamic losses due to the lower effective flow which participates to the power extraction process. Moreover, the flow leaving the upper part of the blade meets the main passage stream causing higher mixing losses due to different momentum and orientation.

The results achieved in the experimental campaign have the twofold purpose of providing accurate boundary conditions for CFD codes and useful references for their validation as well as verifying the best geometry of the blade tip in order to minimize aerodynamic losses and improving heat transfer performance.

The specific aim of the work is intended to gain a detailed characterization of turbulence at the inlet of the turbine, which is located downstream of a piston and a shutter valve as described in chapter 3. Particular attention is paid to the evaluation of parameters such as turbulence intensity, length and time scales, and turbulent spectra. These quantities are of paramount importance in CFD simulations due to the high sensitivity of available models on boundary conditions.

High free upstream turbulence is an interesting condition when dealing with high pressure turbine for both thermal and aerodynamic performances. Indeed, tip leakage vortex diffuses very quickly under a high inlet turbulence intensity, resulting in a very weak tip leakage vortex and less losses [2], while temperature of the blades and of the casing wall reduces for high turbulence level due mainly to the better distribution of temperature along the channel height [3].

In order to perform the measurements of upstream turbulence, hot wire probes are used in parallel with pneumatic probes for comparison purpose. Given the high flows temperature dependence on hot wires results, a novel calibration technique was used, developed by Cukurel [4] and Acarer [5] at VKI.

An experimental investigation is complete and represents a valid reference to CFD codes only if the data provided are accurate and accompanied by a detailed confidence interval. This project has the ambition to fill the gap in accurate uncertainty quantification for turbulent statistics in the turbo-machinery field. Since classical statistic formulations are no more suitable for correlated observations, a new statistical approach to hot-wire measurements in a turbo-machinery field is provided.

The thesis is structured as follows: at first there is a description of the instrumentations and facility utilized, then the results are shown and finally the statistic

approach to the measurement is described and the results are provided with an accurate uncertainty analysis.

Chapter 2 gives a thorough description of the set-up used for the hot-wire's calibration and the methodology applied.

In **chapter 3**, the VKI high-pressure wind tunnel CT3, utilized for the measurement, is described. Furthermore, the methodology applied for the data reduction is defined.

In **Chapter 4** the results in terms of turbulence parameters are presented and discussed.

Chapter 5 discusses the most critical part of the project: the uncertainty quantification of both calibration results and measured quantities. Uncertainty in the final results passes through a meticulous analysis of all possible errors concerning instrumentations precision, quality of probes calibration, etc. Finally, the turbulent statistics are conferred with adequate confidence level.

Conclusions are reported in **Chapter 6** together with future recommendations.

1.3 Background

1.3.1 State of the Art for Turbulence Measurement

Over the last years, computational fluid dynamics (CFD) witnessed a great improvement in both computational cost and prediction methods for turbulence yielding a need for development of measurement techniques, the results of which must be as much accurate as possible.

Enhances in experiments are directed to provide complete description of phenomena not entirely known, such as boundary layer, flow separation and vortex interaction, as well as to equip CFD codes with reliable database for overall aerodynamic parameters and turbulent statistics [6].

In order to achieve these requirements, measurements methods must meet certain characteristics, these are

- High Frequency Response;
- High Spatial Resolution;
- Small or none interference with the flow (non-intrusive instrument).

Several instruments and techniques are available in order to measure fluctuating velocities, which can be classified in different categories. For a full review of the techniques refer to Meng et al [7]. Among the others, the most validated are:

- Optical techniques

- Pressure based techniques
- Hot-wire anemometry

Optical Techniques

Laser Doppler Anemometry (LDA) and Particle Image Velocimetry (PVI) belong to the first category. Both techniques need seeding particles which represent the only disturbance in the flow. However, in case of excessive seeding or of not fine enough particles, the turbulence may be suppressed and underestimated.

LDA utilises the Doppler shift in a laser beam to calculate velocity in a transparent fluid, in which tracing particles or a fluid of contrast is added. The shifted beams are crossed at their focal points; when the particles pass trough the fringes, the laser light is reflected. The knowledge of the incident and reflected beam light balance determines the fluctuating frequency.

The main advantage of LDA is that no calibration is needed and it is characterized by a sufficiently high spatial and temporal resolution. On the other hand, the use of LDA in hostile environment such as the one of turbo-machinery is not always applicable due to the necessity of optical access. The signal is sensitive to acoustic noise, mechanical vibration and varying temperature [8]. Furthermore, since the LDA measures the velocity of the particle rather than the fluid velocity, the accuracy is limited by the accuracy with which these particles follow the main flow.

The PIV is a similar technique, making use of seeding particles to track the flow velocity magnitude and direction by photographing the particles at specific time intervals. A PIV device consists of a digital camera, a laser designed to illuminate a specific area of the flow field and an external trigger.

The advantage of PIV is the multi-dimensional characterization of the flow, which is fundamental in turbo-machinery application, in which the flow is strongly unsteady and three-dimensional. Then again, the main drawback for turbo-machinery purpose is the need for optical access, aside from the fact that very small particles have to be used in order to track the flow with a high enough accuracy.

Pressure Based Techniques

Aerodynamic probes consist of a cylindrical body with one or several holes at the probe tip, which are connected to pressure sensors, e.g. pressure transducer. The signal is acquired by an acquisition system, then voltage and pressure are linked by a dynamic calibration, allowing to compute the flow velocity and direction. Particular type of pressure probe is the Pitot tube which allows to measure velocities by means of Bernoulli principle, measuring the static pressure – when the fluid

enters the tube – and the total pressure – when the fluid comes to rest inside the tube – as

$$V = \sqrt{\frac{2(p_0 - p)}{\rho}} \tag{1.1}$$

The main advantages are the low cost and the high durability. For these reasons, it is still often used in turbo-machinery applications and wind tunnel industries. Drawbacks are the flow interference and the low frequency response, unless specific design of the probes is provided. This limits the use of Pitot tube when turbulence is the main subject of interest.

Hot-Wire Anemometry

High frequency response and high spatial resolution are typical advantages of hot-wires, beside a low cost and an apparently straightforward working principle. On the other hand, fragility and flow interference constitute the main disadvantages.

Improvement in turbo-machinery, that is higher efficiency and higher complexity in blade design, is the result of a deep knowledge of the flow field, which is highly three-dimensional and unsteady. Time-resolved measurements are therefore essential in order to fully understand the physical phenomena in the flow path. Hot-wires are not only suitable for time-resolved measurements but represent the flagship for turbulent flows experiments.

Indeed the hot-wire anemometry (HWA) is one of the most widespread techniques in flow measurements, thanks to its high spatial resolution and frequency response. HWA is the only instrument that delivers an analogue output as representation of velocity up to high frequency fluctuations [9].

As stated by Bruun [10], typical advantages of hot-wires anemometry with respect, for instance, to a Laser Doppler Anemometry (LDA) are the low cost, the high frequency response up to 20-50 kHz, the wide velocity range (up to high compressible flow), the high accuracy and resolution and the high signal-to-noise ratio.

On the other hand, the use of hot-wire probes (HW) is limited to moderate turbulence intensity flow due to the so called *rectification error* [10], for which the wire is not sensitive to recirculation flows. Furthermore, in contrast with LDA or Particle Image Velocimetry (PIV), the HW is an intrusive instrument, hence it causes a disturbance in the flow.

1.3.2 Uncertainty in Turbulence

Measured data are fully meaningful only if accompanied by a complete uncertainty analysis of measured quantities and the understanding of its impact in a CFD

validation process.

There are two main approaches to quantify error sources: one is the ISO Guide to the expression of Uncertainty in Measurement (GUM) and the second is the ASME methodology. The first one divides error sources in two groups, Type A for all kind of errors deriving from experimental observations and Type B for an estimate of an input quantity that has not been obtained from repeated observations. The ASME methodology provides a more straightforward partition of uncertainty sources: random error sources classified by the standard deviation of observed realizations and systematic error sources referring to those which provide bias from the true value and does not affect the population distribution.

In experimental investigations there are two main error sources to take into account, that is the uncertainty in instruments and measurement methods and, more difficult to quantify, the uncertainty resulting from the data reduction of statistical quantities of high order moments [6].

In an experimental campaign concerning turbulence, the parameters of engineering interest are: turbulent intensity (T_u), turbulent kinetic energy (TKE), rate of dissipation (ϵ), time and length scales of the energy containing eddies (T and L) and smaller scales (τ and η), such the Kolmogorov one, related to sub-inertial and dissipative-viscosity effects.

The most common approach in dealing with turbulent flow is to assume a Gaussian distribution for which the central limit theorem is valid and simple formulations for higher order statistical moments can be applied.

In classical statistic, the central limit theorem, described by Moivre in 1733 but erroneously ascribed to Gauss, attributes the normal distribution to uncorrelated, random repetitions. The normal distribution function is

$$f(x) = \frac{1}{\sqrt{2\pi\sigma}} e^{\frac{-(x-\mu)^2}{2\sigma^2}} \tag{1.2}$$

where μ and σ are respectively the mean and the variance of the variable x of interest.

Turbulent flows are chaotic but a certain degree of correlation between structures in time and/or in space is present, proving the existence of a deterministic nature of turbulence. This means that turbulent statistics should not be handled as completely random data; hence, when dealing with turbulent flow phenomena, in view of providing as reliable as possible data, different post-processing strategies must be applied, which are not making use of classical statistics.

Nevertheless, there are few works in the field of uncertainty quantification of turbulent statistics and most of them use the Gaussian distribution assumption (see section 5.2).

One of the aims of this project is to give an accurate confidence level in turbulent statistics (with particular attention for the turbulence intensity and length

scales) of the measurements performed at the inlet of a blow-down, high-pressure turbine facility operated at a low velocity level, in order to provide a useful reference for CFD codes and their validation.

Chapter 2

Hot-Wire Calibration

2.1 Physical Principle of Operation

The hot-wire consists of a thin heated cylinder (the typical sensor is 5 or 9 μm in diameter) invested by a flow with which it exchanges heat by means of the principle of forced convection. Thus, the heat transfer depends on both fluid and flow properties, that is density ρ, viscosity μ, conductivity κ, specific heat c_p, and, velocity V, temperature of the flow T and of the wire T_w and pressure p [10].

The heat transfer in an electrically heated wire can be modeled in a simplified way neglecting radiation as [11]:

$$\frac{d\big(c_w \mathrm{T}_w\big)}{dt} = \mathrm{P} - \mathrm{Q} \tag{2.1}$$

where, c_w is the specific heat of the wire, P is the electrical power supplied by the anemometer to the wire and Q is the heat transferred by convection to the flow. The first term on the left-hand side of the equation represents the stored heat in the wire by means of the wire thermal inertia.

By the definitions of convective heat transfer for a cylinder in cross-flow and of electrical power, equation 2.1 can be rewritten as

$$\frac{d\big(c_w \mathrm{T}_w\big)}{dt} = \frac{\mathrm{E}_w^2}{\mathrm{R}_w} - \pi l_w d_w h\big(\mathrm{T}_w - \mathrm{T}_{adw}\big) \tag{2.2}$$

with R_w being the resistance of the wire, E_w the voltage among the wire endings, l_w and d_w are respectively the wire length and diameter, h is the convective heat transfer coefficient, and T_{adw} the adiabatic film temperature, that is the effective flow temperature *felt* by the wire in the heat transfer process and is equal to $\eta \mathrm{T}_0$, where η is the recovery factor formulated by Dewey [12].

The recovery factor is a function of the Mach number and the Knudsen number, which is defined as the ratio between the molecular mean free path length to a

characteristic physical length scale. The latter is, in the hot-wire application, the diameter of the wire itself.

$$Kn = \frac{1.587 \times 10^{-8}}{\rho d_w} \tag{2.3}$$

Due to the small dimension of the wire the Knudsen number would be close to the continuum flow limit – around 0.01 – and its influence in the heat transfer must be accounted in the recovery factor computation. The latter is accounted as

$$\eta = \eta_c + \eta^*\big(\eta_f - \eta_c\big) \tag{2.4}$$

where η^* is the normalized recovery temperature, η_f and η_c are respectively the free molecular and the high Reynolds number continuum limit and their expressions are [12]

$$\eta_c = 1 - 0.05\frac{M^{3.5}}{1.175 + M^{3.5}} \tag{2.5a}$$

$$\eta_f = \eta_c + 0.2167\frac{M^{2.8}}{0.8521 + M^{2.8}} \tag{2.5b}$$

$$\eta^* = \frac{Kn^{1.193}}{0.493 + M^{1.193}} \tag{2.5c}$$

2.1.1 Constant Temperature Anemometry

There are three ways to operate a hot-wire anemometry. The oldest one is a Constant Current Anemometry (CCA) in which the current is kept constant and a variation in the wire resistance (thus temperature) creates an unbalance in the voltage across the bridge, which will be correlated to heat transfer fluctuations. A second operation mode is the Constant Voltage Anemometry (CVA) but it is still under development and the technique is not as mature as the CCA and the Constant Temperature Anemometry (CTA).

The constant temperature operation is the best approach in order to annul the thermal inertia term in equation 2.2. A circuit of the CTA mode is depicted in figure 2.1. The wire is a leg of a Wheatstone bridge, where the resistance (hence its temperature) is kept constant thanks to a fast response feedback amplifier, which reacts to a variation of the cooling power of the flow (i.e. flow velocity). As a consequence the current varies leading to an unbalance of the bridge top voltage. The fluctuations in bridge top voltage are related then to the heat transfer fluctuations.

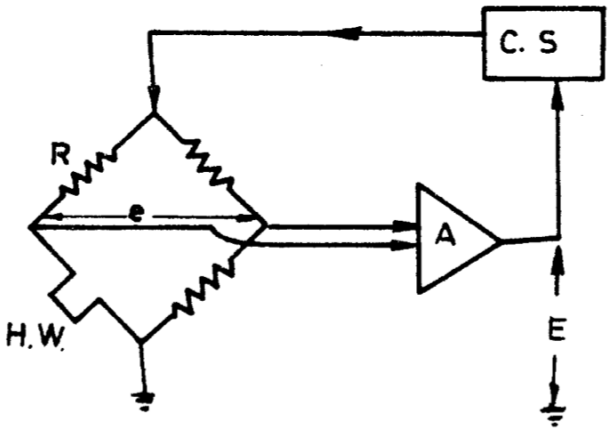

Figure 2.1: Constant Temperature Anemometry (CTA) [9]

The CTA is the most used approach for measurement of turbulent quantities, given the high frequency response, which is upper bounded only by the feedback amplifier itself. Indeed the equation 2.2 becomes,

$$\frac{\mathrm{E}_w^2}{\mathrm{R}_w} = \pi l_w d_w h\big(\mathrm{T}_w - \eta \mathrm{T}_0\big) \tag{2.6}$$

in which, the thermal inertial term has been neglected.

2.2 Mass Flux Calibration

The heat transfer phenomena for heated wires in cross flow is ruled by different parameters of the flow and by geometrical constriction. Transposing the latter conclusion to HWA one can, therefore, link in a proportional way the wire voltage E_w with flow density, velocity, flow angle, total temperature, beside wire geometry and wire temperature, $\mathrm{E}_w = f\big(\rho, \mathrm{V}, \mathrm{T}_0, \mathrm{T}_w, \phi, d_w, l_w\big)$.

The most known equations is the King's Law $\mathrm{E}^2 = A + B\mathrm{V}^n$, where A, B and n are calibration constants, which depend on flow conditions, above all flow total temperature. A calibration curve as the one proposed by King has a drawback of being feasible only for a limited velocity range and for isothermal flow conditions.

In order to correlate the wire voltage only to the flow velocity, all the other dependencies must be decoupled from the latter relation by means of a non-dimensional calibration curve.

The calibration methodology used in the present project is the one proposed by Cukurel [4]. In this paper the heat transfer and the mass flux are accounted with a dimensionless approach, e.g. the Nusselt number (Nu) directs the heat transfer.

Given a certain fluid, a known wire geometry, assuming a 0° flow angle with respect to the wire (see section 2.3.2), neglecting the natural convection (viable for $Re > Gr^{0.3}$ [10]) and considering an incompressible flow, the heat transfer relationship can be written as only a function of the Reynolds number, hence the mass flux.

$$Nu = f\big(Re\big) \tag{2.7}$$

Cukurel [4] and Acarer [5] give a deeper explanation of the methodology also for a compressible case, in which the Mach number dependency on the Nusselt number must be considered together with the Reynolds.

The nominal flow conditions predicted at the test rig inlet are illustrated in table 2.1 for few characteristic blade heights. The evolution along the span of Reynolds number and Mach number is also shown in figure 2.2. It is evident that the Mach number is always abundantly lower than the compressibility limit of 0.3, thus the flow can be considered incompressible. Hence, the voltage fluctuations output of the hot-wire is correlated only to velocity and total temperature fluctuations, while density fluctuations can be considered negligible.

One methodology to decouple the two effects is to compute a sensitivity analysis. For a CTA, the King's law can be written as [11],

$$\frac{\mathrm{E}^2}{\mathrm{R}_w} = l_w\Big[\kappa + \sqrt{2\pi\kappa c_p \rho \mathrm{V} d_w}\Big]\big(\mathrm{T}_w - \eta \mathrm{T}_0\big) \tag{2.8}$$

If one assume that the change in κ, η and c_p are negligible, the change in E, for incompressible flow, will be a function of velocity and total temperature, hence,

$$\frac{e^{'}}{\mathrm{E}} = S_u \frac{\mathrm{v}'}{\mathrm{V}} + S_{T_0} \frac{\mathrm{T_0}'}{\mathrm{T}_0} \tag{2.9}$$

The sensitivity parameters can be obtained by varying one parameter while holding the others constant. The drawbacks of this methodology are the high costly and time-spending procedure and the necessity of at least two wires simultaneously.

Span [%]	$\mathbf{T}_{01}$ **[K]**	$\mathbf{P}_{01}$ **[Pa]**	**M [-]**	$\mathbf{Re}_w$ **[-]**
100.00	300.0	97478	0.00	0.00
90.84	411.8	98009	0.089	11.57
50.00	440.8	98000	0.097	10.67
10.36	410.2	98006	0.099	12.89
0.00	300.0	97333	0.00	0.00

Table 2.1: Nominal inlet flow condition predicted with CFD for some characteristic points of the Span

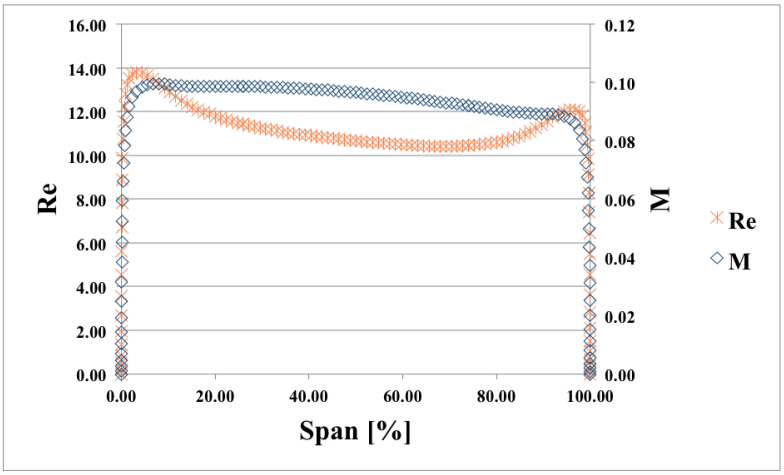

Figure 2.2: CFD prediction for Reynolds and Mach number at stator inlet

Alternatively a direct and analytical method can be performed, but, since the relation $\mathrm{E} = f\left(\mathrm{V}, \mathrm{T}_0, \mathrm{T}_w\right)$ is not physical, a multi-regression fitting is needed with a high number of points in a closed loop facility. This makes the methodology not applicable in the present project in which a single wire probe is used in a blow-down wind tunnel.

However, in a CTA mode of operation if the wire temperature is kept at 1.5 times the flow total temperature, the temperature fluctuation effect can be neglected, as stated by Acarer [5]. In the present study a value higher than 1.25 was found to be a good enough temperature overheat ratio $\mathrm{T}_w/\mathrm{T}_0$.

From a dimensional analysis the heat transfer can be expressed in terms of Nusselt number and it depends, in the most general form for a *cylinder shaped* wire, on flow parameters and geometry quantities, which may be written in a dimensionless way as

$$Nu = f\left(Re, Pr, M, Gr, \tau, \phi, \frac{l_w}{d_w}\right) \tag{2.10}$$

where τ is the overheat factor defined as

$$\tau = \frac{\mathrm{R}_{w,hot} - \mathrm{R}_{w,cold}}{\mathrm{R}_{w,cold}} = \alpha_{20}\Delta\mathrm{T} \tag{2.11}$$

and $\Delta\mathrm{T}$ is the difference between the wire Temperature T_w and 20°C at which the cold resistance of the wire is measured, thus known. α_{20} is the temperature coefficient of resistance at 20°C and depends on the wire material.

In a CTA mode of operation the overheat factor is maintained constant by the feedback amplifier. Once again, for $Re > Gr^{0.3}$ the buoyancy effect can be

neglected. For a given probe and a known fluid, l_w/d_w and Pr are constant. By the assumption of 1-D flow direction and probe aligned to the flow direction also the flow angular dependence ϕ can be omitted (see section 2.3.2). Finally, for incompressible flow, as the one expected at the facility inlet, compressibility effect, thus the Mach number, can be neglected. Hence,

$$Nu = f\big(Re\big) \tag{2.12}$$

With the dimensionless approach, the velocity sensitivity in an incompressible flow is totally included in the Reynolds number computed on the wire diameter, which definition is

$$Re = \frac{\rho \mathrm{V} d_w}{\mu} \tag{2.13}$$

The use of non-dimensional parameters with widely accepted correlations allows to perform a calibration without the need for a closed loop wind tunnel, which changes each flow variable independently and requires a long time of operation. Instead, a simple jet (see section 2.3) operated in similitude with the flow condition expected in wind tunnel is enough to determine the velocity sensitivity and perform an accurate calibration even in a relatively short time.

Considering the expectation for Reynolds number and Mach number at the stator inlet, predicted in a preliminary way by numerical computation and shown

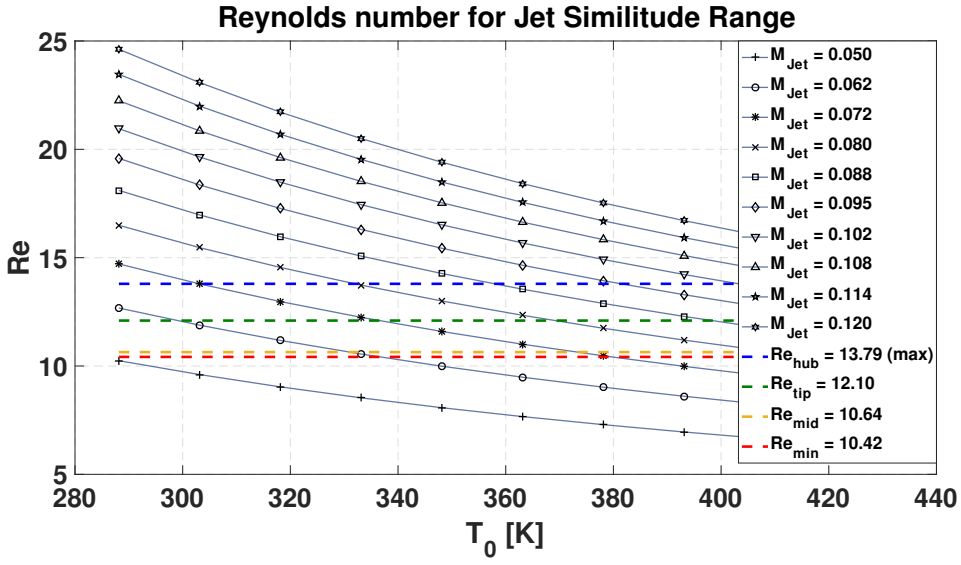

Figure 2.3: Range of T_0 and Mach number for Reynolds similitude in hot-wire calibration

in figure 2.2, a similitude analysis – imposing an equal Reynolds number between the stator inlet and the calibration jet – gives the conditions wanted in terms of Mach number, hence total pressure for a known static pressure, at different stagnation temperature arbitrarily chosen during the calibration. The hot-wire calibration will be performed, then, with value of T_0 and p_0, hence Mach number, chosen within the range of Reynolds number, as shown in figure 2.3.

2.3 Calibration Set-Up

2.3.1 The Dantec Anemometer Frame

In order to use a hot-wire in a constant temperature mode (CTA) a feedback loop control is required. The *Dantec Streamline 90N10* frame (figure 2.4), initialized and operated by ®*Dantec StreamWare* software, serves this purpose. It includes a controller circuit and 4 CTA modules, each of them has its own programmable signal conditioner in order to perform the amplification and offsetting of the signal, beside low-pass filtering up to 300 kHz.

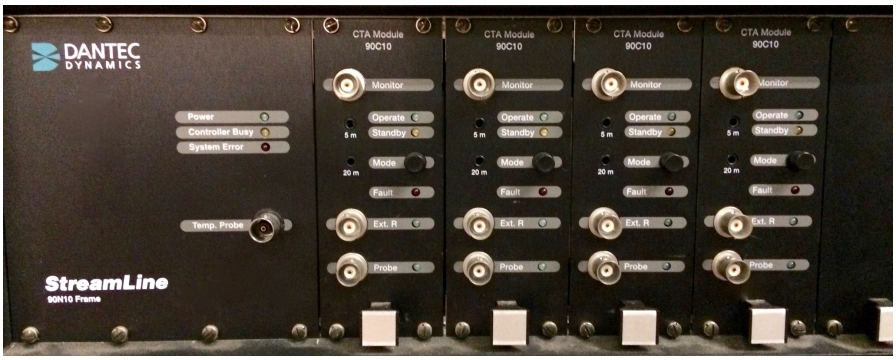

Figure 2.4: Dantec CTA frame

As the name suggests, the CTA mode is based on the principle that the temperature of the wire remains constant during the operation. However, the Dantec StreamWare software allows to fix the overheat factor τ expressed by equation 2.11 and not the wire temperature, which is a function of τ and, thus, of the hot resistance $R_{w,hot}$ and also of the cold resistance $R_{w,cold}$ measured by the Dantec frame and which depends on the ambient temperature. In case in which a in-situ calibration is not possible – circumstance under which this project falls – the frame, thus the software, must be switched off and moved from the calibration location to the wind tunnel in which the measurements are performed. This yields, unless a fortunate coincidence in which ambient temperature does not change, to

a different measured cold wire resistance and, consequentially, to a different wire hot temperature during operation.

In order to overcome the above mentioned problem, the Dantec frame can be tuned by referencing the wire resistance based on an initial and predefined value. With this adjustment the wire resistance in operation mode is the same as the one imposed during calibration.

2.3.2 The Hot-Wire Probe

The wire resistance can change also because of *ageing* effect, due to oxidation of the wire material. In this case no adjustment is possible beside a new calibration.

Since the inlet total temperature is pretty high ($\approx 440K$) and given the limitations of hot-wires with respect to the temperature of the flow, in order to increase the sensitivity of hot-wire only to velocity, an effective way is to increase the wire temperature as much as possible. Nevertheless, at temperature above $250 \div 300°C$, standard hot-wire's materials age very quickly.

Typical materials for hot-wires are tungsten, platinum, nickel and tehir alloys. Although tungsten has the advantage to be more resistant, it ages more easily at higher temperature than platinum, which has, on the other hand, the drawback of being more fragile.

For these reasons a special material was chosen which resists to very high temperature, this is an alloy of Nickel and Platinum, welded with high melting point tin.

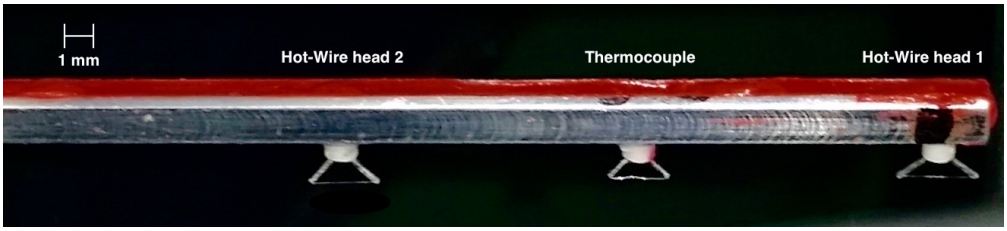

Figure 2.5: The DAO111A hot-wire probe

The probe, shown in figure 2.5 consists of two hot wires located at 37 mm of distance from each other, in order to cover the whole span of the stator inlet – blade height of 74.71 mm – with a relatively low number of tests, and of a thermocouple used to measure reference total temperature between the wires.

The wire is of 9 μm in diameter and 1 mm in active length – out of a 2 mm total length, considering also the copper ending used to prevent interference with the prongs. Although usual wire diameters are 5 μm to enhance spatial resolution, a 9 μm diameter provides higher structural strength and higher resistance to ageing

effect. The 1 mm length is in trade-off between a good spatial resolution and the advantage given by an *infinite length* wire for which heat transfer by conduction to the prongs is null and its heat loss rate depends only on the component of velocity $V_n = V \cos\phi$ normal to the wire. The optimum is at ratio $2l_w/d_w = 100 \div 250$ [13]. Indeed the effective Velocity measured by the hot wire must include a flow angle dependency

$$V_{eff} = V\left[\cos^2\phi + b^2 \sin^2\phi\right]^{1/2} \tag{2.14}$$

where the coefficient b decreases as the ratio $2l_w/d_w$ increases. For the probe used in this work, the ratio is around 225, for which the coefficient b can be neglected with a minimum error [13].

2.3.3 Total Temperature and Total Pressure

In order to compute Nusselt number and Reynolds number, so that the relation 2.12 is fulfilled, total temperature T_0 and total pressure p_0 have to be measured where the flow meets the wire.

The stagnation pressure is measured by means of a *Validyne* differential pressure transducer – equipped with a 86 mbar square membrane – connected with a *Validyne* amplifier, shown in figure 2.6a.

The total temperature is measured by a K-type thermocouple, as the one in figure 2.6b.

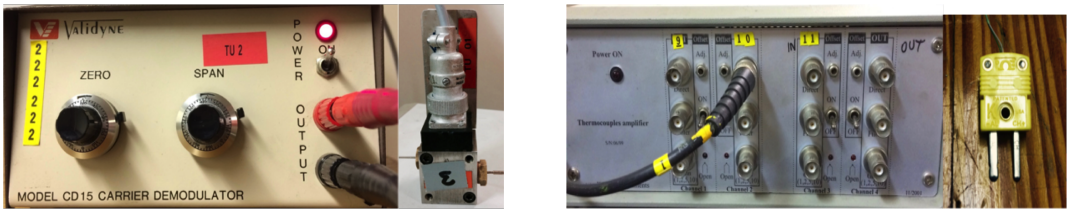

(a) (b)

Figure 2.6: Validyne amplifier with differential pressure transducer (a) and Thermocouple amplifier with K-type thermocouple (b)

2.3.4 The National Instrument Acquisition System

Hot-Wire, Thermocouple and Validyne voltages are acquired by a NI USB-6251 data acquisition board provided by National Instruments, shown in figure 2.7. It consists of 16 input channels with a 16-bit accuracy and a sampling frequency up to 1.25 MHz.

Figure 2.7: 16-bit National Instrument Acquisition System

The hot-wire requires a high frequency sampling in order to capture all the possible turbulent time scales. The frequency response of the wire is optimized by a square-wave test. Although it is ideal to perform the square-wave test in the facility where the test will take place, this was not possible, thus it was conducted in the same jet facility at the highest velocity expected during measurement. Frequency response resulted in the range between 17 and 20 kHz. After a spectral analysis of the signal acquired in flow condition the cut-off frequency (taken to be the one where only white noise is discernible) was found to be around 20÷30 kHz, depending on probe position and flow condition. Following the Nyquist theorem – for which in order to avoid aliasing of the signal a sampling frequency of at least twice the highest useful frequency must be provided – the sampling frequency during calibration was set at 65 kHz, acquiring the signals for 3 seconds, resulting in 195000 samples.

2.4 Calibration Methodology

In order to correlate the Nusselt and the Reynolds numbers some parameter must be measured and/or calculated.

A schematic of the calibration facility is shown in figure 2.8. Stagnation pressure and temperature are measured before the contraction of the jet where the flow can be considered stationary and by assumption of isentropic contraction, both total temperature and total pressure can be considered constant and equal to the one *felt* by the wire at the nozzle exit. Since the flow exits in atmospheric condition, the static pressure is considered to be the atmospheric one.

A heater is located upstream the jet facility in order to vary air temperature from the ambient one up to around 55 °C.

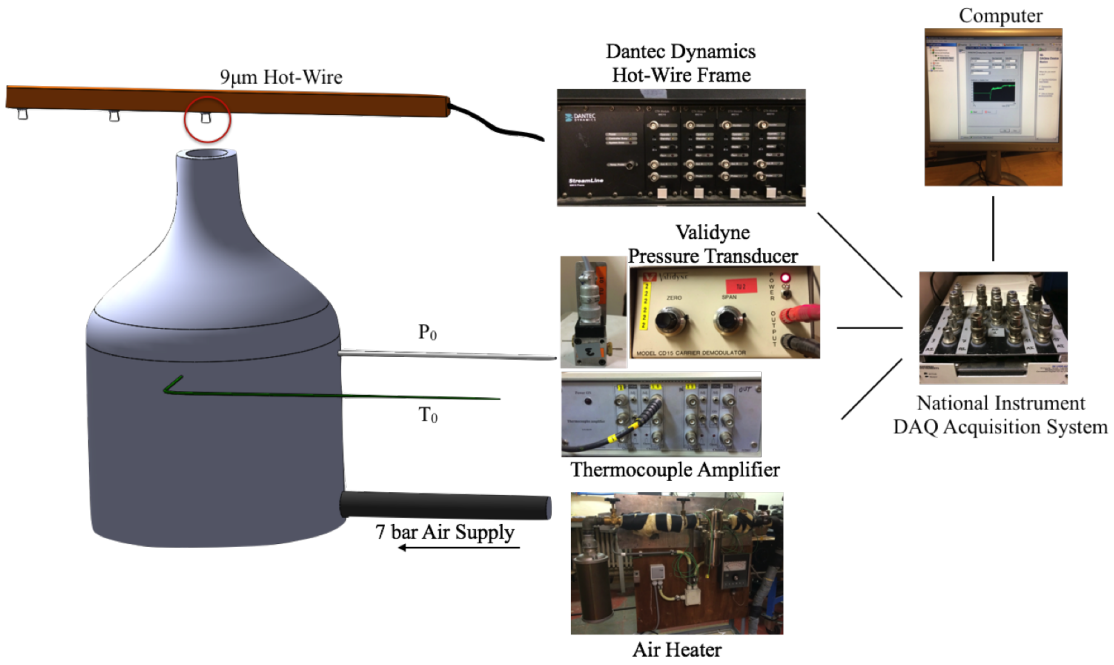

Figure 2.8: Schematic of the Calibration Jet Facility

To completely define the Reynolds number computed on the wire diameter (equation 2.13), velocity V, density ρ and dynamic viscosity μ must be known. From gas dynamic theory the flow is completely defined in its mean quantities by the knowledge of three independent variables, these are as already mentioned in the present dissertation total temperature, total pressure and static pressure.

Thus, before the jet facility may be used, the Validyne pressure transducer and the K-type thermocouple must be calibrated.

As far as the Validyne is concerned, its calibration is performed by a DPI 610 pressure calibrator pump of figure 2.9a. The differential pressure is varied starting from the zero (ambient pressure) up to +60 mbar and down again till −30 mbar in order to check that the pressure input does not affect the value of the internal state of the membrane which should keep its elasticity, hence the calibration curve should remain linear and not presenting an hysteresis shape. The calibration curve is shown in figure 2.10a and an R-square with at least four significant figures equal to 9 is accepted in order to reduce the uncertainty.

The K-type thermocouple is calibrated in the Thermibel heated oil bath of figure 2.9b located at the same position of a Thermibel digital reference thermometer with high precision up to the third decimal digit. Temperature is set from 10°C up to 50°C and an internal rotating magnet helps to level out the temperature inside the oil bath. The magnet rotational speed can be adjusted during the op-

(a) (b)

Figure 2.9: DPI 610 pressure calibrator pump (a) and Thermibel oil bath (b)

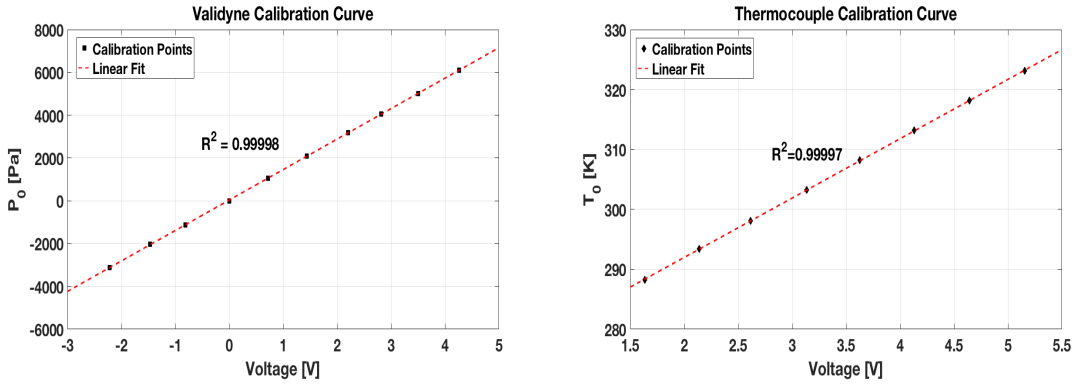

(a) (b)

Figure 2.10: Validyne calibration curve for total pressure measure (a) and Thermocouple calibration curve for total temperature measure (b)

eration. Also in this case the calibration fitting curve is linear (figure 2.10b) and an R-square with at least four significant figures equal to 9 is accepted for sake of precision.

Static pressure in this condition is the ambient one which is measured by a DPI unit that serves the whole Von Karman Institute.

From total and static pressure, the Mach number can be calculated by well

known isentropic gas-dynamic relations

$$M = \left\{ \left[\left(\frac{\mathrm{p}_0}{\mathrm{p}} \right)^{\frac{\gamma-1}{\gamma}} - 1 \right] \frac{2}{\gamma - 1} \right\}^{0.5} \tag{2.15}$$

where $\gamma = c_p/c_v$ is the heat capacity ratio for air and it is equal to 1.4.

Static temperature is evaluated with the assumption of isentropic process

$$\mathrm{T} = \mathrm{T}_0 \left(\frac{\mathrm{p}}{\mathrm{p}_0} \right)^{\frac{\gamma-1}{\gamma}} \tag{2.16}$$

Density is computed with the equation of state for perfect gases.

$$\rho = \frac{\mathrm{p}}{\mathrm{T}R} \tag{2.17}$$

with R the gas constant that, for air, is equal to 287.113 $J/(kgK)$.

All quantities are known in order to compute the flow velocity by the definition of Mach number and speed of sound for perfect gases.

$$\mathrm{V} = M\sqrt{\gamma R \mathrm{T}} \tag{2.18}$$

Finally the dynamic viscosity is calculated by the Sutherland law, based on kinetic theory of ideal gases.

$$\mu = \mu_{ref} \left(\frac{\mathrm{T}_{ref} + \mathrm{T}_s}{\mathrm{T}_0 + \mathrm{T}_s} \right) \left(\frac{\mathrm{T}_0}{\mathrm{T}_{ref}} \right)^{3/2} \tag{2.19}$$

where T_{ref} and μ_{ref} are the reference temperature and the reference viscosity (e.g. $\mu_{ref} = 1.716 \times 10^{-5}$ for $\mathrm{T}_{ref} = 273.15\mathrm{K}$). T_s is the Sutherland temperature and it is equal to 110.4 K.

If the Reynolds number correlates the flow quantities and gives information about velocity, the Nusselt is the dimensionless number used to describe the heat transfer and it is accounted with its definition

$$Nu = \frac{h d_w}{\kappa} \tag{2.20}$$

and by the definition of the convective heat transfer coefficient h

$$Nu = \frac{\mathrm{Q} d_w}{\kappa A \big(\mathrm{T}_w - \eta \mathrm{T}_0 \big)} \tag{2.21}$$

where $A = \pi l_w d_w$ is the surface of the wire. The heat Q is equal, for CTA mode, to the electric power provided to the wire $\mathrm{E}_w^2/\mathrm{R}_w$. However the voltage output is the said top bridge voltage. The relation between the total resistance

and the wire one is the one typical of the Wheatstone bridge, of which the wire forms a leg.

$$\frac{\mathrm{E}_w}{\mathrm{R}_w} = \frac{\mathrm{E}_b}{\mathrm{R}_t + \mathrm{R}_l + \mathrm{R}_w} \tag{2.22}$$

where R_t is the top bridge resistance and R_l is the lead resistance. Thus, equation 2.21 becomes,

$$Nu = \frac{\mathrm{E}_b^2}{\mathrm{T}_w - \eta \mathrm{T}_0} \frac{\mathrm{R}_w}{\pi \kappa l_w \big(\mathrm{R}_t + \mathrm{R}_l + \mathrm{R}_w\big)^2} \tag{2.23}$$

The thermal conductivity can be expressed by the relation

$$\kappa = \kappa_{ref} \left(\frac{\mathrm{T}_0}{\mathrm{T}_{ref}} \right)^{0.7} \tag{2.24}$$

where T_{ref} and κ_{ref} are again the reference temperature and reference thermal conductivity (e.g. $\kappa_{ref} = 0.024$ for $\mathrm{T}_{ref} = 273.15\mathrm{K}$).

2.4.1 The Effective Wire Temperature T_w

What is still unknown and required in equation 2.23 in order to compute the Nusselt number is the wire temperature reached once the overheat is imposed and the wire is fed with current.

In [10] the wire temperature is computed analytically with the resistance-temperature relation

$$\mathrm{T}_w = \mathrm{T}_{ref} + \frac{\mathrm{R}_{w,hot} - \mathrm{R}_{w,cold}}{\alpha \mathrm{R}_{w,cold}} = \mathrm{T}_{ref} + \frac{\tau}{\alpha} \tag{2.25}$$

However, this conceals an assumption that the wire temperature is uniform along its length. This is not true because of prongs conductivity and it depends also on the wire diameter and length, thus it is not clear whether maximum or an average of the wire temperature distribution is the best choice to describe the phenomena. A solution is to define a temperature most representative of the heat transfer itself which may be defined as *effective* wire temperature.

The methodology applied in references [4] and [14], makes use of the concept for which the calibration relation 2.12 for low-speed flow (i.e. $M < 0.2$ [5]) is a one-variable equation, thus the acquired data cloud must collapse in a single curve.

For this reason the wire temperature is left as an unknown and by an iterative process the *effective* wire temperature $\mathrm{T}_{w,eff}$ is found as the one that maximize the R-square value of the least squares 4_{th} order polynomial fitting curve.

2.5 Results

Calibration is performed at five different temperatures starting from the ambient one to a maximum of 55 °C and at different Mach number, hence at different total pressure, from a minimum of 0.045 to a maximum of 0.25. Higher Mach number would introduce a compressibility effect for which density change would affect the heat transfer and consequentially the voltage output as well as flow temperature and velocity. In terms of dimensionless numbers, the Nusselt number would be function not only of Reynolds but also of Mach number, $Nu = f\big(Re, M\big)$.

However, as previously showed in section 2.2, compressible flows are not of interest for the turbine inlet measurements. As far as the lowest Mach numbers are concerned, a low-speed calibration in a different facility should be performed, since the accuracy for the jet facility of figure 2.8 rapidly decrease at $M < 0.04$. Nonetheless, the range of Mach number expected in the measurement facility (figure 2.2) allows to skip the low-speed calibration, unless measurements at wall proximity and at viscous sub-layer are required.

Figure 2.11 shows the calibrated points in terms of output voltage and flow velocity, following the relation $\mathrm{E}_b = f\big(\mathrm{V}, \mathrm{T}_0, \mathrm{T}_w\big)$. As flow temperature increases the heat transfer decreases and so the voltage output is lower, given the same flow velocity.

Figure 2.12 is the result of the iterative procedure described previously in section 2.4.1 in order to find the wire effective temperature. The R-square value is maximum at 572.18 K, slightly higher than the lower limit of 550 K which permits

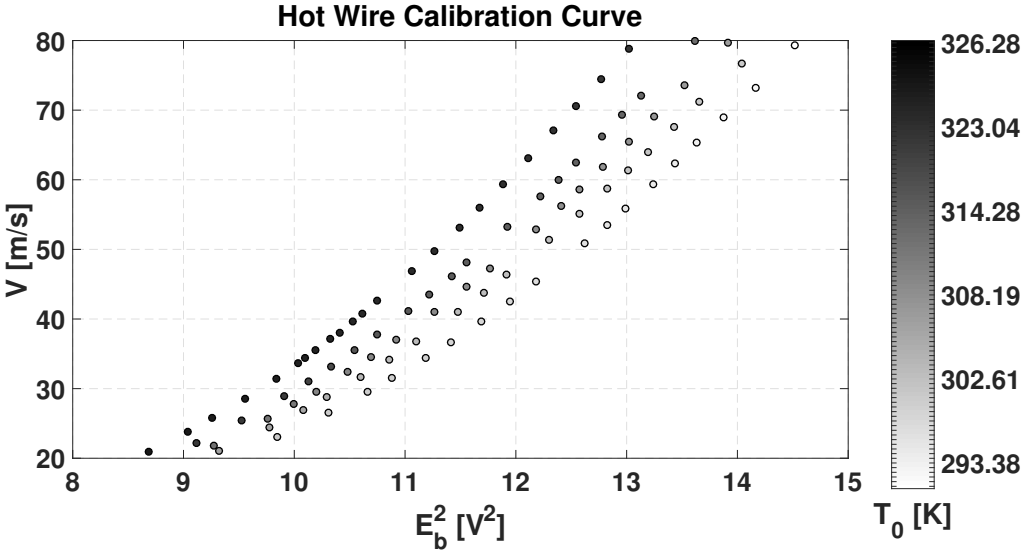

Figure 2.11: Raw calibration data cloud

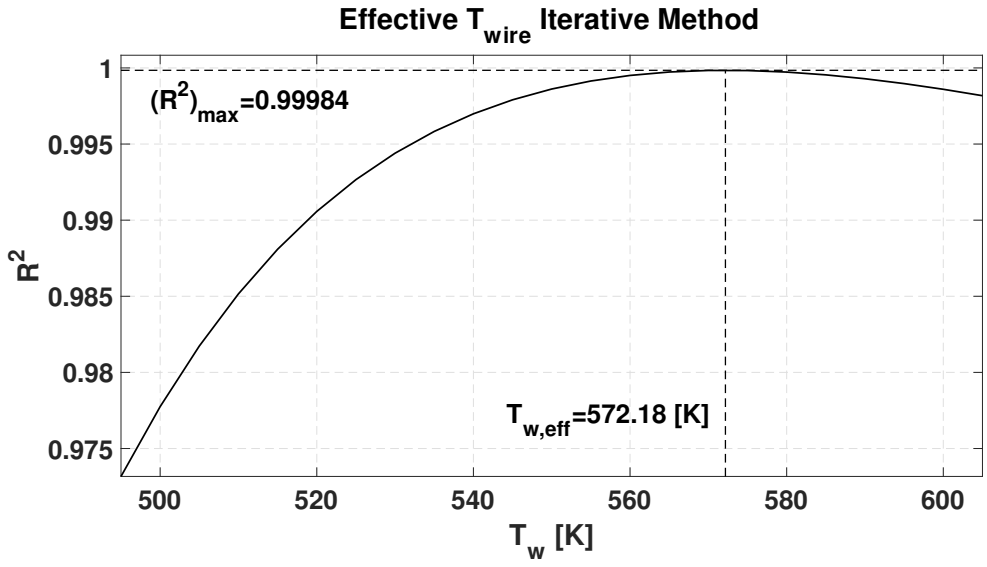

Figure 2.12: R-square evolution with guessed wire temperature

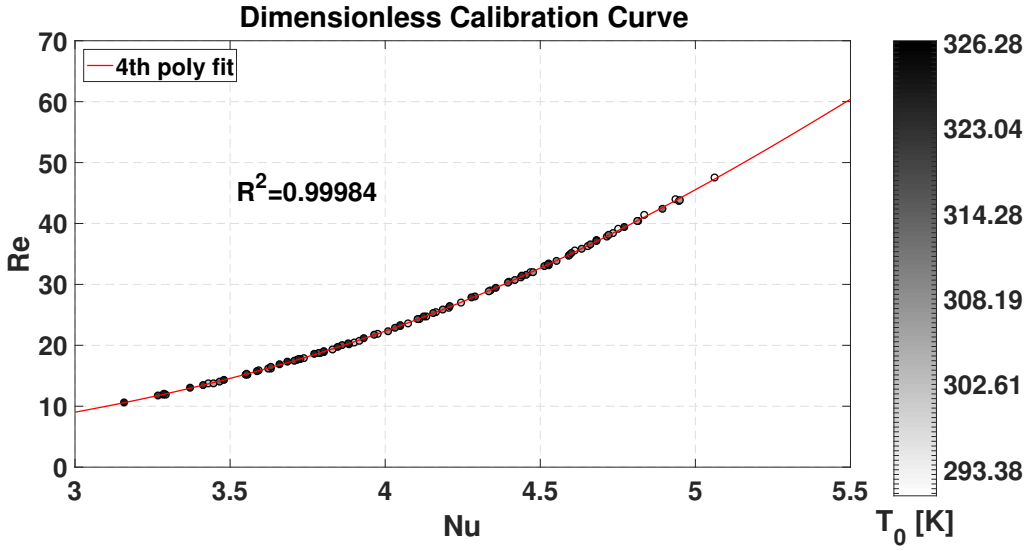

Figure 2.13: Collapsed data in a single curve

to neglect the temperature fluctuations dependency in the sensitivity analysis of section 2.2.

Once the effective wire temperature is found the data are collapsed in the single dimensionless curve of figure 2.13. The fitted curve is a 4_{th} order polynomial, which responds to the needing for linearisation of the calibrated data sets. Indeed, as explained by Carbonaro [9], the non-linearity of hot-wire signal leads to errors in

turbulent flows for mean velocity, fluctuations and averaged turbulent statistics. In order to avoid these errors a linearisation is required. The possible methods are a logarithmic fit or the said polynomial fit. Since $E^2 \propto V^{0.5}$, hence $V \propto E^4$, then at least a 4_{th} order fit is needed. Moreover the calibration curve, fit by polynomial regression, provides a better frequency response than the logarithmic linearizer [9].

2.6 Validation

In order to validate the calibration, time resolved measurements are carried out in the same jet facility where the calibration was performed with different conditions and wire positions. The sampling frequency is set at 65 kHz as the calibration one for 5 seconds.

Four different locations of the wire – at $x/d = 1, x/d = 2, x/d = 3, x/d = 4$, where d is the nozzle diameter of 12 mm – and three different flow conditions in terms of Mach number – $M = 0.095, M = 0.196, M = 0.264$ – are taken into account as shown in figure 2.14. Here the results for the lower Mach number conditions are discussed, as it is the most significant flow condition in the present work (figure 2.15).

It is plain how turbulence intensity (T_u), defined as the ratio between the root mean square of the instantaneous velocity fluctuations and the mean velocity value, increases with the distance x/d from the nozzle exit up to 6.25%.

In order to check the reliability of the hot-wire calibration a comparison between the mean velocity measured by the hot-wire $\overline{V}_{hw}$ and the one computed by pneumatic quantities $\overline{V}_{pneum}$ was realized, exhibiting a good agreement, especially for the data collected at the distance $x/d = 1$ as it is expected. Results are shown in table 2.2.

The deviation from pneumatic probes' results and hot-wire one at the $x/d = 1$

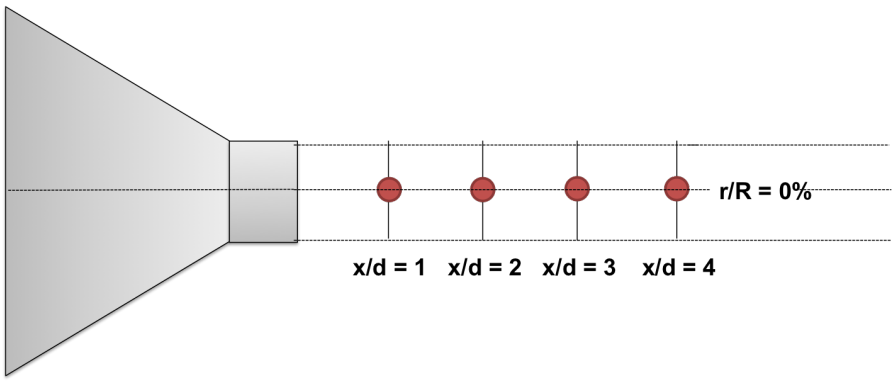

Figure 2.14: Probe location with respect to the nozzle

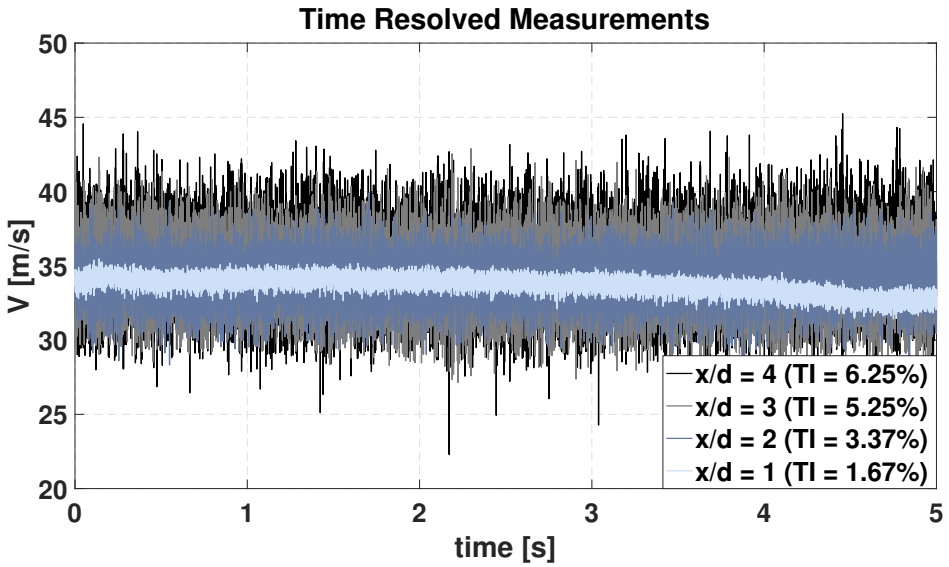

Figure 2.15: Time resolved measurements at different probe position for $M = 0.095$

Probe Location	$\overline{\mathbf{V}}_{hw}$ **[m/s]**	$\overline{\mathbf{V}}_{pneum}$ **[m/s]**	**err [%]**
$\mathbf{x/d = 1}$	33.77	33.28	1.48
$\mathbf{x/d = 2}$	34.13	33.28	2.56
$\mathbf{x/d = 3}$	34.35	33.28	3.23
$\mathbf{x/d = 4}$	34.77	33.28	4.49

Table 2.2: Comparison between mean velocity measured by hot-wire at different wire positions and by pneumatic quantities at the nozzle exit

distance may be due only to random sampling uncertainty. Indeed 1.48% is in the range of uncertainty due to calibration as shown in Appendix A.

The more the wire is distant from the jet the higher is the error. This is due to the fact that when the wire is located at a distance higher than one time the nozzle diameter, given the limitation in the fixing system of the jet facility, it is not possible to be certain to align the wire with the jet central core. Moreover, the small nozzle diameter leads to a very thin core at $x/d \geq 1$ and it may causes uncertainty due to wire spatial resolution.

Nonetheless, an error in mean velocity of 5% was demonstrated to correspond in a maximum error of less than 0.5% in turbulence intensity, for relatively low speed flows.

Furthermore, by applying a fast Fourier transformation (FFT) of the time data series in the frequency domain, the power spectral density can be analysed. In order to avoid spectral leakage and to have higher spectral resolution an Hamming

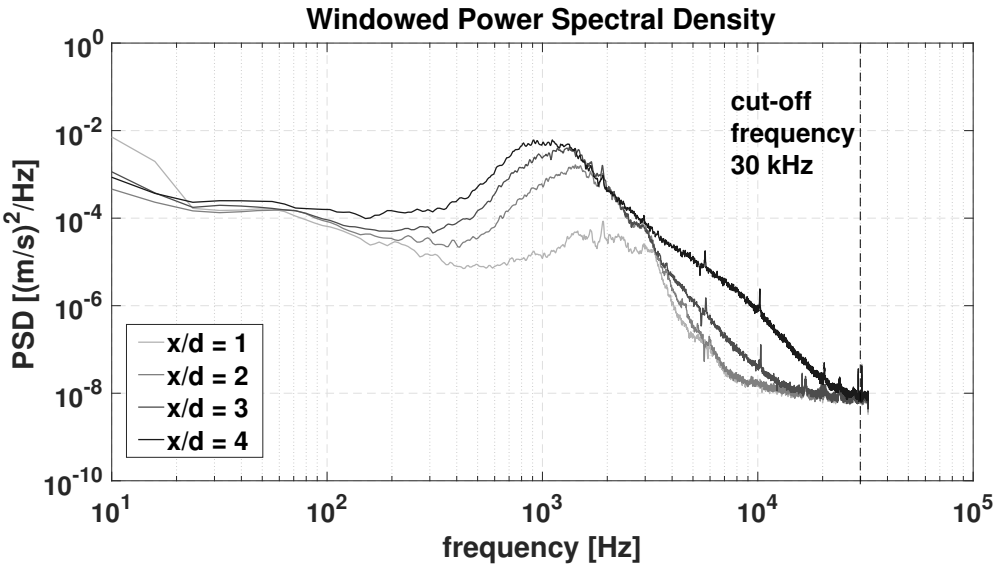

Figure 2.16: Power Spectral Density for different probe position and $M = 0.095$

windowing is applied with the *pwelch* ®Matlab function.

As showed in figure 2.16 some features common in round jet flows may be distinguished.

First of all, a broad frequency peak is evident at Strouhal number between 0.35 and 0.5 in accordance with experiments in the near-field region of a turbulent axisymmetric jet at high Reynolds number [15], where the Strouhal number is computed on the nozzle diameter as,

$$St_d = \frac{fd}{V_{nozzle}} \tag{2.26}$$

where f are the frequencies related to the broad frequency peaks. These peaks are associated to the roll-up of the initial vorticity sheet into the toroidal vortex rings, typical of the core region of a jet characterised by a rapid contraction. The amplitude of the broad frequency peak increases with the distance till $x/d = 4$, though it is expected to decrease as the distance exceeds $x/d = 5$ as observed in the near-field of a round jet downstream an abrupt contraction nozzle [16].

At last, the cut-off frequency was found to be 30 kHz, justifying the choice of 65 kHz for sampling frequency, higher than the Nyquist criterion in order to avoid time aliasing. Further check was done at a sampling frequency of 150 kHz confirming the goodness of the choice.

Chapter 3

Measurement Campaign

3.1 The VKI Anular Cascade Facility CT3

High pressure stage is the life-limiting component in modern gas turbines due to the aggressive environment in which it operates. Thus research has focused on this critical area in order to provide wind tunnels capable of simulating with high accuracy a real operating engine.

Turbine test rigs can be classified based 1) on the geometry of the test section, or 2) on the operation mode. For the first class the distinction is between

1. Linear Cascade Facilities, which advantages are simplicity and possibility of fine optical access. They are often used to study unsteady flow phenomena such as wakes and vortex shedding. Nevertheless it is not possible to provide information about three dimensional paths.

2. Annular Cascade Facilities, which are more complex than the linear cascade and optical access is more difficult to provide. On the other hand, three dimensional phenomena can be simulated, together with real radial and annular distribution of flow properties.

For the second class the difference is between

1. Closed Loop Facilities, which operate in a continuum mode. Thanks to a high interval of time in which measures can be integrated, the measurements are more accurate. As far as heat transfer measurements are concerned, closed loop facilities are not functional. Indeed, after the facility runs for a while, the system reaches the thermal equilibrium with the flow. Furthermore, this kind of facilities requires high power consumption in order to be run for long time.

2. Transient Facilities, which operate for a limited interval of time. They allow to study heat transfer to the wall. Indeed, the characteristic time of conduction is much higher compared to the operation time. By the conductive heat transfer theory, this allows to model the heat transfer with a lumped capacitance method for which the wall temperature is only dependent on time and has a typical *e-folding* trend

$$\mathrm{T}_{wall}\big(t\big) = \mathrm{T}_{\mathrm{inf}} + \big(\mathrm{T}_{initial} - \mathrm{T}_{\mathrm{inf}}\big)\mathrm{e}^{-t/\tau} \tag{3.1}$$

where τ is the characteristic time depending on the ratio between conductive heat transfer and the heat accumulated by the solid body. Another advantage of transient facilities is the low power required during operation, thus low cost. Although they are used mainly for heat transfer, transient facilities are used intensively also for aerodynamic measurements.

Moreover, transient facilities are divided in three categories [17]

1. Blow-Down Tunnel as the one developed in 1984 at the Massachusetts Institute of Technology in which air is suddenly vented through the test section from a pressurized and heated vessel.

2. Shock Tunnel as the one used in Calspan and developed in 1985 in which air is compressed thanks to a shock wave travelling along a tube and then it expands through a nozzle in which a normal shock allows to adapt the flow at the desired guide vane inlet condition.

3. Isentropic Light Piston Compression Tube, as the one developed at Oxford University in 1977, in which air is compressed with a quasi-isentropic process by a moving piston and thereby heated following the isentropic relation

$$\mathrm{T}_{final} = \mathrm{T}_{ambient}\left(\frac{\mathrm{p}_{final}}{\mathrm{p}_{initial}}\right)^{\frac{\gamma-1}{\gamma}} \tag{3.2}$$

The hereby heated and compressed air is then released in the test section by a fast operating valve.

The compressor tube annular cascade facility CT3 of the Von Karman Institute for fluid dynamic (figure 3.1) belongs to the last category and it is the biggest facility in the world of its kind, able to host turbines with tip radius up to 0.8 meters [18].

A schematic layout of the facility is given in figure 3.3 where the main elements of the facility are discernible.

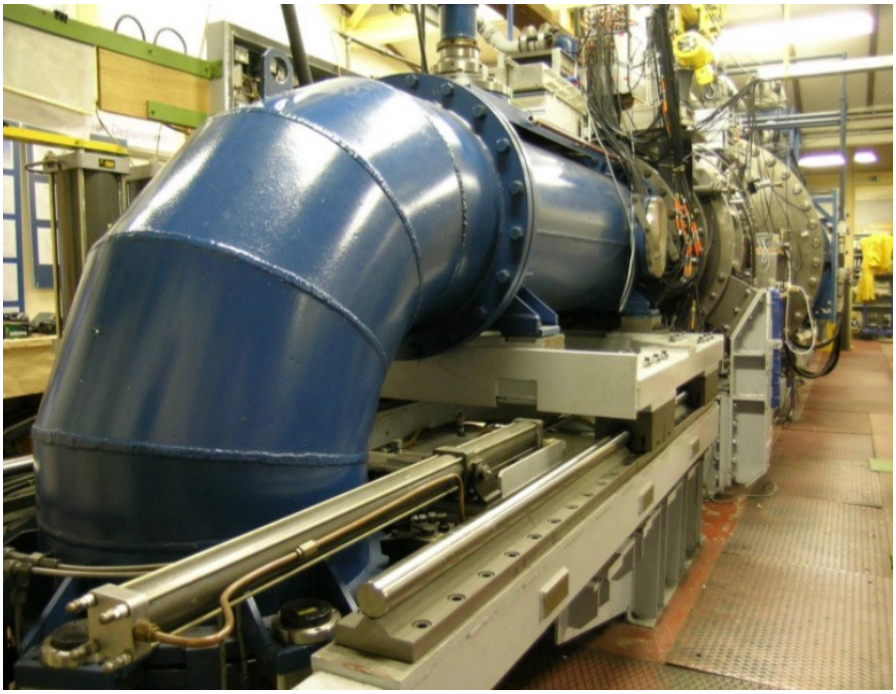

Figure 3.1: Picture of the VKI's CT3 facility

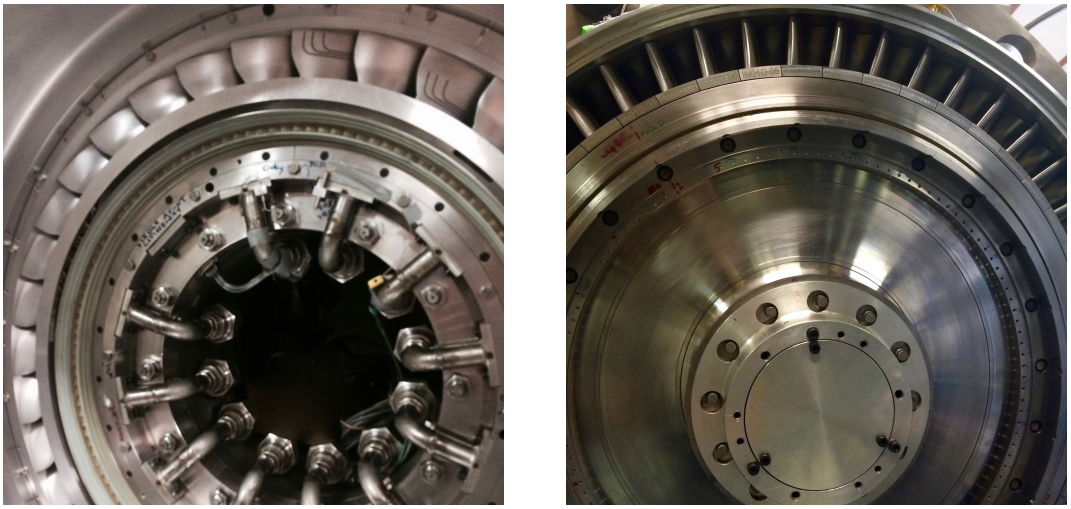

(a) (b)

Figure 3.2: Stator (a) and Rotor (b) of the VKI's CT3 facility

The **compression tube** is connected with the VKI's 300 bar air supply reservoir and it was designed in order to prevent total pressure fluctuation which occurrence is common in transient facilities and depends mainly on the ratio between

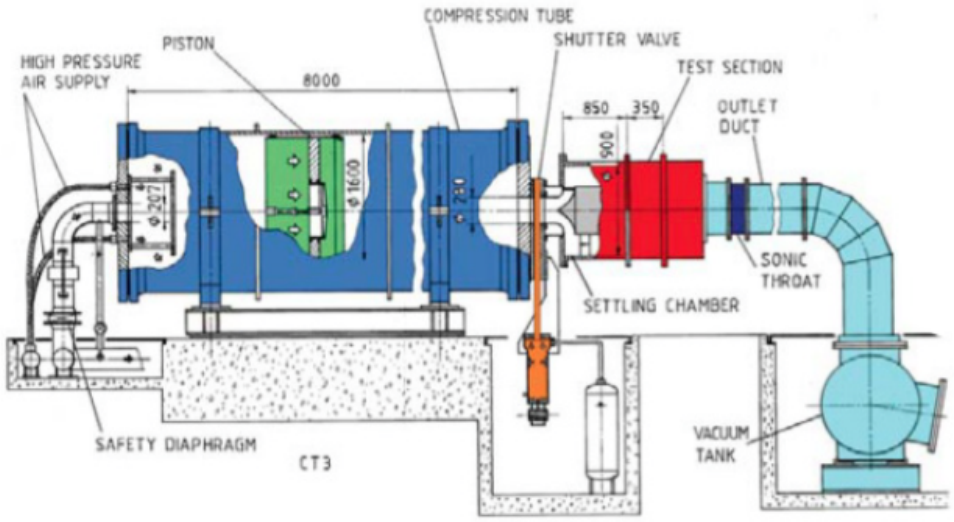

Figure 3.3: General layout of the VKI's CT3 facility

the volume of the tube and the volume upstream the working section nozzle throat. The tube has a dimension of 1.6 meters of inner diameter and it is 8 meters long with a surface roughness of around 6.2 microns for a total volume of circa 15 m^3. Alone it weigth 13000 kg and the maximum allowable pressure is 20 bar [17].

The **piston** is driven by the cold air coming from the external high pressure air supply reservoir from one side and compresses and heats on the other side the working flow. When the flow reaches the pressure desired the **shutter valve**, triggered by a pressure transducer measuring the pressure inside the tube, suddenly open, releasing the flow in the test section. This valve is vertically oriented and consists in a 350 mm diameter disc of titanium. It has an opening velocity of 10 m/s [18] corresponding in an opening time of $40 \div 70$ ms.

Afterwards the flow goes into the **annular settling chamber** of 500 mm and 900 mm of respectively inner and outer diameter, which acts as a damping factor for the oscillation caused by the piston and the rapid opening of the shutter valve and it stabilizes the flow before entering in the test section.

The **test section** hosts the nozzle vanes and the probe traversing system and in this particular experimental campaign consists of a single high-pressure stage containing three measurement planes as depicted in figure 3.4 – turbine inlet, NGV outlet and turbine outlet, referred respectively with the subscripts 1, 2 and 3. The stator shown in figure 3.2a is composed by 38 blades while the rotor of figure 3.2b has 48 blades and it is run at a nominal rotating speed of 5900 RPM and it was mounted in a rainbow configuration to study the flow leakage in 7 different tip geometries.

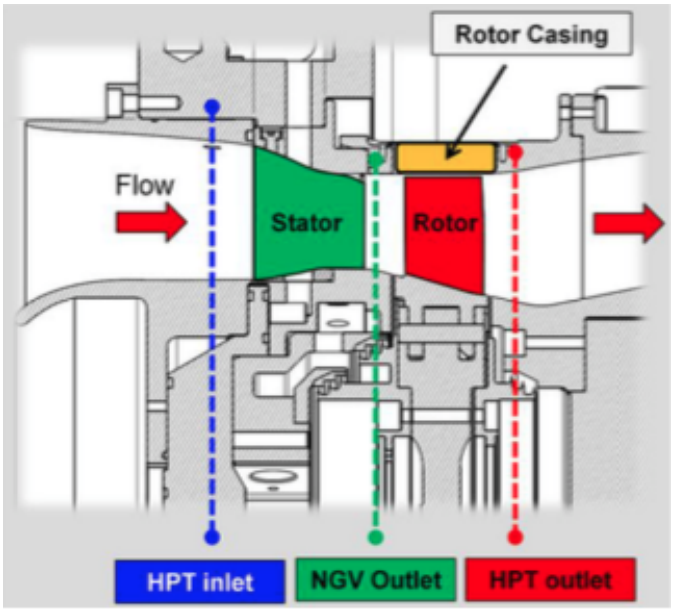

Figure 3.4: Test Section of VKI's CT3 facility with measurements location

Last components of the wind tunnel are a **sonic throat**, with an adjustable section which allows to freely select a desired mass flow rate, and a **vacuum tank** where the flow is discharged at the end of every test.

The facility is designed to simulate the operating condition of modern aero-engines as close as possible. In order to achieve this purpose a scaling approach is used. Similarity is respected in viscous forces with the Reynolds number, thermal properties by means of the Prandtl number, compressibility effect accounted by the Mach number and temperature ratios $T_{flow}/T_{wall}/T_{coolant}$. In the present work the flow parameters of similarity have been optimized and set as in table 3.1 for the whole duration of the experimental campaign.

Indeed, the facility is designed in order to adjust independently the Reynolds

Similitude Parameter	
Outlet Reynolds number computed on Rotor Chord	2.4×10^5
Inlet Absolute Mach number	0.1
Outlet Relative Mach number	0.73
Temperature ratio $\left(T_{wall}/T_{0,1}\right)$	0.68
Non Dimensional Rotational Speed $\left(RPM/T_{0,1}\right)$	281.3
Total to Static Pressure Ratio $\left(p_{0,1}/p_3\right)$	2.2

Table 3.1: Similarity test condition at midspan

number and the pressure ratio, beside the temperature ratio. The free control parameters are [18]

- The inlet total pressure $p_{0,1}$ by selecting a tube pressure at which the shutter valve is triggered and knowing that the inlet stagnation pressure is around 10% lower than the one in the tube.
- The inlet total temperature $T_{0,1}$ according to equation 3.2 by properly choosing the $p_{initial}$, hence the pressure ratio.
- The opening of the sonic throat area which imposes the mass flux.

By adjusting $p_{0,1}$, $T_{0,1}$ and the sonic throat area a wide range of Reynolds number and Mach number can be applied.

Thus, prior to the test, the desired conditions are achieved by creating the *quasi*-vacuum condition in the vacuum tank ($14 \div 30$ mbar of absolute pressure) in accordance with the pre-stabilised inlet total pressure. This process requires up to 45 minutes. Afterword, the rotor is spun up thanks to an high pressure turbine directly attached to the same shaft of the main rotor. Once 95% of the nominal speed is reached, the high pressure air is released at around 270 bar in the tube activating the piston. When the pressure inside the tube is the one desired the shutter valve is triggered and the working flow is discharged in the test section. The test lasts up to 0.4 seconds. At first total temperature and total pressure raise

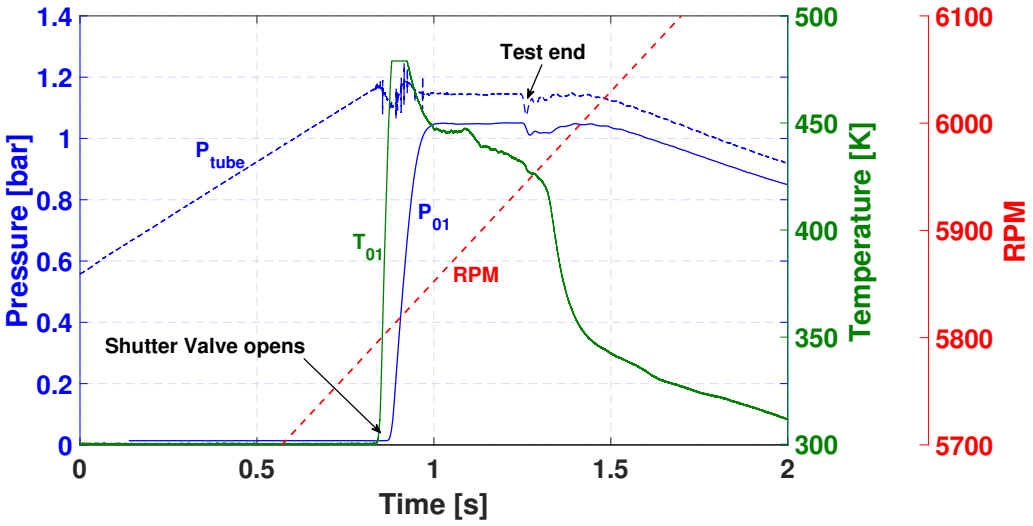

Figure 3.5: Evolution of $T_{0,1}$, $p_{0,1}$, p_{tube} and rotational speed in a typical test sequence

to the nominal value in 0.1 seconds circa. However, before the flow is completely stable, some fluctuations are present due to the mass of the piston. The actual time interval in which the measures are time-averaged is of the order of 0.15 seconds. A typical blow down sequence is depicted in figure 3.5. The end of the test is determined by perturbation travelling towards the test section. This is a sign of when the pressure in the vacuum tank increases above a certain critical point.

3.2 Plane 1 Set-Up

Turbomachinery flows are unsteady and three-dimensional by nature and a variety of measurement techniques must be used in order to catch all thermodynamic and aerodynamic features. For this purpose high frequency response and high spatial resolution are of paramount importance. At the turbine outlet at least a frequency response capable to acquire the blade passing frequency (around 4800 kHz) and its first 5 harmonics is needed [19]. As far as the inlet is concerned, the object is to characterize the flow in terms of big and small length scale of turbulence in order to have as more accurate as possible simulations of the flow. Small turbulent scales, as the Kolmogorov one, are in the range of 10^4 Hz. Hot-wire technique is the only instrument that delivers an analogue output as representation of velocity up to such high frequency fluctuations.

It is evident, though, as hot-wire requires measures of total temperature and pressure in order to transform the voltage signal in useful information of velocity. High precision in these measures, especially in temperature, is required to have reliable value of mean velocity, while velocity fluctuations are only marginally influenced by an error in temperature estimation.

The plane 1 is situated at 0.5 times the stator blade chord upstream of the nozzle guide vane leading edge (figure 3.4). A schematic of the plane 1 set-up is shown in figure 3.6b. In order to gauge the total pressure a Kiel probe is used consisting of four heads to cover the whole span (figure 3.6c top), while total temperature is measured by means of probes consisting of four bare K-type thermocouple rakes (figure 3.6c center). Additionally a probe composed by a Kiel head and a bare K-type thermocouple, quantifying total pressure and total temperature at the midspan, is used as reference value for repeatability check (figure 3.6c bottom). Finally static pressure is measured at the hub end-wall and tip end-wall by means of static pressure taps inserts.

Figure 3.6a shows the hot-wire probes, described in section 2.3.2, inserted in plane 1.

The hot-wire signal is acquired at a sampling frequency of 120 kHz in order to catch all possible flow features and to avoid time aliasing according to the Nyquist criterion. However, some initial tests were performed at a sampling frequency of

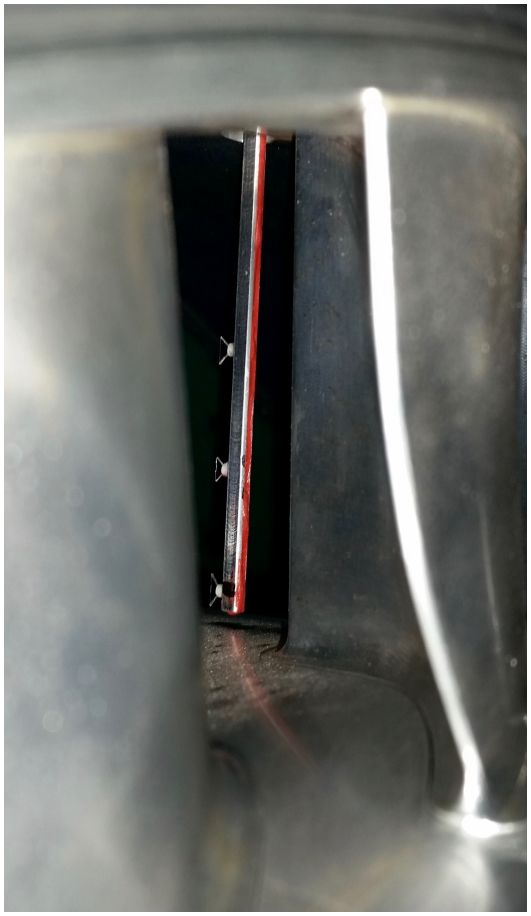

(a) Hot wire Probe inserted in plane 1

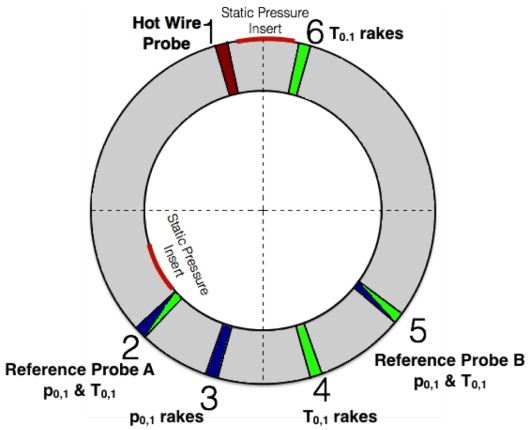

(b) Plane 1 slots

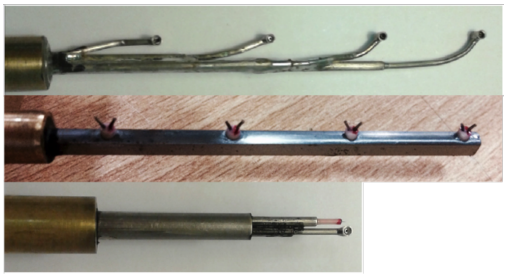

(c) total pressure rakes (top), thermocouple rakes (center), reference probe for T_0 and p_0 (bottom)

Figure 3.6: Plane 1 Set-Up and Instrumentation

1 MHz. Furthermore, the signal is off-setted and amplified by the Dantec system as mentioned in section 2.3.1.

3.3 Post Processing

The signals are acquired by different acquisition systems, each with its own offset and delay. Once all data have been shifted together and coupled with their own calibration fitting, except for the hot wire signal which will be treated in a first moment with its raw voltage signal, the data post processing involves three starting essential steps

1. Detect the time interval in which the flow is stabilized. The letter has been found to be no longer than 0.2 seconds. However some transient fluctuations

are still present after the shutter valve is triggered and the effective stabilised time interval is around $0.1 \div 0.15$ seconds.

2. Fit the total temperature, total pressure and static pressure depending on the hot-wire location along the span. Indeed, although total pressure presents a quasi-flat shape along the blade height, total temperature is affected by stratification. Moreover, the hot-wire results in terms of mean velocity are highly dependent on the exact value of flow total temperature, whilst not accurate total and static pressure value, hence Mach number value, does not implicate a considerable error in terms of Reynolds number.

3. Low-pass filter the signals monitoring the cut-off frequency. This is done in order to avoid noise influence in the final results in terms of velocity fluctuation.

Looking at the total pressure trend in figure 3.7 it is easy to recognize the four different time intervals described previously in section 3.1. The shutter valve takes 0.1 seconds to open and discharge the flow in the test rig. The following 0.1 seconds are characterized by some fluctuations in the tube pressure due to the mass of the piston and, finally, the flow is stable and the signals are processed. The last part of the signal is affected by the increasing pressure in the vacuum tank.

Once the stable window is pinpointed the hot-wire raw voltage is cut and processed. As shown in figure 3.8 the hot-wire signal has its starting point at

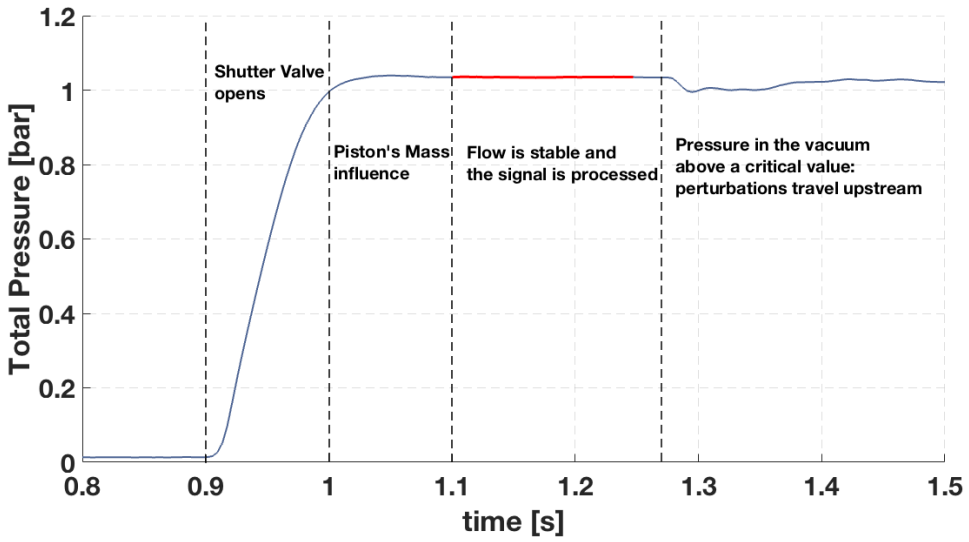

Figure 3.7: Total Pressure sequence and signal fraction used for the post processing

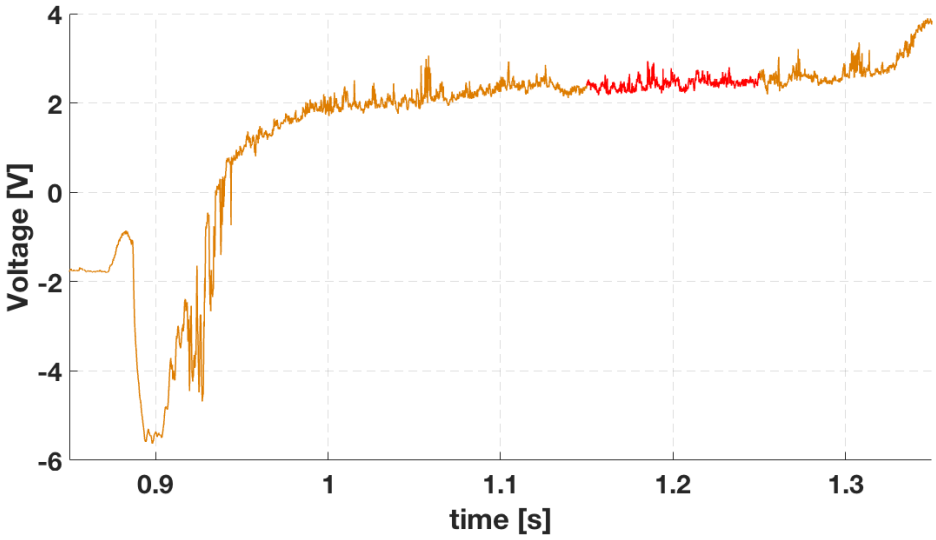

Figure 3.8: Hot-wire raw voltage signal during the blow down

negative top bridge voltage (equals to the effective voltage times the gain and minus the offset) due to the very low density in the test section, which in turn is a consequence of the vacuum condition, and presents a little overshoot after the shutter valve opens due to the fast pressure wave. The signal, then, shows a big undershoot mainly caused by the rapidly increase in flow temperature which reaches value of the order of the wire temperature, drastically reducing the heat transfer.

As already mentioned, the measurement of the hot-wire relies on an accurate knowledge of the total and static pressure and, over all, of the total temperature. Thus, the Mach number must be computed by means of the measures of total pressure performed with the Kiel probes and of static pressure thanks to the pressure tap insert at hub and tip. Whereas the total pressure has a flat trend along the span and the static pressure is almost constant between tip and hub, for which a linear interpolation is accurate enough to predict their value at the hot-wire position, the total temperature may vary up to 40 K from the mid position to the wall proximity. Moreover, while an error in Mach does not imply a significant error in the velocity computed by the hot wire, a small error in temperature leads to strong deviation in velocity.

Indeed, it was demonstrated in a study of two-Dimensional Hot-Wire Anemometry in High Speed Flow [5] that an error of Mach number of 1% is translated in an error of Reynolds not higher than 0.1%. On the other hand, a perturbation analysis performed in the present work revealed how an error of 1% on the value of stagnation temperature leads to an error up to 10% in terms of mean velocity.

Moreover, the same error of total temperature entails a deviation of turbulence intensity up to 1%. Thus, it is clear how a good estimation of total temperature is extremely important to hot-wire results.

Temperature is acquired in different position along the span and the annulus as

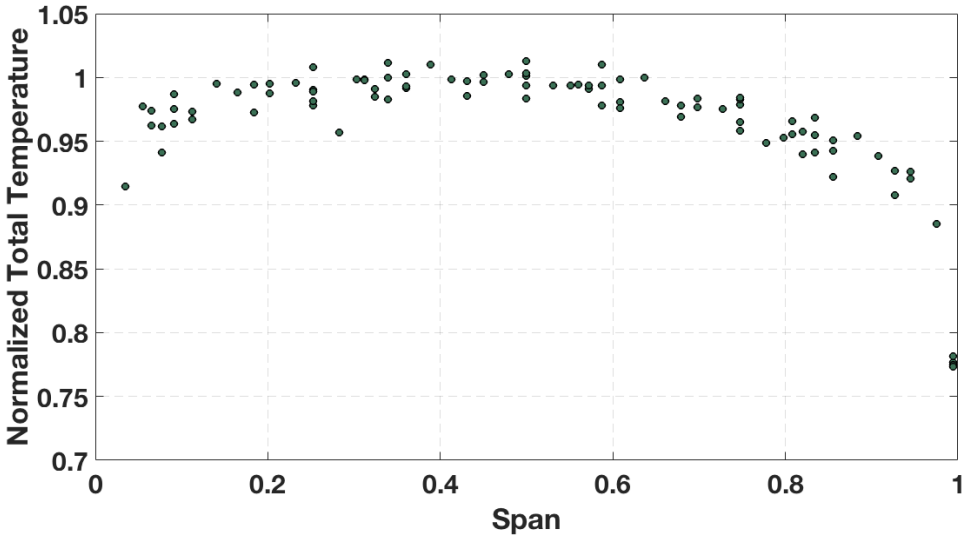

Figure 3.9: Normalized total Temperature along the Span

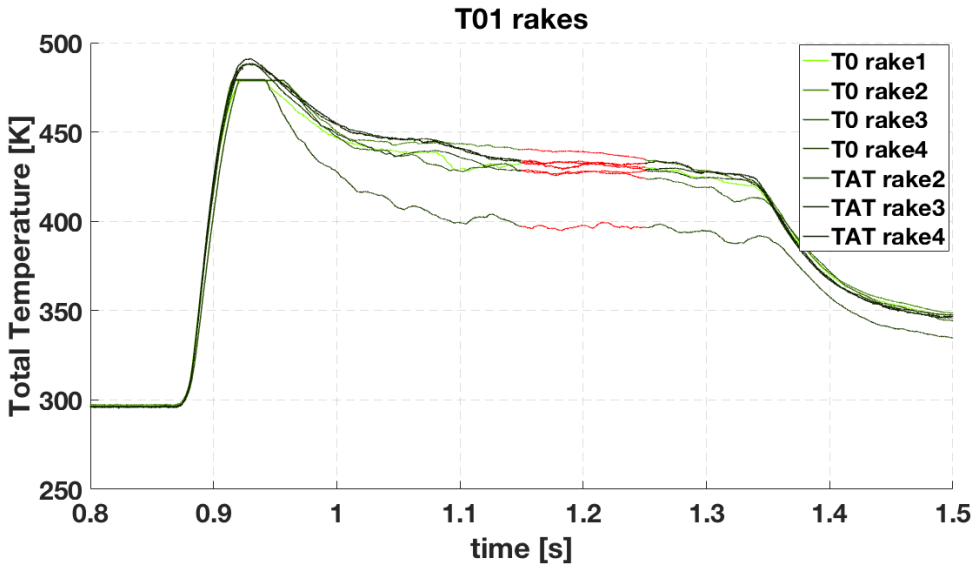

Figure 3.10: Total Temperature sequence during a test for different rakes highlighting the signal fraction used for the post processing

shown in figure 3.6b, and results indicate a trend of total temperature as in figure 3.9 where temperature taken at different positions is normalised with respect of a reference temperature acquired at the midspan for different tests showing a good repeatability.

Two methodologies were proposed in order to predict the total temperature at the location of interest. The first one considers a shape preserving interpolation fitting from the measures of the rakes (figure 3.10) for the single test. The second consists in using the whole tests' history results together with the reference temperature at the midspan from the curve of the repeatability chart obtained in figure 3.9. The results are reported in figure 3.11 showing a good agreement, except for the wall proximity in which the interpolation method does not take into account the wall temperature in the fitting process, therefore the second method is preferred since no hypothesis on the wall heat transfer is needed. The scatter between the two is considered in the uncertainty analysis.

Moreover, it is plain from figure 3.10 how temperature could not reach a perfect stability in the processed time window. In this case the dimensionless calibration curve shows its power, by annulling temperature dependency in velocity computation.

Finally the hot-wire raw voltage is converted in Nusselt number by the equation 2.23. From the calibration curve the Reynolds is determined and finally the instantaneous velocity is calculated from the Reynolds number definition.

A further check is done by comparing the results in terms of velocity com-

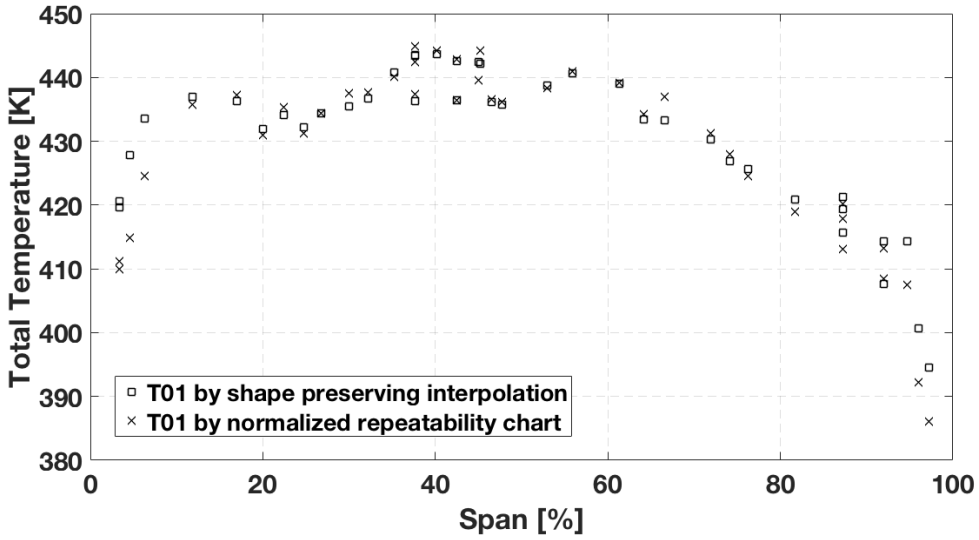

Figure 3.11: Comparison between two methodology of total Temperature computation

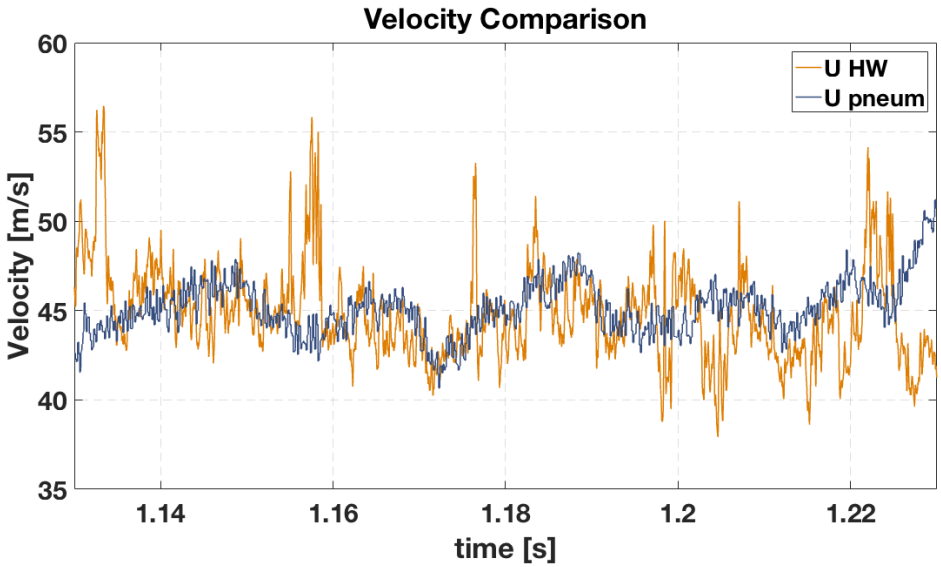

Figure 3.12: Velocity comparison between the one computed by the hot-wire and the one computed by pneumatic rakes

puted with the hot wire methodology and the one computed with the pneumatic quantities at lower frequency as shown in figure 3.12 with a good agreement.

Chapter 4

Results and Discussion

4.1 Statistical Description of Turbulence

There is a large body of literature dealing with the topic of turbulence with almost the same amount of theories and formulations. Among the others, the most detailed books are the one of Pope [20] and Biswas [1].

The most accepted and validated theory is the characteristic feature for which turbulent flows exhibit a large range of length or time scales. However it is common practice for analysis purpose to distinguish between few scales. These are the integral scales, the inertial sub-range scales and the dissipative or Kolmogorov scales.

The integral scales are those corresponding to the energy containing eddies and form the large scales of turbulent flows.

Biswas [1] roughly defines the integral length scale as the distance over which the velocity fluctuations at one point are correlated with those at another point.

The smallest turbulent scales are described by, and named after the Russian mathematician and physicist Andrey Kolmogorov. With his first similarity hypothesis he stated that the geometry and the anisotropy of a flow-field could influence only the large scales, while the smallest scales are only influenced by local quantities such kinematic viscosity ν and energy dissipation rate ϵ. Thus these small eddies, having a smaller time scales, will rapidly settle into a quasi-equilibrium state and can be computed as

$$\eta = \left(\frac{\nu^3}{\epsilon}\right)^{1/4} \tag{4.1a}$$

$$\tau = \left(\frac{\nu}{\epsilon}\right)^{1/2} \tag{4.1b}$$

where η and τ are respectively the Kolmogorov length and time scales. By dividing for the flow length and time scale, after few passages it is possible to state that

$$\frac{\eta}{L} = Re_L^{-3/4} \tag{4.2a}$$

$$\frac{\tau}{T} = Re_L^{-1/2} \tag{4.2b}$$

Hence, at sufficiently high Reynolds number there is enough separation between large and small scales and it exists a range of high wave numbers (or frequency) in which the turbulence is in a state of statistical equilibrium [1]. If this is the case the flow is considered fully turbulent, else, if the separation between the two scales is not well demarcated, that is if the Reynolds number is not big enough, highly correlated structures take place in the flow.

Kolmogorov's second similarity hypothesis proposes the existence of an intermediate scale at a wave number higher than the one of the large scales but lower than the one of the small scales which can be well defined only at very high Reynolds number. In this inertial range the statistics of turbulence are in equilibrium between their production and their dissipation term, and they depend only on the dissipation rate ϵ. This hypothesis yields to an expression for the sub-inertial energy spectrum [20]

$$E\big(\kappa\big) = \alpha\epsilon^{2/3}\kappa^{-5/3} \tag{4.3}$$

where α is a non-dimensional universal constant and κ the wavelength. Thus, by looking at the turbulent energy spectra, several slopes may be identified. A typical spectra is shown in figure 4.1.

Turbulent flows are by nature chaotic. This precludes the possibility of having two equal velocity components in different flows at the same time and location. Therefore, in order to compare or quantify turbulent flows it is necessary to adopt a statistical approach.

Any deterministic model used to describe turbulence is based on statistical data, hence a study in turbulent flows is complete and satisfying only when statistical measurements are also carried out.

General statistical description of turbulent flows involves correlation functions, probability density functions and spectra. These three functions fully describe the nature of turbulence and high order statistical moments such as length and time scales, turbulent kinetic energy and its dissipation rate, turbulence intensity etc.

The first or zero order statistical moment is the average or mean and it is the simplest quantity that may be computed from a signal. Ideally, when we deal with turbulent flows, the statistical moments should be determined by ensemble

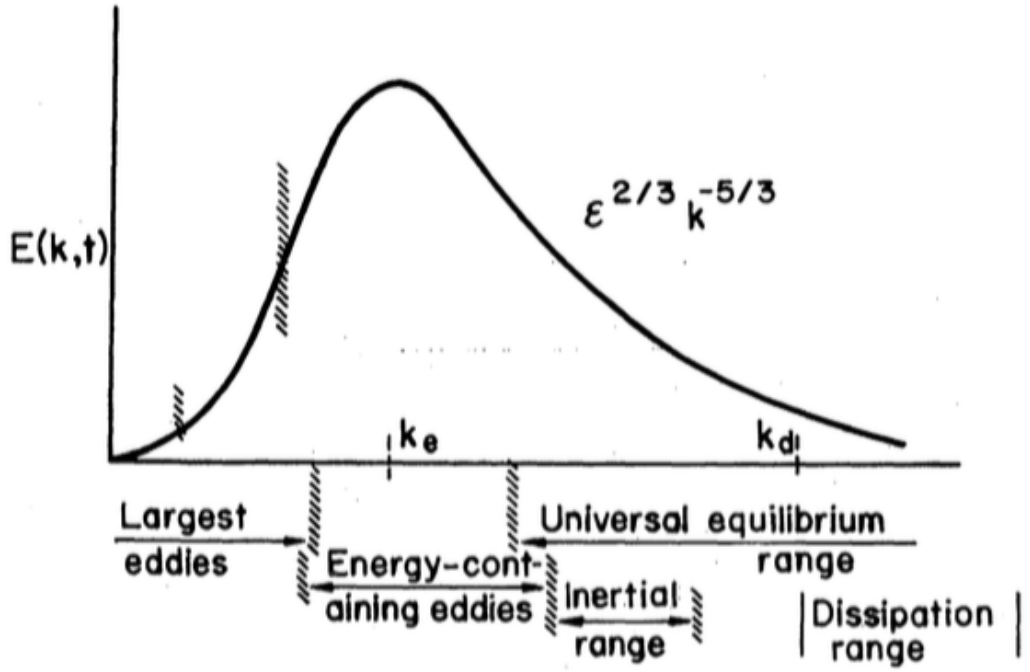

Figure 4.1: Typical turbulent spectra in which the slopes for the scales in the inertial sub-range and in the dissipative range may be distinguished [1]

average of a number of populations of different observations, however in experimental situations this is not always possible and an average on a finite number of samples over a finite time period is instead performed, attempting to represent the ensemble average [21]. Thus the mean is accounted as

$$\overline{\mathrm{U}} = \lim_{t\to\infty} \frac{1}{t} \int_0^t \mathrm{U}(t)\,dt \tag{4.4}$$

where U is the axial-component of velocity V. Since a one dimensional hot wire is used, from now on the velocity is always accounted as its axial-component U.

The root mean square (RMS) value of the velocity signal is roughly an average of the fluctuating components of the velocity signal and it is defined as

$$\overline{\mathrm{u}'} = \lim_{t\to\infty} \left[\frac{1}{t} \int_0^t \left(\mathrm{U}(t) - \overline{\mathrm{U}} \right)^2 dt \right]^{1/2} \tag{4.5}$$

As already mentioned, turbulence is chaotic but not completely random. A certain degree of correlation arises from a turbulent flow process. As far as a one dimensional flow is concerned, a simple measure of the dependence of the velocity

signal amplitude at one time on the amplitude of the other signals at different times is given by the autocorrelation function

$$R_u(\tau) = \frac{\overline{\mathrm{U}(t)\mathrm{U}(t+\tau)}}{\overline{\mathrm{U}(t)^2}} \tag{4.6}$$

Similarly, the autocorrelation function can be also written in terms of spatial correlation. Thus the dependence of a signal amplitude in a certain location on the other signal amplitudes in other locations is given by

$$R_u(\chi) = \frac{\overline{\mathrm{U}(x)\mathrm{U}(x+\chi)}}{\overline{\mathrm{U}(x)^2}} \tag{4.7}$$

The properties of autocorrelation, as previously discussed, yield to the computation of the turbulent scales. For instance, the energy containing eddies are described by the integral length scale which can be computed as

$$L = \int_0^\infty R_u(x)\,dx \tag{4.8}$$

or in terms of time scales

$$T = \int_0^\infty R_u(t)\,dt \tag{4.9}$$

The degree of correlation will decrease with increasing distance, up to a distance where the autocorrelation goes to a zero value. This distance is of the order of the integral length scale.

The same information may be obtained by a Fourier transformation of a signal from the time domain into the frequency domain. Thus the energy contained in each eddy is described as a function of frequency or of wave length. The energy spectrum $E(f)$ is the fraction of the turbulent kinetic energy present in the frequency interval $\left[f, f+df\right]$ [1].

Finally, one of the most important functions is the Probability Density Function (PDF) from which several information can be extracted. The PDF quantifies the probability that a certain signal $\mathrm{U}(t)$ will have a value between the levels $\overline{\mathrm{U}}$ and $\overline{\mathrm{U}} \pm d\mathrm{u}$. This probability can be written as

$$Prob\left[\overline{\mathrm{U}} - d\mathrm{u} \leq \overline{\mathrm{U}} \leq \overline{\mathrm{U}} + d\mathrm{u}\right] = \int_{\overline{\mathrm{U}}-d\mathrm{u}}^{\overline{\mathrm{U}}+d\mathrm{u}} f_u(\mathrm{U})\,d\mathrm{u} \tag{4.10}$$

where f_u is the probability density function describing the shape of the velocity population in a diagram where the abscissa is the velocity amplitude and the

ordinate is the percentage with which the single velocity observation is detected in a time period. This diagram is known as histogram.

It is known how a completely random signal will exhibit a Gaussian or normal distribution with a zero mean and the function is defined by equation 1.2 here reported once again.

$$f(x) = \frac{1}{\sqrt{2\pi\sigma}} e^{\frac{-(x-\mu)^2}{2\sigma^2}} \tag{4.11}$$

Similarly, turbulent flows in steady state with equilibrium between production and dissipation would present a Gaussian distribution with a mean value of velocity and a standard deviation (second order statistical moment) representing the RMS of the fluctuations of equation 4.5. Hence a deviation from normal probability density function may be thought as a deviation from the equilibrium itself [1]. This deviation is accounted by the third order statistical moment factor, usually called skewness and the fourth order statistical moment factor, also called kurtosis.

$$Skewness = \lim_{t\to\infty} \frac{1}{t} \int_0^t \frac{\left(\mathrm{U}(t) - \overline{\mathrm{U}}\right)^3}{\overline{\mathrm{u}'}^3} dt \tag{4.12a}$$

$$Kurtosis = \lim_{t\to\infty} \frac{1}{t} \int_0^t \frac{\left(\mathrm{U}(t) - \overline{\mathrm{U}}\right)^4}{\overline{\mathrm{u}'}^4} dt \tag{4.12b}$$

The skewness indicates an asymmetry of the PDF from a Gaussian and it is zero for normal distribution, while the kurtosis is a measure of the flatness of the PDF and it is equal to three for a normal distribution. Skewness provides us with useful information, e.g. a positive one may indicate a deviation from the equilibrium between production and dissipation of turbulent energy [1] or, in the near-wall region, can imply enhanced sweep events where flow separation may occur [22], or else, high skewness may stand for high correlated structures in the flow.

4.2 Inlet Characterisation

The inlet of the turbine test rig aims to represent the flow condition of an aircraft engine at the exit of the combustion chamber, in all the flight situations. Typically at this state the flow is conducted in the turbine by s-shaped ducts and its conditions are quasi or fully turbulent.

The hot-wire technique is employed to measure instantaneous velocity, from which a Reynolds decomposition in mean and fluctuating components may be

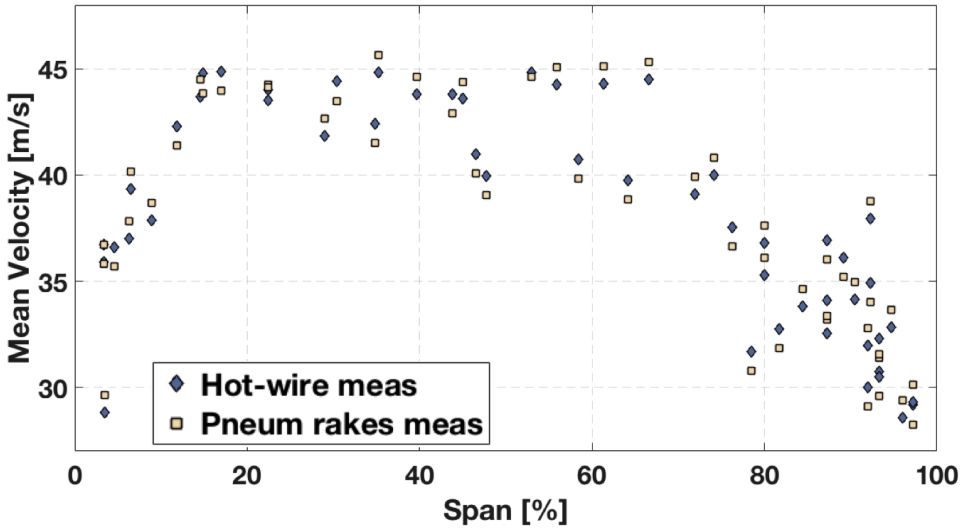

Figure 4.2: Mean Velocity distribution along the blade height

accomplished. Thanks to the high instrument's frequency response the turbulent spectra is computed up to the highest frequency fluctuations allowing to determine the smallest turbulent time and length scales.

A complete traversing has been performed in order to have information along the channel height of 74.71 mm. It was not possible to characterize the inner part of the boundary layer because of the probe design, which did not allow to take measurements at span lower than 3% and higher than 97% from the hub, nevertheless boundary layer characterisation is beyond the scope of this study.

At all the measurement locations a very good agreement in mean velocity computed with the hot-wire and the one derived from the pneumatic rakes was obtained and the results are shown in figure 4.2.

It must be reminded that every point in the figure represents a distinct test which may differ from the others because of variation in ambient conditions, in flow stability after the shutter valve opens or in spurious disturbance of the flow. At the time when this thesis was written only few tests for each point along the span were performed, thus, in order to have a good estimation of the mean velocity and other statistics trend, more tests have been planned allowing to check the repeatability of the results.

Nevertheless, some information may be obtained. It is plain that the mean velocity is higher at position closer to the hub than to the tip according to radial equilibrium theory. Indeed, static pressure is quite higher at the upper part of the channel rather than the one measured with the hub inserts.

Furthermore, decreasing values of mean velocity are detected at span location

lower than 5% and higher than 90% where the flow may be affected by boundary layer viscous stresses giving the impression of a thinner boundary layer at the hub compared to the tip.

From Reynolds decomposition of the instantaneous velocity the fluctuating components of velocity and, therefore, all the turbulent statistics may be computed.

$$\mathrm{u}' = \mathrm{U}\big(t\big) - \overline{\mathrm{U}} \tag{4.13}$$

The turbulence intensity, also often referred as turbulence level, is a measure of the level of unsteadiness in the flow in a precise period of time. It is defined by the ratio between the root mean square of the velocity fluctuations computed with equation 4.5 and a reference mean velocity.

$$T_u\big[\%\big] = \frac{\overline{\mathrm{u}'}}{\overline{\mathrm{U}}} \times 100 \tag{4.14}$$

Its value is of paramount importance for aerodynamic and thermal performance of an aircraft engine. A high turbulence level reduces the risk of flow detachment, energizing the boundary layer. This is an advantage mainly for compressors where an adverse pressure gradient is present. Furthermore, during an investigation of tip clearance flows in an axial turbine, Xiao et al [2] predicted weaker tip leakage and less losses for high upstream turbulence level.

The most significant issue in high pressure turbines is the very high temperature at which the flow operates. As far as thermal performance is concerned, a

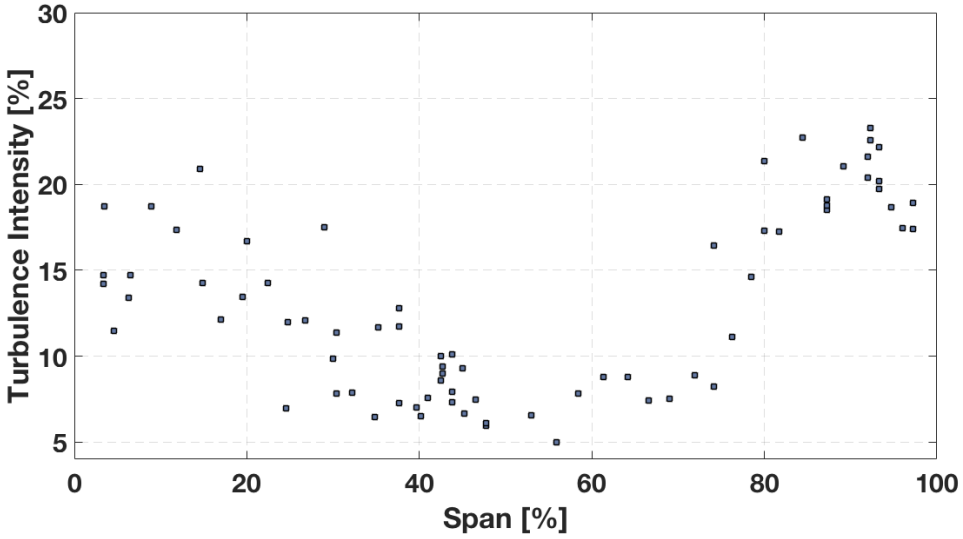

Figure 4.3: Turbulence Intensity distribution along the blade height

high turbulence intensity causes a more uniform distribution of temperature along the channel and increases the flow convective heat transfer coefficient h. In a computational study on the turbulence intensity influence on the heat transfer of a high pressure turbine stage, Wang et al [3] predicted a beneficial temperature reduction of the blades and casing wall, due mainly to the better distribution of temperature along the channel height, in flows with a turbulence intensity of 20% compared with a 5% turbulence level flow.

Indeed the most critical part to cool down inside a turbo-machinery is the tip of the blade and the tip end wall of the casing due to the higher difficulty in reaching them with cooling systems. Furthermore, the tip is also affected by higher temperature flows with respect to the hub according to radial equilibrium theory. Hence, a higher turbulence intensity has found to be beneficial to both aerodynamic and thermal performance.

In the turbulence intensity definition it is possible to use two values for reference velocity at the denominator of equation 4.14. The first is a reference value taken as the free stream velocity in the midspan, while the second choice is to use the local value of mean velocity. In the present work, due to the relatively high variation of mean velocity along the span and the non perfect repeatability caused by the low number of tests up to the time when this thesis was written, the local mean velocity is used as reference value. Figure 4.3 depicts the turbulence intensity at the inlet of the VKI's CT3 facility. The turbine stage is characterised by a turbulence level between 5% and 10% at a span from around 20% to 80% of the blade height, while it is up to 20% near the walls. The highest values are registered at the tip.

4.3 Time and Length Scales

As previously stated, turbulent flows are characterised by vortices of different size. The largest eddies are influenced by the geometry and the boundary conditions and they are responsible for the energy transport and mixing. On the contrary, the smallest scales are only influenced by local properties, such as the viscosity and the rate at which the turbulent kinetic energy (TKE) is transported and dissipated in internal energy. Thus they present a universal behaviour whether the mean flow boundary conditions may be.

The production of the large eddies is ascribed to large strain rate, that is high velocity gradient in one direction. At the inlet of the turbine, secondary flows are still not developed and the most important strain is in the direction of the blade height. Hence, a one-dimensional study as the one proposed could be a good approximation. The largest strain rate expected in this turbine section results from the two end wall boundary layer interaction with the mainstream flow.

The integral length or time scales represent the distance or the time at which

two velocity fluctuations are no more correlated and they can be computed by means of the autocorrelation factors as previously stated from the equations 4.8 and 4.9. Since the signals are reported in time it is more appropriate to discuss in terms of time scale. The conversion between the two is done thanks to the Taylor *frozen* hypothesis for which the length scale is proportional to the time scale by only means of a convective mean velocity.

$$L = T\overline{\mathrm{U}} \tag{4.15}$$

Obviously, in an experimental measure, the integration is only possible in a finite interval of time and all statistical quantities are computed with a numerical integration over the number of samples forming the signal. In the present work the integration is computed in the time interval when the signal is stable during the blow down as shown in figure 3.7. For instance, given N the number of samples, the mean velocity is accounted as

$$\overline{\mathrm{U}} = \frac{1}{N}\sum_{i=1}^{N}\mathrm{U}_i \tag{4.16}$$

The determination of the integral scales from the equation 4.9 is not straightforward. The form of the autocorrelation function is such that it rapidly decreases to zero, after which it may become negative and proceeds to oscillate about zero.

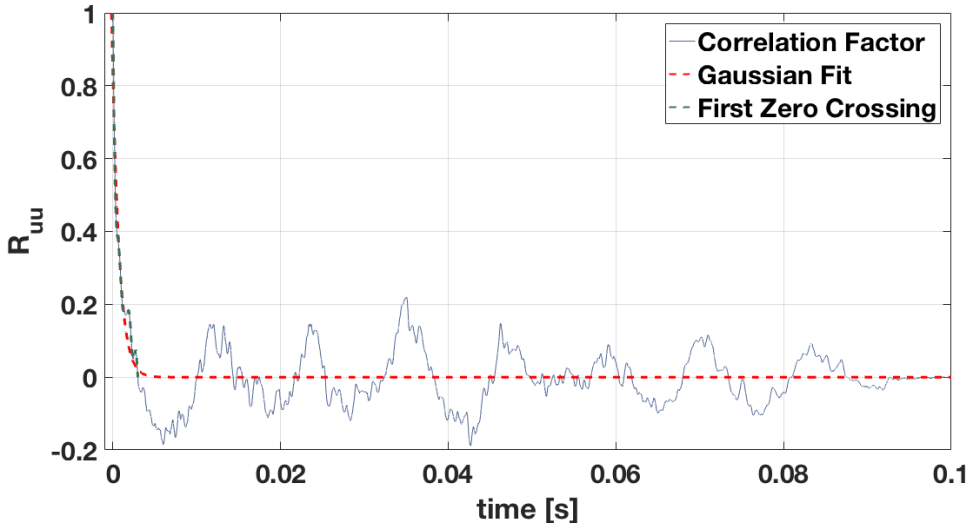

Figure 4.4: Autocorrelation factor (blu), Gaussian fit of $R_u(t)$ (red dashed line) and first zero crossing (green dashed line)

In the present work the autocorrelation of velocity fluctuations, at the turbine inlet and at the limited time interval in which it is integrated, was found to be as the one of figure 4.4 in which wide oscillations are present about zero.

There are different methodologies used to compute time scales from the autocorrelation function, all of them widely utilized. The most common involve a numerical integration of the equation 4.9. However, if $R_u(t)$ presents a negative undershoot, the integration yields to numerical cancellation and to an erroneous estimation of time scale. In this case it is possible to integrate a Gaussian fit of the autocorrelation function or to integrate the autocorrelation function only up to the time when it reaches the zero or, alternatively, when it reaches the minimum value of the first negative undershoot. One more method is to integrate the autocorrelation function up to the time when $R_u(t)$ reaches the value e^{-1}.

However, it is known, and it was demonstrated in an experimental study with PIV [23], that integral time scale computed from the autocorrelation function is only accurate when the integration is performed over a large enough time step. If the time domain is composed by a limited number of samples the integral may lead to an erroneous estimation of time scales.

Furthermore, in his study, O'Neill [23] states that wide oscillations can be described as *spurious* if a small number of data points are used and they may derive from numerical errors in the autocorrelation computation. The error, in this case, exceeds the quantity being estimated. From figure 4.4, therefore, the time scale computed from the longitudinal autocorrelation has to be considered unreliable, and a different methodology must be adopted.

An example of different approach is the wavelets-based dominant scales methodology. It emerged in the recent years as an alternative to classical longitudinal autocorrelation function in order to detect integral length scales. It was successfully employed for unsteady and periodic flows at the rotor exit of a low pressure turbine rig by Lewalle et al [24].

Another validated solution is to adopt a Fourier transformation and compute the integral time scale from the Power Spectral Density function (PSD) as proposed by Roach [25] and experimentally applied by El-Gabry [26].

The latter methodology will be employed in the present work, although it makes use of a strong assumption of isotropic and homogeneous turbulence.

The integral time scale is a measure of the largest and most energetic eddies in a turbulent flow. Hence, it is computed as a function of the spectral energy at zero frequency where the maximum amount of energy is expected in a truly isotropic turbulent flow.

$$T = \left[\frac{E(f)}{4\overline{\mathrm{u}'^2}} \right]_{f \to 0} \tag{4.17}$$

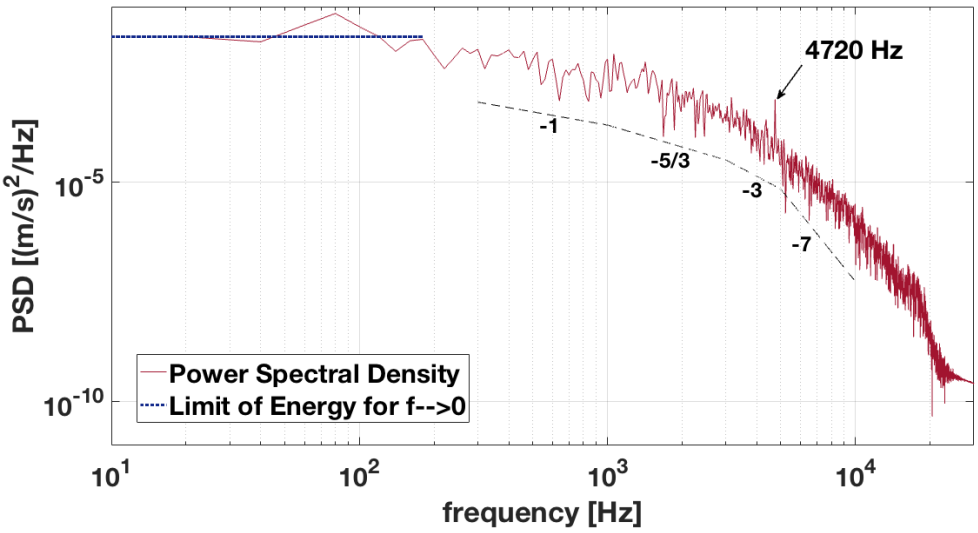

Figure 4.5: Power Spectral Density and the averaged energy at frequency tending to zero for integral time scale computation

The integral length scale L is then computed with the Taylor frozen hypothesis (equation 4.15).

In order to compute the energy at the zero frequency $E(f)_{f\to 0}$, the power spectral density is averaged up to the frequency where an asymptotic trend is detected. As it is shown in figure 4.5 the spectrum is averaged up to a frequency of 250 Hz.

The amplitude of the spectral energy, and the time scale deriving from it, was computed with the Fast Fourier Transform (FFT) by means of the software ®Matlab. Furthermore, an Hamming windowing is implemented with the ®Matlab function *pwelch*, in order to have higher spectral resolution and to avoid spectral leakage. Given the length of the signal of 12000 samples, a number of 6000 windows with a 50% overlap is applied. This gives the best compromise between spectral resolution and clearness of the spectra.

The spectra is depicted up to 30 kHz corresponding to the cut-off frequency after which only white noise was registered. The power spectral density (PSD) shows the typical trend of a developed (or quasi-developed) turbulent flows in which all the typical slopes can be disclosed. After the frequency ascribed to the integral time scales, there is the f^{-1} slope of the exponential turbulent decay, where the energy content starts decreasing. Next, a full $f^{-5/3}$ slope is appreciable, consisting of the scales of the sub-inertial range, responsible for the turbulent kinetic energy transport in the so called *energy cascade* at approximately 1 to 5 kHz. Finally the f^{-7} slope is present around 6 to 15 kHz related to the dissipative

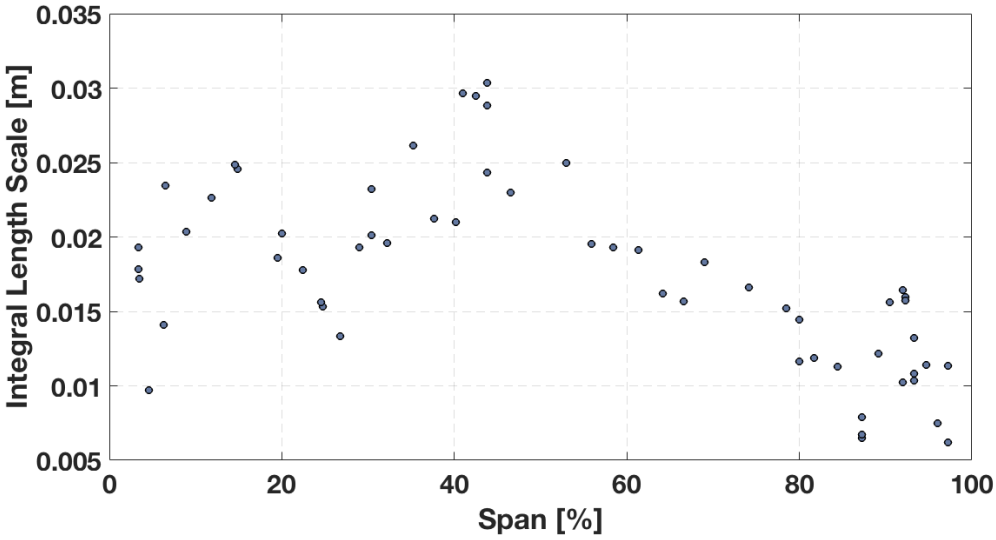

Figure 4.6: Integral Length Scale distribution along the blade height

scale.

A spike at around 4720 Hz can be clearly identified at almost every test. Although the signal is referred to the inlet condition, this spike is attributed to the reflected pressure waves generated by the blade rotation of the rotor. Indeed the rotational speed of the turbine rotor is around 5900 RPM at the time the measure is acquired for a number of rotor blade equal to 48 corresponding exactly at a blade passing frequency of 4720 Hz.

The integral length scale is a measure of the largest eddies and it depends on flow boundary conditions and geometry, thus it is expected, in a quasi axial symmetric geometry, that the maximum value of integral length scale is of the order of half the inlet section height, which is around 74 mm. In figure 4.6 is reported the integral length scale computed with equation 4.17 for a full traverse and the results meet the expectations.

It is worth reminding that each point is related to a different test, thus a perfect repeatability is only achievable with a much larger number of tests, however it is possible to observe a defined distribution along the span. The maximum is around 40% of the span. High value of integral length scale are associated to low turbulence intensity and high energy containing flow structures, while lower value of integral length scale are ascribed to higher flow strain interaction, where the fluctuations and the anisotropy is maximum, and thus they represent the region where the turbulence production and dissipation is maximal.

As far as the micro length scales are concerned, Roach [25] defines them as a measure of the average dimension of the eddies which are mainly responsible

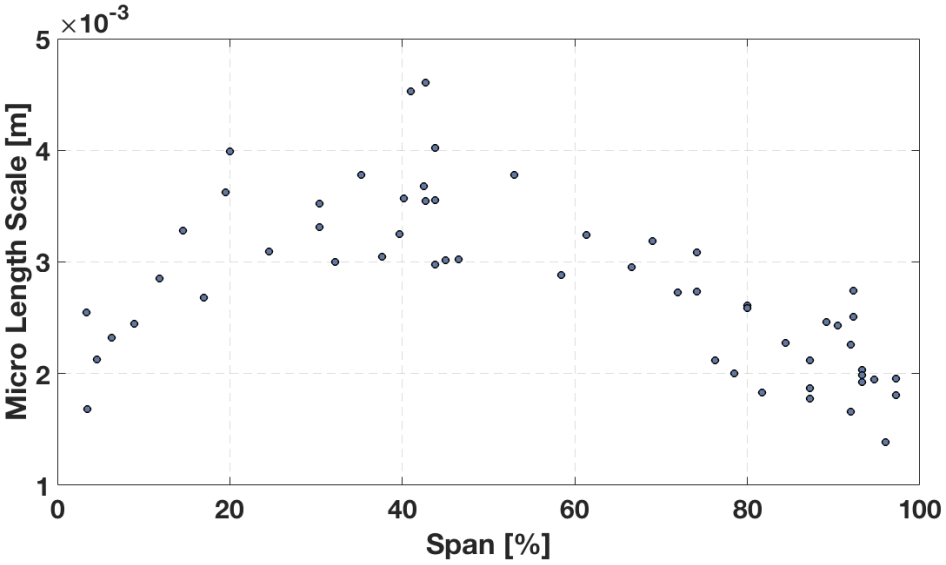

Figure 4.7: Micro Length Scale distribution along the blade height

for the dissipation of turbulent energy. Therefore, by looking at the spectra of figure 4.5, it is possible to expect their energy content to be at a frequency in the range of $3 \div 5$ kHz, where the f^{-7} decay starts. With the assumption of isotropic and homogeneous turbulence it is possible to compute the micro scales λ with the formula,

$$\frac{1}{\lambda^2} = \frac{2\pi^2}{\overline{\mathrm{U}}^2\overline{\mathrm{u}'}^2} \int_0^\infty f^2 E(f) df \tag{4.18}$$

where the integral is computed by means of a numerical integration, using the trapezoid rule with the ®Matlab function *trapz*.

In high Reynolds number flow these micro scales will be, then, larger than the Kolmogorov one, which are the smallest scales in the flow ascribed to the highest frequency in the spectra, and which may be computed with the equation 4.2a. The results in terms of micro scales are shown in figure 4.7. Also in this case the maximum is detected around the 40% of the span where the largest flow structures are present. The values of the micro length scales measured fall in the range of frequency expected, computed as

$$f_\lambda = \frac{\overline{\mathrm{U}}}{2\pi\lambda} \tag{4.19}$$

Chapter 5

Uncertainty Analysis

The process of measurement involves disparate sources of error. When dealing with hot-wire and any other intrusive instrument, the first element to take into account is the change in the flow field generated by the flow-probe interference. Beside this aspect, which is difficult to quantify, the other sources of error are the following:

- The probe is characterised by a finite length of the order of 1 mm. Hence, the results are not referred to a single point but they are averaged over a finite volume. The smallest length scales in turbulent flows can reach value lower than 0.1 mm. When this is the case the error in turbulence intensity and length scales can be of the order of 10% [25]. This error is accounted as spatial resolution.

- As seen in section 4.3, the micro length scales are evaluated from the power spectrum by an average over a broad frequency bend, while it is the highest frequency end of the spectrum which characterises the major contribution in the dissipation time scales. This gives an error in the micro scales if the integral of equation 4.18 is not computed over a sufficiently large frequency band.

- Common flows are characterised by a variety of frequency components. On the contrary, the probes have an upper limit beyond which it does not recognize the signals and a lower limit below which measurement is not performed. As stated by Biswas [1] a probe with cut-off frequency f_2 and lowest frequency limit f_1 must measure for a duration at least $5/f_1$ seconds so that at least 5 cycles of the lowest harmonic is included in the averaging process. Further, the sampling rate must be at least $2f_2$ according to the Nyquist criterion.

- Other sources of error are the finite precision of the calibrated curve, the round-off errors during computer-based data reduction or during the reading

of data points from visual instrumentations. Moreover, errors may come from spurious events such as instruments vibrations, change in materials conditions or electronic interference, which cause a deviation of the actual value of the signal, beside human errors, which can always occur.

It is important to distinguish between error and uncertainty. The first one defines the difference between the measured value and the true value and remains unknown, while the uncertainty refers to an estimate of the error by introducing a confidence interval in which it is expected to find the true value with a certain percentage of confidence level and it is the only quantifiable parameter.

Two widely accepted standard methodology are available to deal with uncertainty quantification, these are the ISO Guide to the expression of Uncertainty in Measurement (GUM) and the ASME methodology. The difference between the two procedures is the grouping of uncertainty sources. In this study the ASME method is considered advantageous in traceability of uncertainty terms, which are divided in two well defined groups,

1. Systematic errors, which are always present and remain the same during the experiments. These may be tolerances specified by manufacturers or calibration uncertainty of the instrument used in a measurement. Systematic errors represent the bias of the true value with respect to the measured one.

2. Random errors, which cause a scatter in the measurements' results affecting the data in a completely random way. These errors are accounted by a standard deviation from the mean value by knowing the probability density distribution of the measured population.

Systematic errors will be identified with the letter b while random errors with the letter s. If more than one component of e.g. systematic uncertainty sources are present, say N contributions, these are combined by mean of a root mean square value as $b = \left(\sum_{i=1}^{N} b_i^2\right)^{1/2}$.

If the collected data fit a Gaussian distribution, the three-sigma rule is applicable. Thus, approximately 68.27% of the values lie within a standard deviation σ of the mean μ, 95.45% of the values fall within two times the standard deviation, and roughly 99.72% of the values are comprised within 3σ.

The sample standard deviation, referred as random uncertainty s is computed as

$$s = \sqrt{\frac{\sum_{i=1}^{N} \left(X_i - \overline{X}\right)^2}{N-1}} \tag{5.1}$$

where N is the number of samples of a single measurement.

The total uncertainty, identified with the letter U, will be then $U = \left(b^2+s^2\right)^{1/2}$.

It is common practice to express the uncertainty by its expanded value at 95% confidence interval for which the uncertainty is multiplied by a factor $\pm t_{95}$. If the number of samples is large enough and the combined degrees of freedom given by the Welch-Satterthwaite equation are higher than 30 [27], the t_{95} factor is equal to 2.

Finally, if the quantity of interest is not directly measured but it is derived from other quantities, say $C = f\left(c_1, c_2\right)$ the expansion technique is used for which the final uncertainty is given by propagation of the other measured uncertainty by means of a Taylor series expansion with a first order truncation, hence

$$U_C = \sqrt{\left(\frac{\delta C}{\delta c_1} U_{c_1}\right)^2 + \left(\frac{\delta C}{\delta c_2} U_{c_2}\right)^2} \tag{5.2}$$

If the two variables being measured are dependent one an other, a cross correlation term should be added in the equation.

5.1 Calibration Uncertainty

As described in chapter 2, the hot-wire probe is calibrated in a cold jet in combination with a K-type thermocouple and a Validyne pressure transducer, which uncertainty is respectively $U_{T_0} = 0.157$ K and $U_{p_0} = 6.78$ Pa computed with the methodology described in Appendix A. These uncertainties are used as systematic error sources in the quantification of the hot-wire calibration uncertainty.

During calibration, only the mean value of velocity are taken into account in the construction of the calibration curve. Thus, in order to avoid that physical velocity fluctuations are considered in the mean velocity uncertainty, the standard deviation of the hot-wire voltage signal acquired at *zero-flow* E_0 is considered as uncertainty in the mean voltage signal also when velocity fluctuations are present. E_0 was found to be 0.1 V, with the assumption that it remains constants when the flow crosses the wire. With this presumption the dynamic calibration will present similarity with classical static calibration for which normal distribution of samples is ensured.

The calibration uncertainty for the hot-wire is accounted as deviation from the actual Reynolds number computed on the wire diameter. The systematic error sources will be accounted as the calibration uncertainty of total pressure and total temperature, while the random uncertainty is accounted as static standard deviation of hot-wire voltage signal and quality of the data fit.

In order to evaluate the quality of the data fit given by a calibration curve as the one of the hot-wire of figure 2.13, the standard error estimate is used as

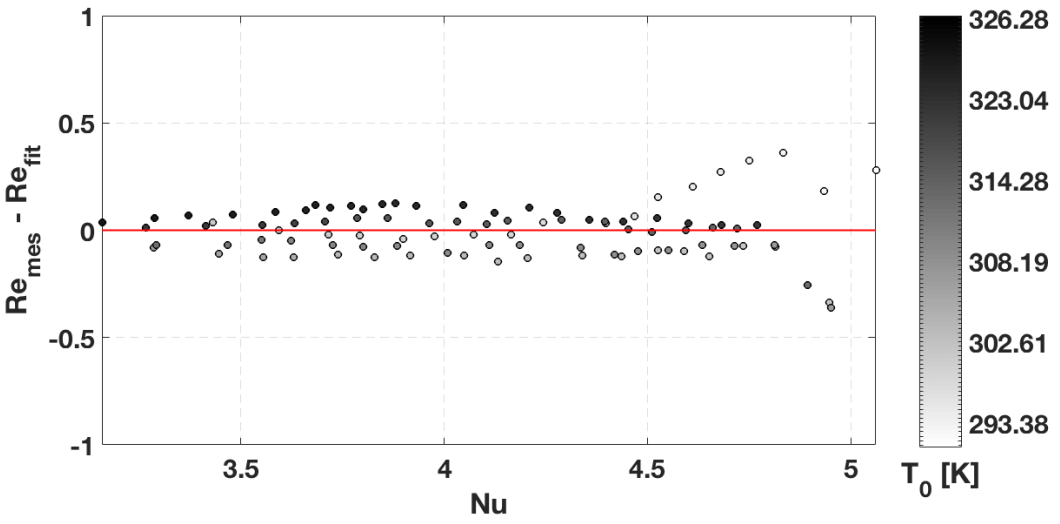

Figure 5.1: Deviation of calibrated points from the fitting calibration curve

indicated in reference [27] and defined as

$$SEE_{Re} = \sqrt{\frac{\sum_{i=1}^{N_{cal}} \left(Re_i - Re_{fit,i}\right)^2}{N_{cal} - K}} \tag{5.3}$$

where Re_i indicates the i_{th} measured point while $Re_{fit,i}$ stands for the i_{th} value calculated from the data fit and the difference is graphically shown in figure 5.1. N_{cal} represents the number of calibrated points measured and K is the number of coefficients used in the data fit (for the hot-wire calibration $K = 5$ since a 4_{th} order polynomial fit is used). The denominator in the equation 5.3, $N_{cal} - K$, represents the degrees of freedom of the random uncertainty source of the measured quantity M [27]. Finally, the random uncertainty derived from the not perfect quality of the fitting curve is given by

$$s_{\overline{Re}} = \frac{SEE_{Re}}{\sqrt{N_{cal}}} \tag{5.4}$$

Furthermore, the computation of the Nusselt number depends on the hot-wire voltage signal, the total temperature, the flow conductivity and the recovery factor as expressed in equation 2.23. The Reynolds number, on the other hand, depends on the flow viscosity, density and mean velocity as expressed in equation 2.13. Thus, a propagation analysis of all error sources in the computation of these dimensionless numbers must be applied. Hence,

$$U_{Nu} = \sqrt{\left(\frac{\delta Nu}{\delta \mathrm{E}_b} U_{E_0}\right)^2 + \left(\frac{\delta Nu}{\delta \mathrm{T}_0} U_{T_0}\right)^2 + \left(\frac{\delta Nu}{\delta \eta} U_{\eta}\right)^2 + \left(\frac{\delta Nu}{\delta \kappa} U_{\kappa}\right)^2} \tag{5.5}$$

$$U_{Re,meas} = \sqrt{\left(\frac{\delta Re}{\delta \rho} U_{\rho}\right)^2 + \left(\frac{\delta Re}{\delta \mu} U_{\mu}\right)^2 + \left(\frac{\delta Re}{\delta \mathrm{V}} U_{V}\right)^2} \tag{5.6}$$

The uncertainty for the flow properties appearing in equations 5.5 and 5.6 are computed by the propagation analysis formulated in appendix A.

Furthermore, the uncertainty of the calibration curve comes from error propagation of the Nusselt uncertainty on the fitting 4_{th} order polynomial curve, that is

$$U_{Re,fit} = \frac{\delta Re}{\delta Nu} U_{Nu} \tag{5.7}$$

The final calibration uncertainty in terms of Reynolds number is computed as the root mean square of the three component of uncertainty in Reynolds number given by the equations 5.4, 5.6 and 5.7. Given the high number of samples and much more than 30 degrees of freedom, the 95% extension of uncertainty for the hot-wire calibration is given by

$$U_{Re} = \sqrt{U_{Re,fit}^2 + U_{Re,meas}^2 + s_{\overline{Re}}^2} \tag{5.8a}$$

$$U_{Re,95} = 2U_{Re} \tag{5.8b}$$

It is important to point out that the uncertainty in the measured wire resistance and temperature of the wire were not included in the computation of the Nusselt number uncertainty, in a first moment. The dependency on the wire resistance was neglected since an error of even 10% in the measured resistance resulted in no change in the final calibration curve. As far as the wire temperature is concerned, its uncertainty is evaluated by a perturbation analysis. For this analysis, every measured quantity is perturbed up to its 95% uncertainty value and the iterative process described in section 2.4.1 is repeated. A new calibration curve is found and the $U_{Re,95}$ is calculated as described above for the highest and lowest T_w. Finally, the result in terms of calibration curve uncertainty with 95% confidence level is shown in figure 5.2.

The most significant source of error was found to be the error propagation from the other measured quantities of equation 5.6. This error can only be reduced by increasing accuracy in the instrumentations utilized.

The quality of the fitting computed with equation 5.4 can be reduced if a larger number of calibrated points is exploited.

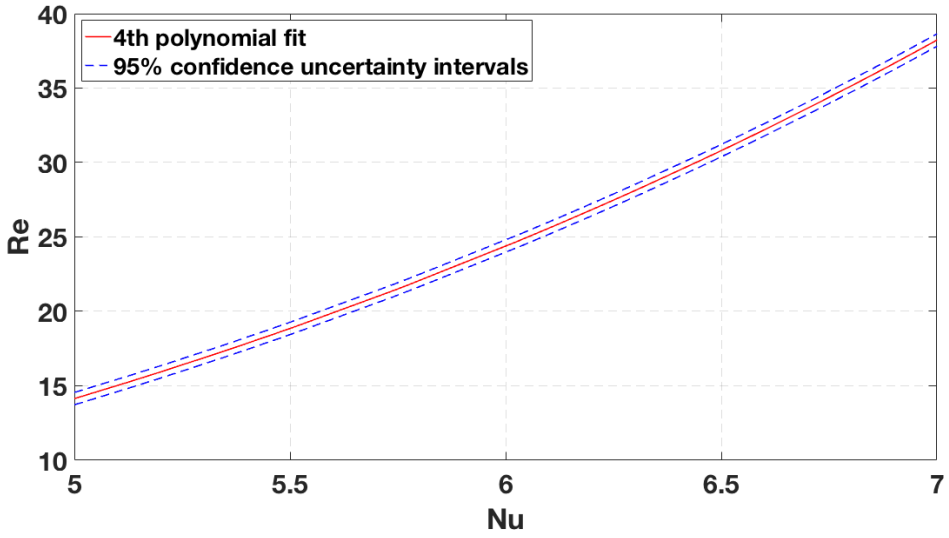

Figure 5.2: Hot-wire calibration curve with 95% confidence level

5.2 Measurements Uncertainty

The same distinction between systematic and random error sources is maintained for the uncertainty quantification of the measurements performed in the VKI's CT3 facility.

Systematic errors for hot-wire results are those which remain in all measurements. These are uncertainty in measured total temperature, total pressure and static pressure and the uncertainty value obtained for the calibration.

From a perturbation analysis it was found that total pressure and static pressure uncertainties are negligible compared to the uncertainty in total temperature. The latter is considered to be the result of the scatter between the two methodologies applied in the total temperature computation described in section 3.3. It is of the order of 2 K in the whole span except for the wall proximity where it may be up to 6 K.

As far as the random uncertainty term is concerned, it is imperative to understand that in dynamic, unsteady and turbulent conditions it is impossible to ensure a Gaussian distribution of the velocity samples. The result in terms of velocity computed with hot-wire is shown, for one test, in the histogram of figure 5.3. It is evident the deviation from the normal distribution with a high positive skewness.

In general positive skewness provides us with a useful information, indicating a deviation from the equilibrium between production and dissipation of turbulent energy [1]. Drozdz [22] showed that a positive skewness in the near-wall region can

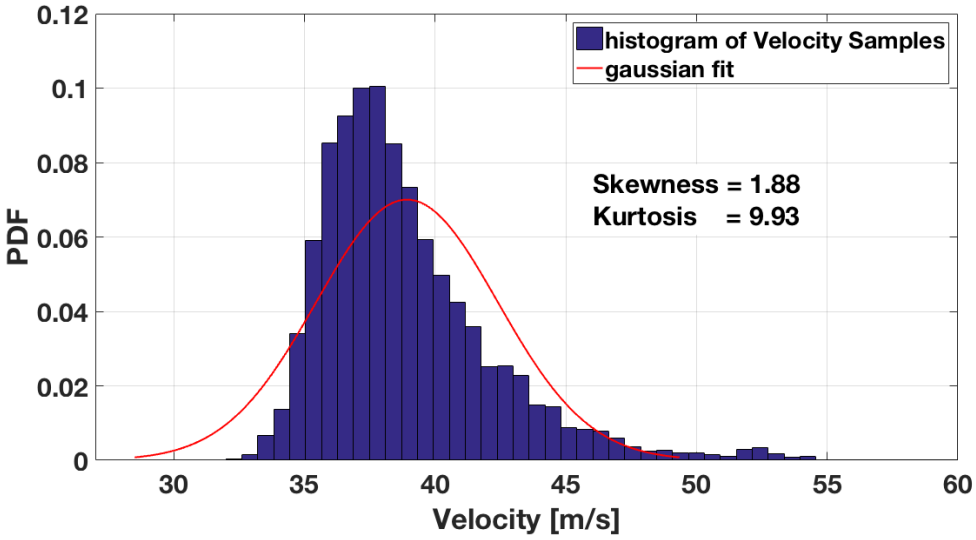

Figure 5.3: Histogram of velocity samples

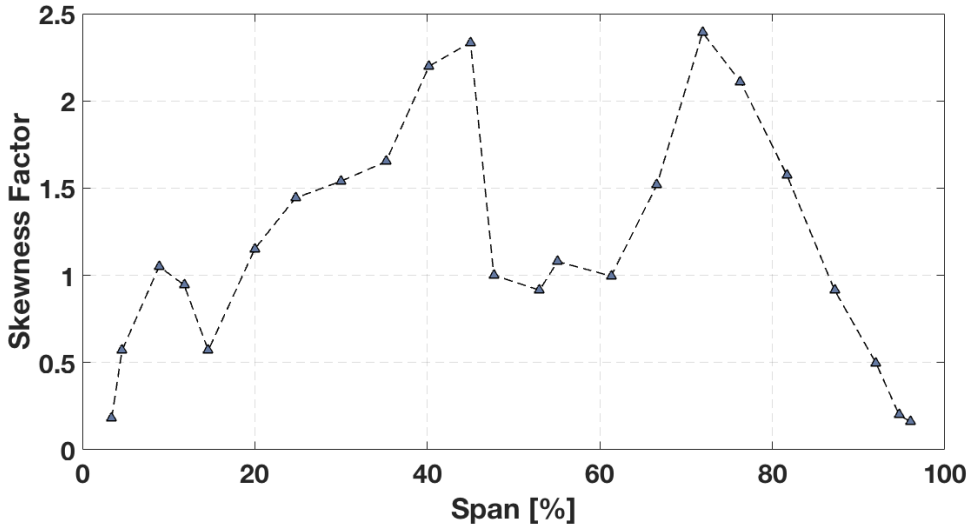

Figure 5.4: Skewness of velocity samples distribution along the span

indicate enhanced sweep event where flow separation may occur or may reflect the presence of high shear stresses imposed on a background of lower turbulence level. Dell'Era et al [27] ascribed high skewness in an axial compressor inlet to zones where higher pressure vortex structures are present. Furthermore, high skewness may stand for high correlated structures; indeed higher skewness is found in region where higher integral length scale is computed, as it is shown in figure 5.4.

As far as a skewed probability density function may give information about the physic of the flow, it can not be used to compute the random source of uncertainty. In literature, many attempts have been made to give a reference for unsteady measurements uncertainty. Dell'Era [27] makes use of a transformation of the signal by sorting it in ascending order, computing the median and calculate the inverse of a cumulative distribution function with mean equal to the median itself and standard deviation estimated with the assumption of Gaussian distribution. On the other hand Derksen [28] suggests to not assuming a Gaussian distribution but to over-impose a distribution to the turbulent statistic by means of the maximum statistical entropy approach. Lenschow [21] computes the higher order statistical moments by assuming that the autocorrelation function can be represented with an exponential distribution and then an analytical expression is provided.

The methods proposed by the above mentioned scholars have in common the use of a parametric approach to the problem; hence, a hypothesis on the distribution of the parameters is developed. In this project a non-parametric approach is proposed, thus the turbulent statistics are computed with their uncertainty without any hypothesis on the probability density function. The methodology is a re-sampling technique developed by Efron [29] in an econometric field, called Bootstrap. An enhanced version of it, the Moving Block Bootstrap proposed by Künsch [30], is used in order to ensure that correlation between samples remains untouched.

5.2.1 General Principle of Bootsrtapping

Statistic should answer to three questions when dealing with measurements: How to collect data? How to analyse these data? How accurate are these data?

The Bootstrap re-sampling technique attempts to answer the latter question computing the statistical inference. In other words it is a way to measure accuracy – in terms of variance, error prediction, confidence intervals – of samples estimates by means of a computer-based algorithm [31].

The main idea is that inference about a population of sample data may be modelled by performing inference on a re-sampled group of these data in a random fashion. It is formally used when the distribution of a statistic of interest is unknown, or when the sample size is not sufficient to compute direct statistical inference [31].

On the contrary, parametric theories for statistical inference require assumptions on the distribution function. Once the PDF is assumed or known, it is possible to compute from a sample data set $\boldsymbol{x}$ a sample mean, say $\overline{X}$, as prediction of the true value μ and a standard error σ. For instance, for normally distributed N samples, it is possible to define the standardized z-score pivotal quantity as

$$z = \frac{x - \mu}{\sigma} \tag{5.9}$$

z will have mean equal to 0 and variance equal to 1. Moreover, the central limit theorem states that, for normal distributed samples, the sample mean is also normally distributed with standard deviation $\sigma/\sqrt{N}$ and the z-score of the mean will be

$$z = \frac{\overline{X} - \mu}{\sigma/\sqrt{N}} \tag{5.10}$$

Again the distribution of the z-score of the mean will have the same distribution with mean equal to 0 and variance equal to 1.

It is, then, possible to evaluate statistical inference by the classical percentile method, for which approximately 95% of the time the true value will fall within 2 standard deviations.

$$\mu_{95} \approx \overline{X} \pm \frac{2\sigma}{\sqrt{N}} \tag{5.11}$$

It is evident that to evaluate confidence intervals for the mean value the second order moment must be known. In the turbulence community, when probability density function is not known, a usual way to deal with inference problem is to assume that the statistic of interest follows a normal distribution. Further estimation must be performed on the standard error of the parameter. In literature, few analytical formulations are available for the standard error estimation of higher than first order statistical moments such as variance, Reynolds stresses, third and fourth order moments [32], however their validity is ensured only for uncorrelated samples. Indeed, if samples are correlated the resulting confidence intervals would be narrower than they actually are [33].

Due to the necessity of high sampling frequency of the hot-wire signal, the measured velocity samples are highly correlated, thus classic statistical procedures are no more applicable.

One solution to this problem is to use a number of uncorrelated samples N_{eff} from the original data set of N samples. From these samples classical formultaions of normal distributed mean and variance can be exploited. In order to evaluate the value for N_{eff} from a recorded observation, an estimation of the integral time scale is required [10]. However, as stated in section 4.3, it is possible to compute time scale with different definitions and, as demonstrated by Theunissen [34], depending on the definition utilized, the value of N_{eff}, the value of the statistic of interest and its standard error estimate can be much different and thus highly unreliable.

Moreover, no equations are available for standard errors of more complicated parameters such as length and time scales, dissipation of TKE and micro scales [33].

On the other hand, the non–parametric Bootstrap overcomes these problems thanks to the following presumption: *if the sample is a good approximation of the population, the Bootstrap re-sampling method provides a good approximation of the sampling distribution* [31]. This theoretical justification lies on two levels of asymptotic:

1. *As the original sample size N approaches the population size, the empirical distribution function (EDF) approaches the true distribution (PDF)* [31]. Indeed, as a sample increases in size, it contains more and more information about the population.

2. *If the original sample size N is large enough, as the number of re-samples increases to infinity, the bootstrapped estimate of the sampling distribution approaches the sampling distribution of the original statistic* [31].

The procedure to extract mean and error estimate is described by the following steps [29] and depicted in figure 5.5,

1. Construct a sample probability distribution $\hat{f}$ by placing a mass $1/N$ at each point x_1, x_2,...,x_N of the time series $\boldsymbol{x}$. This is the non-parametric maximum likelihood estimate of the population distribution and thus, each sample has the same probability to be drawn.

2. From the empirical distribution found, draw a random sample of size N with a random replacement. In other words, create a new data series with the same observations randomly extracted from the original data series. This will be a Bootstrap sample series $\boldsymbol{x}^*$.

3. Calculate the statistic of interest θ from the bootstrapped sample series yielding to θ^*.

4. Repeat step 2 and 3 B times, where B is a large number which must be defined later on.

5. Approximate the sampling distribution of the statistic θ by the Bootstrap distribution of θ^* induced by the random mechanism.

6. Compute the mean and the standard deviation of the statistic θ^* from the Bootstrap distribution.

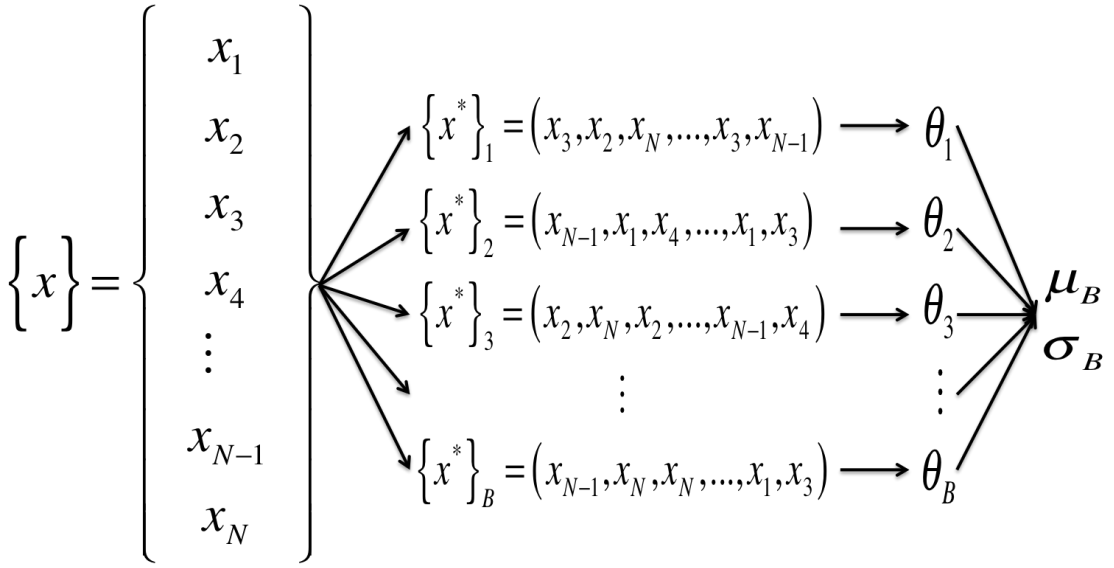

Figure 5.5: Principle of Bootstrap re-sampling technique

In other words, the construction of Bootstrap samples is performed with a Monte Carlo style procedure. Repeated realizations of $\boldsymbol{x}^*$ are generated by taking randomly samples of size N from $\hat{f}$.

The Bootstrap data set will thus consist of members of the original data set, some appearing zero times, some once, some twice or more times.

The histogram of the corresponding statistic θ_1^*, θ_2^*,...,θ_B^* taken from each Bootstrap series is taken as an approximation to the actual distribution [29].

Finally, the Bootstrap estimate of the standard error would be the standard deviation of the Bootstrap replications of the statistic θ, hence

$$\sigma_\theta^* = \left[\frac{\sum_{i=1}^{B} \left(\theta_i^* - \overline{\theta^*}\right)^2}{B-1} \right]^{1/2} \tag{5.12}$$

where $\overline{\theta^*}$ is the mean of the bootstrapped realizations of θ

$$\overline{\theta^*} = \frac{\sum_{i=1}^{B} \theta_i^*}{B} \tag{5.13}$$

Although bootstrapping is asymptotically consistent, the procedure described conceals an important assumption of sample independence. Indeed, re-sampling destroys any correlation between observations. This is a big limitation when dealing with turbulent statistics such as length scales which are strictly dependent on the correlation factor. For this reason an enhanced version of the Bootstrap must be used as described in the following section.

5.2.2 The Moving Block Bootstrap

As previously mentioned the Moving Block Bootstrap (MBB), ascribed to Künsch [30], ensures that correlation remains untouched. It consist in replacing the samples in block of length b instead of taking one sample per time randomly.

The data is split into $N - b + 1$ overlapping blocks and N/b blocks will be randomly drawn with replacement and aligned in order to construct a Bootstrap sample series of roughly the same size of the original data set.

This procedure is again repeated B times to get B Bootstrap series. From each of them the statistic of interest is computed and the probability distribution estimated.

However, two questions arise from what discussed up to now: how large should be the number of Bootstrap replications B in order to approximate the sample distribution well? And, how long should be the blocks in order to leave correlation intact?

As far as the number of replications B is concerned, Efron [31] stated that depending on the statistic of interest the value may vary. In particular, very seldom are more than $B = 200$ replications needed for estimating an error variance, while a much higher value (around 1000) are required for estimating a Bootstrap confidence interval.

In the present study, a sensitivity analysis is used in order to compute the number of B Bootstrap replications depending on the statistic of interest, on the

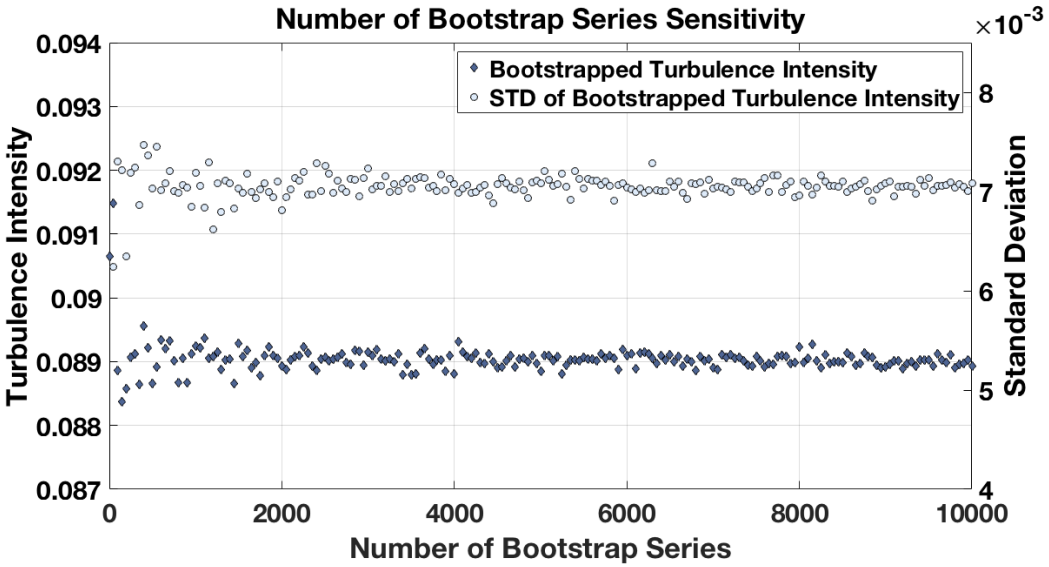

Figure 5.6: Mean and Standard Deviation of Turbulence Intensity depending on the number of Bootstrap series

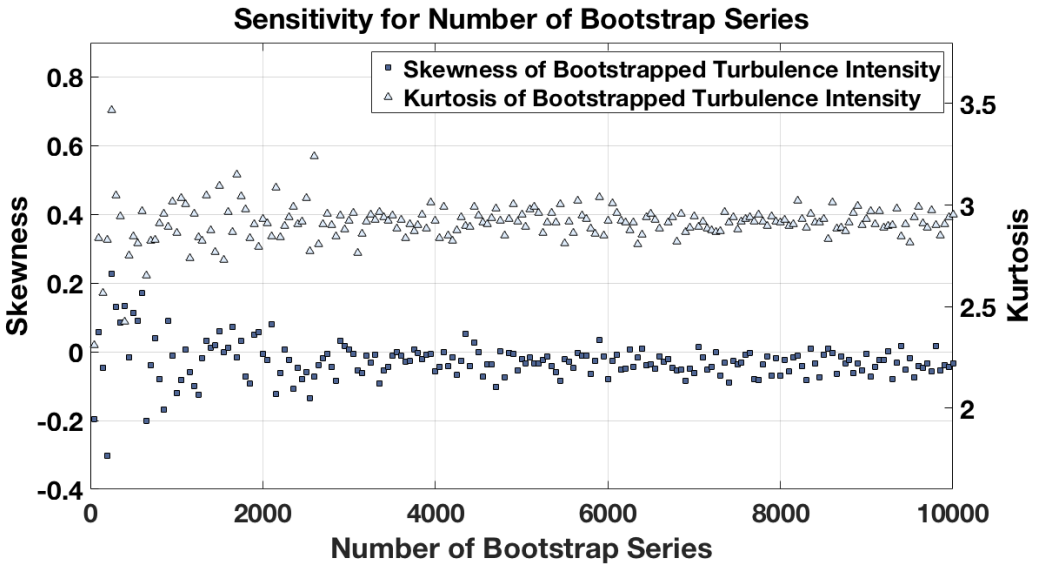

Figure 5.7: Skewnees and Kurtosis of Turbulence Intensity depending on the number of Bootstrap series

basic idea that Bootstrap replications asymptotically tend to a defined distribution whether the parameter one wants to estimate.

As a title of example, figures 5.6 and 5.7 show the dependency of the bootstrapped mean, standard deviation, skewness and kurtosis of the turbulence intensity on the number of replications B.

Results, especially the one for skewness and kurtosis, show the tendency to normality as the number of Bootstrap replications B exceeds 4000 for the turbulence intensity measured in the CT3 facility, while a number of 10000 B replications is required for length and time scales error estimation and confidence interval.

The histograms of the mean velocity and of the turbulence intensity resulting from bootstrapping the hot-wire velocity signal is shown in figure 5.8 and 5.9. It is evident that the empirical bootstrapped distribution can be easily compared to a Gaussian probability density function. Indeed skewness and kurtosis of the bootstrapped mean are roughly equal to zero and three respectively.

To answer the second question, concerning the number of samples b that each block should have to ensure intact correlation in the signal, Politis et al [35] proposed an automatic procedure for block length selection based on a first estimation of the autocorrelation function, and the time or length scale from the original signal, which is aimed at minimizing the mean square error of the standard error estimate.

The procedure is synthesized hereafter by the following steps [35]:

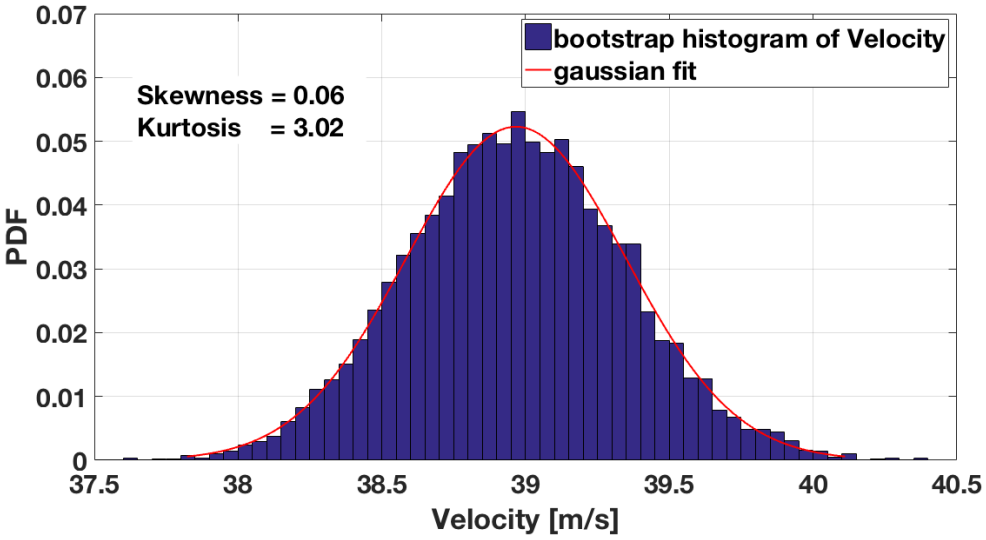

Figure 5.8: Histogram of bootstrapped mean velocity

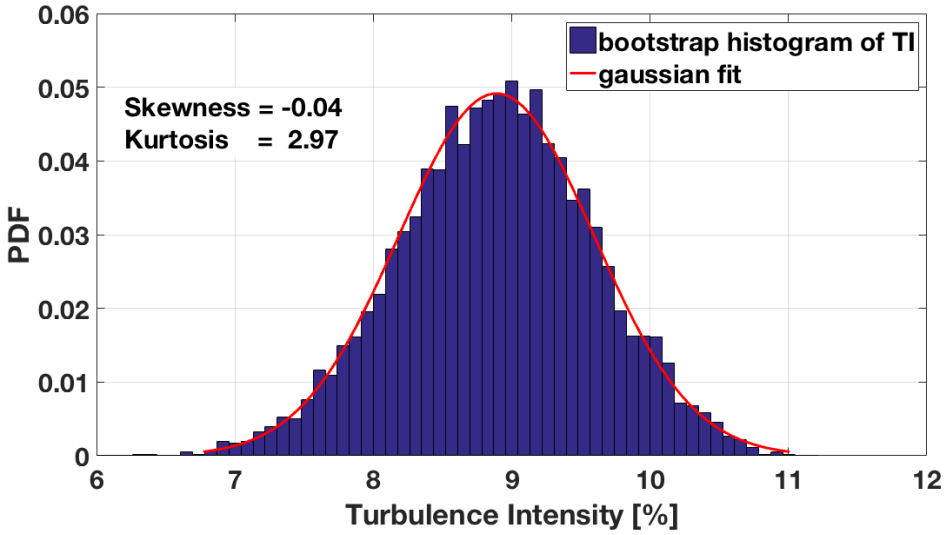

Figure 5.9: Histogram of bootstrapped turbulence intensity

1. Calculation of the unbiased autocorrelation function with equation 4.6.

2. Finding the smallest lag m for which the K_{th} consecutive value of the autocorrelation factor satisfies $R_x(m+k) \leq c\left(\frac{\log N}{N}\right)^{1/2}$ with $k = 0, 1, ..., K$ and $K = \max\left(5, (\log N)^{1/2}\right)$. c is a constant and it is generally equal to 2. It

basically consists in identifying the time lag after which the autocorrelation can be considered negligible.

3. The optimum block length b will be computed as

$$b = N^{1/3}\left(\frac{2G^2}{D}\right)^{1/3} \tag{5.14}$$

where the terms composing the equation are

$$D = \frac{4g^2(0)}{3} \tag{5.15a}$$

$$g(0) = \sum_{k=-2m}^{2m} \lambda(k/2m) \times R(k\Delta t) \tag{5.15b}$$

$$G = \sum_{k=-2m}^{2m} \lambda(k/2m) \times |k| \times R(k\Delta t) \tag{5.15c}$$

In these equations the term λ is computed as

$$\lambda(k/2m) = \begin{cases} 1, & \text{if } 0 \leq |(k/2m)| \leq 0.5 \\ 2(1 - |k/2m|), & \text{if } 0.5 < |(k/2m)| \leq 1 \\ 0, & \text{otherwise} \end{cases} \tag{5.16}$$

Once the optimum block length is computed, it is possible to construct the Bootstrap repetitions as described previously and from each of them compute the statistic of interest and its bootstrapped mean, standard deviation and confidence interval.

Garcia et al [33] validated the Moving Block Bootstrap with automatic block length selection by means of analytical formulation (when existing) and experimental results with acoustic Doppler velocimeter, with good agreement. However the automatic block length selection was validated in a fully developed and stationary turbulent flow for an extended period of time by means of a closed loop facility.

As already discussed in section 4.3, due to the limited time in which the measures are taken, the autocorrelation function presents wide oscillation around zero. O'Neill [23] stated that wide oscillations in autocorrelation function can be described as *spurious* if a small number of data points are used and they may derive

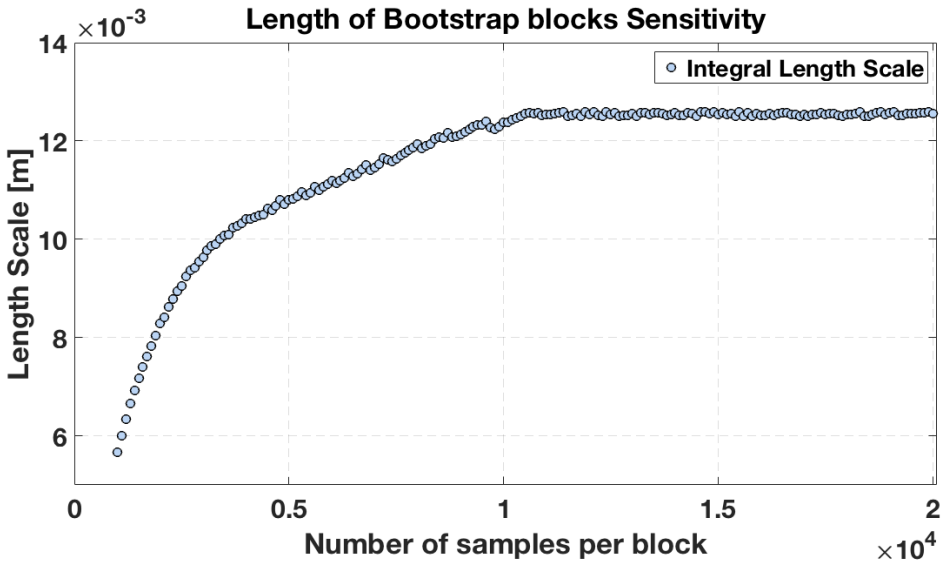

Figure 5.10: Mean of Integral Length Scale sensitivity depending on the Bootstrap blocks' length relative to an original signal sampled at 1 Mhz for the 0.1 seconds of test resulting in 100000 samples

from numerical errors in the autocorrelation computation. Indeed, he demonstrated that integral time scale computed from the autocorrelation function is only accurate when the integration is performed over a large enough time step. If the time domain is composed by a limited number of samples the integral may lead to an erroneous estimation of time scales. On the other hand high oscillation may indicate large correlated structures and again, if the time in which the autocorrelation is computed is not large enough it may lead to an underestimation of the block length. Therefore, as asserted by Theunissen [34], when the autocorrelation function is affected by strong oscillations, it is preferred to use a conservative block length selection.

For the purpose of this thesis the block length was selected after a sensitivity analysis. It must be reminded that the optimum block length depends on the number of samples composing the original signal in the interval considered, hence it depends on the sampling frequency. In figure 5.10 the block length is selected for an original signal sampled at the frequency of 1 MHz resulting in 100000 samples for the 0.1 seconds of test. The number of samples b composing each block is selected as the lower number of samples, above which the length scales, calculated as described in section 4.3, does not change. This indicates a full convergence of the power spectra. For the case proposed in figure the number of elements per block was found to be slightly higher than 10000. For the case in which the sampling frequency was 120 kHz – hence the number of samples resulted to be

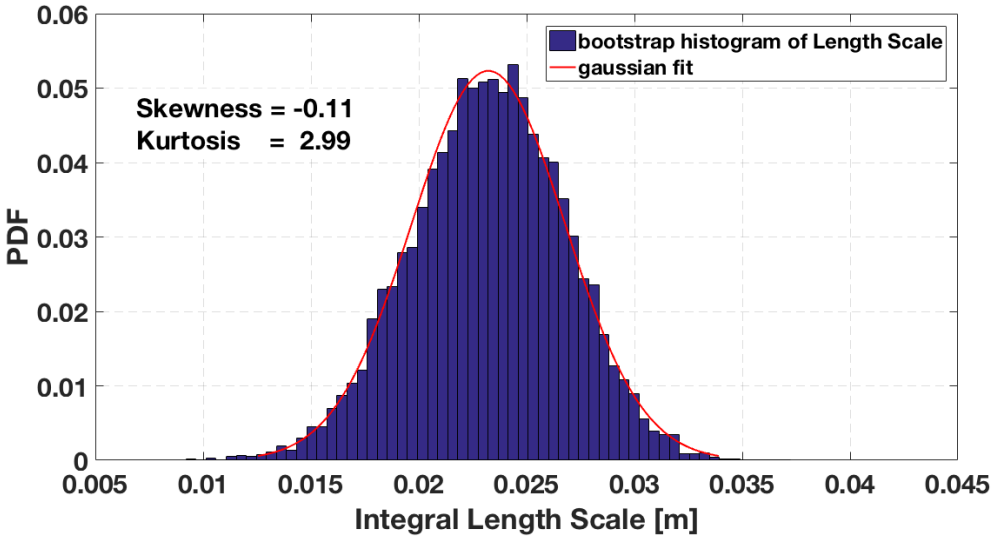

Figure 5.11: Histogram of bootstrapped Integral Length Scale

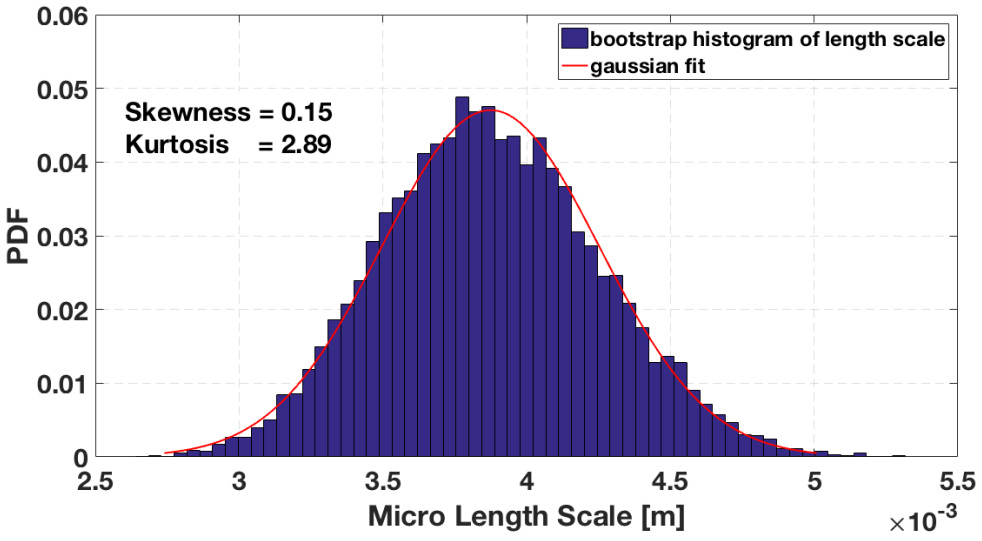

Figure 5.12: Histogram of bootstrapped Micro Length Scale

12000 for the 0.1 seconds of the test – the optimum block length was found to be slightly higher than 1200 confirming the ratio $b/N \approx 1/10$.

The histogram resulting from the bootstrapped integral length scale and micro length scales are shown in figures 5.11 and 5.12.

Again the empirical density function can be fitted with a Gaussian probability density function with good agreement.

5.2.3 Bootstrapped Confidence Interval

An interval estimate is often more useful than just a point estimate. When taken together, the point and the interval estimate give a full information of what is the best guess for the property θ. Given a mean estimate $\overline{\theta}$ and a standard error estimate σ the expression of confidence interval is given as

$$\overline{\theta} \pm t \times \sigma \tag{5.17}$$

where t is a proportional constant and it depends on the confidence level with which this information is given. The confidence level is given in terms of percentage, e.g. for a Student-t distribution the confidence interval is given with a confidence level of 95% for $t = 2$ if the number of samples is large enough.

Formally when N grows large enough the distribution of θ becomes more and more normal with mean $\overline{\theta}$ and variance σ^2. The normal distribution is often written as $\mathrm{N}_\theta\big(\overline{\theta}, \sigma^2\big)$ or by pivotal quantity

$$z = \frac{\theta - \overline{\theta}}{\sigma} \approx \mathrm{N}_z\big(0, 1\big) \tag{5.18}$$

This is valid for a number of sample $N \to \infty$. When a finite number of samples is present then z is substituted with t, standing for the pivotal quantity of a Student-t approximation. The $100\alpha_{th}$ percentile point of a Student-t distribution is then known, e.g. for $\alpha = 0.025$, then $t = -2$ and symmetrically for $\alpha = 0.975$, then $t = +2$. Tables are available for all values of α. Therefore, the information of the estimate of θ is given in a full satisfying way as

$$\overline{\theta} \pm |t^\alpha| \times \sigma \tag{5.19}$$

with $100\big(1 - 2\alpha\big)\%$ confidence level.

When using the Bootstrap technique, we get an approximation of the empirical density function. For this PDF the confidence intervals can be computed in two most common ways as described by Efron [29].

1. The first method is similar to a Student-t approximation. Indeed it is available a table for the pivotal quantity of the so called *Bootstrap-t* distribution. The pivotal quantity for the bootstrapped statistic is represented by the Bootstrap approximation of the Student-t distribution. For more details see Efron (p.160) [29]. Although it is valid also for not symmetrical distribution, difficulties arise for more complicated statistics for which a simple formula for the standard error does not exist.

2. The second method is based on the construction of the bootstrapped histogram for each statistic and compute the confidence interval from it. This

•	$\overline{\mathrm{V}}$ [m/s]	T_u [%]	L [mm]	λ [mm]
Student-t dist.	[43.4 ÷ 46.3]	[12.3 ÷ 15.3]	[10.7 ÷ 24.6]	[2.3 ÷ 3.1]
Boot. Percentile	[43.4 ÷ 46.2]	[12.4 ÷ 15.3]	[10.9 ÷ 24.3]	[2.3 ÷ 3.1]

Table 5.1: Comparison between Student-t distribution and percentile Bootstrap to compute confidence interval with 95% confidence level for mean velocity, turbulence intensity, integral and micro length scale

method, called *percentile Bootstrap*, is more straightforward than the first one and it consists in creating the cumulative distribution function $\hat{\mathrm{G}}$ for the bootstrapped statistic θ^*. The $1-2\alpha$ percentile interval is simply defined as the α and $1-\alpha$ percentile of $\hat{\mathrm{G}}$. Although simple, the main disadvantage of this method is that it performs well only for symmetrical Bootstrap empirical density function for which a Gaussian fit is applicable, hence the percentile Bootstrap confidence interval of the Bootstrap distribution is roughly equal to the one derived from its Gaussian fit.

In the present work all the bootstrapped statistic of interest show an asymptotic tendency to normality, and the confidence interval can be computed with the second methodology, as long as the length of the Bootstrap series B is higher than a certain value, that is $B \geq 200$ for the mean confidence interval, $B \geq 4000$ for the turbulence intensity and $B \geq 10000$ for the length and time scales.

A comparison between the percentile Bootstrap method and the Student-t distribution for computing the confidence interval with 95% confidence level is given in table 5.1 for one test, as an example, with good agreement.

5.2.4 Uncertainty Results

The results for the measurements taken at the inlet of the CT3 VKI's high pressure turbine stage are then expressed with their uncertainty at 95% confidence level in terms of mean velocity $\overline{\mathrm{V}}$, turbulence intensity T_u, integral length scale L and micro length scale λ as shown in figures 5.13, 5.14, 5.15 and 5.16.

The total uncertainty is computed as the root mean square of the random uncertainty derived from the Bootstrap technique and the systematic uncertainty which is affected especially by the error in the total temperature.

It is possible to notice a higher uncertainty in mean velocity and turbulence intensity close to the wall, due to the highest uncertainty of total temperature in that region, and where the highest unsteadiness in the flow is present, that is where shear stresses are more important and integral length scales are smaller.

While systematic uncertainty has a relatively high weight in mean velocity and in turbulence intensity, integral and micro length scales uncertainties are more

affected by random error sources. The high value of uncertainty in the integral length scale may depend on the short time interval in which the measures are acquired.

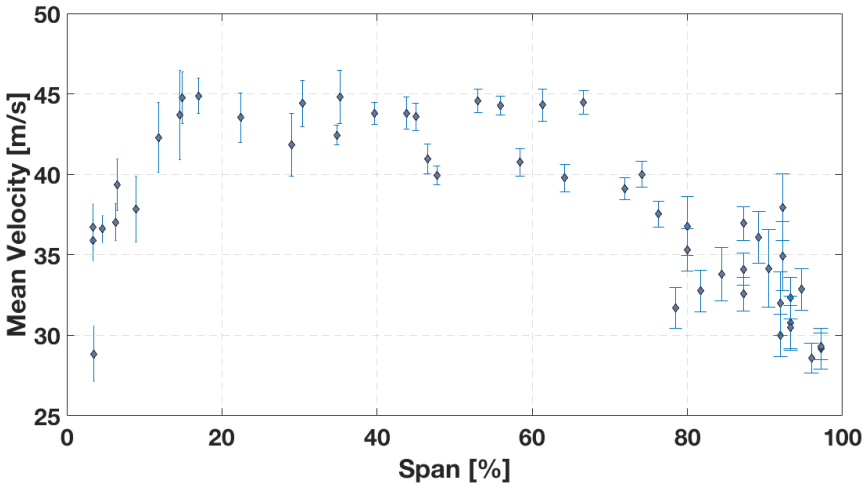

Figure 5.13: Mean Velocity distribution along the blade height with its uncertainty at 95% confidence level

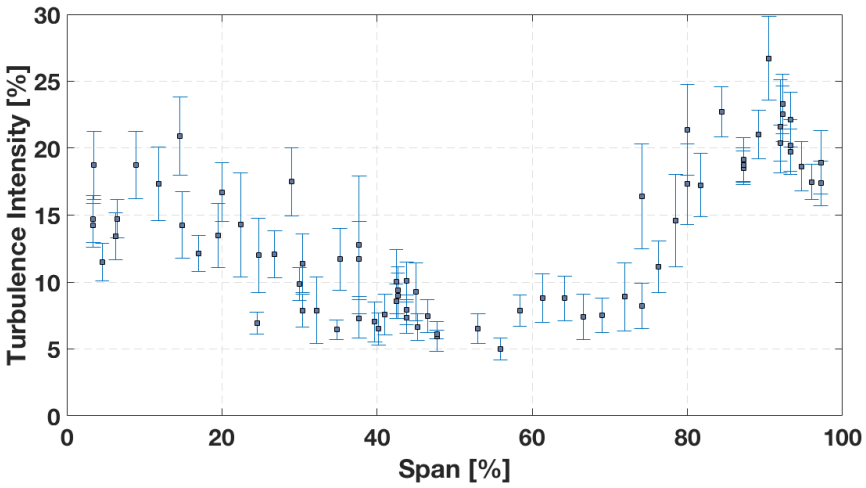

Figure 5.14: Turbulence Intensity distribution along the blade height with its uncertainty at 95% confidence level

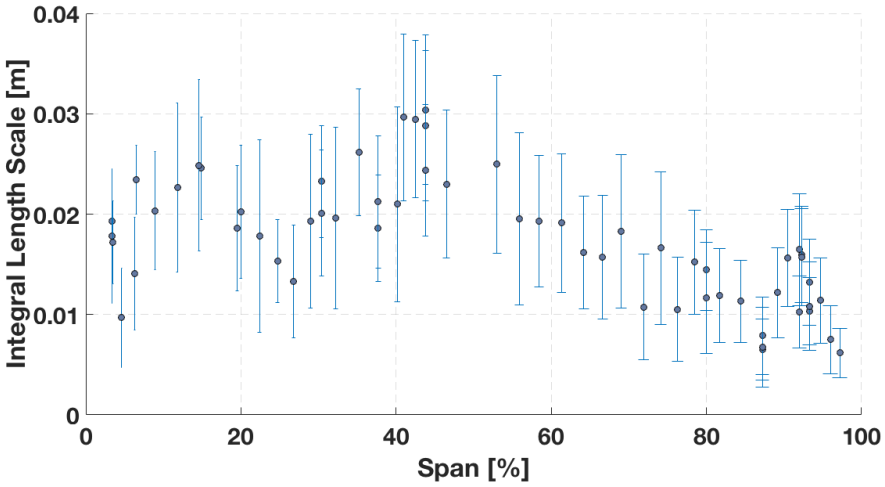

Figure 5.15: Integral Length Scale distribution along the blade height with its uncertainty at 95% confidence level

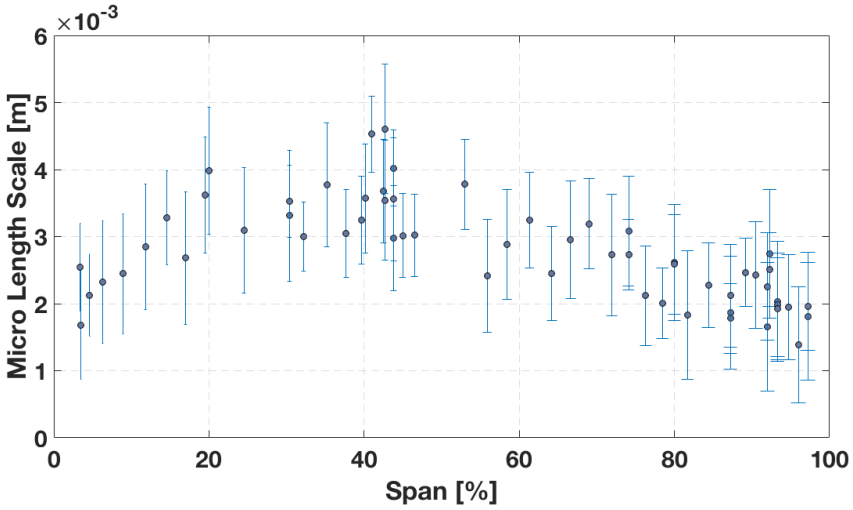

Figure 5.16: Micro Length Scale distribution along the blade height with its uncertainty at 95% confidence level

Chapter 6

Conclusions

Hot-wire anemometry operated in constant temperature mode was employed for measurements in the VKI's CT3 blow-down compression tube facility in order to characterize the flow-field at the inlet of a high pressure turbine stage in terms of turbulence intensity, integral length scales and micro length scales.

A dimensionless approach to the calibration was used in order to decouple the temperature dependency on hot-wire raw voltage results from the mass flux dependency. This allowed to reduce measurements data from a unique calibration curve also for strongly not-isothermal flows as the one encountered in the CT3 facility.

The work done aimed to give accurate turbulence results in order to provide CFD with reliable boundary conditions for validation and help in the design process of highly performing blade tip geometry. In experimental investigations, where the true measured value is never a priori known, accuracy is only achievable when results are associated with error estimations.

The uncertainty was computed by means of the ASME approach, which divides the error sources in systematic and random. The systematic error sources do not affect the distribution of a given population, while the random error sources is accounted by the standard deviation of the statistic probability density function.

However, quantification of the random uncertainty for turbulence measures is not straightforward, since it is not possible to know probability distribution for statistical moments of order higher than the first. For this reason, it is common practice to deal with it by means of a parametric approach. Therefore, any turbulent statistics may be accounted with the assumption that the said statistic population follows a Gaussian distribution, or, alternatively, the probability density function can be assumed to be the one that maximizes the statistical entropy.

Instead, in the present work a non-parametric approach was used by means of the Bootstrap re-sampling technique.

The main strength of the Bootstrap method is that it is asymptotically con-

sistent, that is, when the number of Bootstrap repetition is big enough, the bootstrapped statistic's distribution approximates the measured statistic's distribution without needing to know it in advance. Thus, it is possible to compute statistical inference without any assumption on the probability density function.

In correlated samples, the Moving Block Bootstrap (MBB) performs as well as the standard Bootstrap, but, in addition, it prevents to destroy the autocorrelation.

The bootstrapping procedure has shown a tendency to normality for a number of Bootstrap repetitions $B \geq 200$ for the mean, $B \geq 4000$ for the turbulence intensity and $B \geq 10000$ for the length and time scales confidence intervals.

The block length was selected either by an automatic algorithm or by a sensitivity analysis. For highly correlated structures, or for flows with strongly oscillating autocorrelation function, the sensitivity analysis assured more reliability since the automatic algorithm is based on a previous estimation of time scale from the autocorrelation function itself. A good value for b was found to be slightly higher than 1/10 times the original sample size N.

Thanks to the resulting symmetry of the bootstrapped PDF, the inference is given by the percentile Bootstrap method, for which a 95% confidence level is taken from the cumulative distribution function $\hat{\mathrm{G}}$ of the bootstrapped statistic of interest and the $1-2\alpha$ percentile interval is simply defined by the $\left[\alpha B\right]_{th}$ and the $\left[\left(1-\alpha\right)B\right]_{th}$ sample of $\hat{\mathrm{G}}$. This was found to agree with the uncertainty computed from the classic Student-t distribution methodology.

Finally, results in terms of mean velocity, turbulence intensity, integral length scale and micro length scale are conferred and displayed along all the blade height with the respective uncertainty with 95% confidence level.

6.1 Future Recommendation

The Bootstrap technique applied in the present work has demonstrated to be efficient with a good degree of repeatability. Nevertheless, validation of the method has to be provided with other more validated non-parametric techniques such as a classic Monte Carlo simulation in which all parameters involved in the data reduction are fed in the Monte Carlo computer-based algorithm.

Appendix A

Uncertainty of Calibration Instruments

A.1 Thermocouple Uncertainty

Uncertainty is evaluated as the root mean square of systematic and random error sources. The K-type thermocouple is calibrated with a Thermibel oil bath and a Thermibel high precision digital thermometer as a reference.

The manufacturer indicates an uncertainty in the reference thermometer of $b_1 = 0.02$ K full scale, while the resolution of the instrument is up to the third decimal digit.

Resolution errors, which derive from the round-off of the fourth decimal digit, is computed with a uniform distribution with infinite degree of freedom. Thus it is $b_2 = 0.001/\sqrt{3} = 0.00058$ K.

Systematic uncertainty is

$$b_{T_0} = \sqrt{b_1^2 + b_2^2} \approx 0.02K \tag{A.1}$$

Random uncertainty is evaluated as the standard deviation of the samples in terms of the thermocouple voltage acquired at a sampling frequency of 10 kHz for 3 seconds. Given the high number of samples a Gaussian distribution is ensured with degrees of freedom much higher than 30, hence

$$s_E = \sqrt{\frac{\sum_{i=1}^{N} \left(\mathrm{E}_i - \overline{\mathrm{E}}\right)^2}{N-1}} \tag{A.2}$$

The calibration curve obtained is a linear fitting of the calibrated points in a Voltage-Temperature graph of figure 2.10b with angular coefficient m and intercept

q. Temperature random uncertainty is then computed by propagation as $s_1 = s_{\mathrm{E}}\delta \mathrm{T}_0/\delta \mathrm{E} = s_E m$.

To evaluate the quality of the fitting curve the standard estimate of error is used as

$$SEE_{T_0} = \sqrt{\frac{\sum_{i=1}^{N_{cal}} \left(\mathrm{T}_0, i - \mathrm{T}_{0,fit,i}\right)^2}{N-K}} \tag{A.3a}$$

$$s_2 = \frac{SEE_{T_0}}{\sqrt{N_{cal}}} \tag{A.3b}$$

where K is the number of coefficient of the calibration curve, hence $K = 2$, and N_{cal} is the number of calibrated points composing the fitting curve.

The total random error source is

$$s_{T_0} = \sqrt{s_1^2 + s_2^2} \approx 0.156K \tag{A.4}$$

Total uncertainty for the thermocouple and its expansion value at 95% confidence level are then

$$U_{T_0} = \sqrt{s_{T_0}^2 + b{T_0}^2} \approx 0.157K \tag{A.5a}$$

$$U_{T_0,95} = 2U_{T_0} \approx 0.314K \tag{A.5b}$$

A.2 Validyne Pressure Transducer Uncertainty

The same procedure is used to evaluate the uncertainty of the Validyne pressure transducer, which is calibrated with a DPI pressure pump with a manufacturer indication of uncertainty equal to 0.025% of Full Scale, which is 7000 Pa. Resolution of the digital pump is 0.001 Pa and it is treated with an uniform distribution and infinite degrees of freedom.

The systematic uncertainty is equal to $b_{p_0} \approx 1.75$ Pa.

The calibration curve is again a linear fitting of the calibrated points in the Voltage-Pressure graph of figure 2.10a.

By applying the same procedure used for the thermocouple for the standard estimate of error SEE_{p_0} and the same sampling frequency of 10 kHz for 3 seconds the final random uncertainty will be equal to $s_{p_0} \approx 6.55$ Pa.

The total uncertainty is then $U_{p_0} \approx 6.78$ Pa and the 95% confidence level extension is again computed as

$$U_{p_0,95} = 2 \times \sqrt{s_{p_0}^2 + b_{p_0}^2} \approx 13.56Pa \tag{A.6}$$

A.3 Error Propagation Analysis for Hot-Wire Calibration

In equations 5.5 and 5.6 the uncertainty for the Nusselt number and the Reynolds number is computed by propagation of other measured quantities' uncertainty. Here all the formulations are provided.

The partial derivative terms of equation 5.5 are

$$\frac{\delta Nu}{\delta \mathrm{E}_b} = \frac{2\mathrm{E}_b\mathrm{R}_w}{\left(\mathrm{R}_l + \mathrm{R}_t + \mathrm{R}_w\right)^2 \kappa l_w \pi \left(\mathrm{T}_w - \eta \mathrm{T}_0\right)} \tag{A.7a}$$

$$\frac{\delta Nu}{\delta \mathrm{T}_0} = \frac{\mathrm{E}_b^2\mathrm{R}_w\eta}{\left(\mathrm{R}_l + \mathrm{R}_t + \mathrm{R}_w\right)^2 \kappa l_w \pi \left(\mathrm{T}_w - \eta \mathrm{T}_0\right)^2} \tag{A.7b}$$

$$\frac{\delta Nu}{\delta \eta} = \frac{\mathrm{E}_b^2\mathrm{R}_w\mathrm{T}_0}{\left(\mathrm{R}_l + \mathrm{R}_t + \mathrm{R}_w\right)^2 \kappa l_w \pi \left(\mathrm{T}_w - \eta \mathrm{T}_0\right)^2} \tag{A.7c}$$

$$\frac{\delta Nu}{\delta \kappa} = -\frac{\mathrm{E}_b^2\mathrm{R}_w}{\left(\mathrm{R}_l + \mathrm{R}_t + \mathrm{R}_w\right)^2 \kappa^2 l_w \pi \left(\mathrm{T}_w - \eta \mathrm{T}_0\right)} \tag{A.7d}$$

While the partial derivative terms of equation 5.6 are

$$\frac{\delta Re}{\delta \rho} = \frac{\mathrm{V} d_w}{\mu} \tag{A.8a}$$

$$\frac{\delta Re}{\delta \mu} = -\frac{\mathrm{V} d_w \rho}{\mu^2} \tag{A.8b}$$

$$\frac{\delta Re}{\delta \mathrm{V}} = \frac{d_w \rho}{\mu} \tag{A.8c}$$

Uncertainty for flow properties is given by propagation of error starting from the three measured quantities: total temperature, total pressure and static pressure. Static pressure is the ambient one during calibration and its uncertainty is neglected.

In order to compute the Reynolds number uncertainty, it is required uncertainty in viscosity, density and velocity. The viscosity is a function of the total pressure, hence its uncertainty will be

$$\frac{\delta mu}{\delta \mathrm{T}_0} = \frac{3\mu_{ref}\left(\mathrm{T}_s + \mathrm{T}_{ref}\right)}{2\mathrm{T}_{ref}\left(\mathrm{T}_0 + \mathrm{T}_s\right)} \left(\frac{\mathrm{T}_0}{\mathrm{T}_{ref}}\right)^{1/2} - \frac{\mu_{ref}\left(\mathrm{T}_s + \mathrm{T}_{ref}\right)}{\left(\mathrm{T}_0 + \mathrm{T}_s\right)^2} \left(\frac{\mathrm{T}_0}{\mathrm{T}_{ref}}\right)^{3/2} \tag{A.9a}$$

$$U_\mu = \frac{\delta mu}{\delta \mathrm{T}_0} U_{T_0} \tag{A.9b}$$

As far as the density is concerned, the only variable which participates at the propagation is the static temperature.

$$\frac{\delta\rho}{\delta \mathrm{T}} = -\frac{\mathrm{p}}{R\mathrm{T}^2} \tag{A.10a}$$

$$U_\rho = \frac{\delta\rho}{\delta \mathrm{T}} U_T \tag{A.10b}$$

Static temperature is computed from the Mach number and the total temperature,

$$\frac{\delta \mathrm{T}}{\delta \mathrm{T}_0} = \frac{1}{\frac{\gamma-1}{2}M^2+1} \tag{A.11a}$$

$$\frac{\delta \mathrm{T}}{\delta M} = -\frac{2M\mathrm{T}_0\frac{\gamma-1}{2}}{\left(\frac{\gamma-1}{2}M^2+1\right)^2} \tag{A.11b}$$

$$U_T = \sqrt{\left(\frac{\delta \mathrm{T}}{\delta \mathrm{T}_0}U_{T_0}\right)^2 + \left(\frac{\delta \mathrm{T}}{\delta M}U_M\right)^2} \tag{A.11c}$$

Moreover, the uncertainty in the computed velocity is function of error propagation from Mach number and static temperature

$$\frac{\delta \mathrm{V}}{\delta M} = \left(\gamma R\mathrm{T}\right)^{1/2} \tag{A.12a}$$

$$\frac{\delta \mathrm{V}}{\delta \mathrm{T}} = \frac{\gamma R M}{2\left(\gamma R\mathrm{T}\right)^{1/2}} \tag{A.12b}$$

$$U_V = \sqrt{\left(\frac{\delta \mathrm{V}}{\delta M}U_M\right)^2 + \left(\frac{\delta \mathrm{V}}{\delta \mathrm{T}}U_T\right)^2} \tag{A.12c}$$

The Mach number is computed as function of total pressure, hence

$$\frac{\delta M}{\delta \mathrm{p}_0} = \frac{\left(\frac{\mathrm{p}_0}{\mathrm{p}}\right)^{\frac{\gamma-1}{\gamma}-1}}{\gamma\mathrm{p}\left[\left(2\left(\frac{\mathrm{p}_0}{\mathrm{p}}\right)^{\frac{\gamma-1}{\gamma}}-2\right)\frac{1}{\gamma-1}\right]^{1/2}} \tag{A.13a}$$

$$U_M = \frac{\delta M}{\delta \mathrm{p}_0}U_{p_0} \tag{A.13b}$$

As far as the Nusselt number uncertainty is concerned, the flow conductivity and the recovery factor uncertainty must still be calculated. The flow conductivity is function of the total temperature and its uncertainty is

$$\frac{\delta\kappa}{\delta \mathrm{T}_0} = \frac{7\kappa_{ref}}{10\mathrm{T}_{ref}}\left(\frac{\mathrm{T}_0}{\mathrm{T}_{ref}}\right)^{-3/10} \tag{A.14a}$$

$$U_\kappa = \frac{\delta\kappa}{\delta \mathrm{T}_0} U_{T_0} \tag{A.14b}$$

Finally, uncertainty in the recovery factor η is found to be on the order of 10^{-7}, hence negligible.

As explained in section 5.1 the final Reynolds number uncertainty has three contributions, one deriving from error propagation of the fitted curve with respect to the Nusselt number uncertainty, one derived from the quality of the fitting by means of the standard estimate of error and one derived form error propagation of the other measured quantities from which the Reynolds number is calculated. The latter gives the highest uncertainty.

In particular, for the first hot-wire HWA1 it is $U_{Re,fit} \approx 0.120$, $s_{\overline{Re}} \approx 0.003$ and $U_{Re,meas} \approx 0.229$. The total uncertainty is $U_{Re} \approx 0.231$. For the second hot-wire HWA2 it is $U_{Re,fit} \approx 0.124$, $s_{\overline{Re}} \approx 0.012$, $U_{Re,meas} \approx 0.157$, $U_{Re} \approx 0.161$. Thus the extended uncertainty with 95% confidence level is

$$U_{Re,95}^{HWA1} \approx 0.461 \tag{A.15a}$$

$$U_{Re,95}^{HWA2} \approx 0.322 \tag{A.15b}$$

References

[1] G. Biswas and V. Eswaran. Turbulent flows: Fundementals, experiments and modeling. *Pangbourne, Alpha Science International Ltd*, 2002.

[2] Xiao and Xinwen. *Investigation of tip clearence flow physics in axial flow turbine rotors*. PhD thesis, The Pennsylvania State University, 2001.

[3] Z. Wang, Z. Liu, and Z. Feng. Influence of mainstream turbulence intensity on heat transfer characteristics of a high pressure turbine stage with inlet hot streak. *Journal of Thurbomachinery*, 138, 2016.

[4] B. Cukurel, S. Acarer, and T. Arts. A novel perspective to high-speed cross-hot-wire calibration methodology. *Exp Fluids*, 53:1073–1085, 2012.

[5] S. Acarer. Two-dimensional hot-wire anemometry in high speed flow, 2011.

[6] D. Favier. The role of wind tunnel experiments in cfd validation. *Encyclopedia of Areospace Engineering*, 2010.

[7] J. Meng, E. Tabosa, W. Xie, and K. Runge. A review of turbulence measurements techniques for flotation. *Minerals Engineering*, 95:79–95, 2016.

[8] R. G. Seasholtz. Laser doppler velocimeter measuraments in a turbine stator cascade facility. Technical report, Lewis Research Center Cleveland, Ohio, 1974.

[9] M. Carbonaro. Hot-wire measurements. in "introduction to measurement techniques in fluid dynamics". Technical report, Von Karman Institute for Fluid Dynamics, 2012.

[10] H. H. Bruun. *Hot-Wire Anemometry, Principles and Signal Analysis*. Oxford Science Publication, 1995.

[11] P. C. Stainback and K. A. Negabushana. Review of hot-wire anemoetry technique and the range of their applicability for various flows. *Electronic Journal of Fluids Engineering, Transactions of the ASME*, 1994.

[12] C. F. Dewey. A correlation of convective heat transfer and recovery temperature data for cylinders in compressible flow. *International Journal of Heat and Mass Transfer*, 8:245–252, 1965.

[13] G. Comte-Bellot. Hot-wire anemometry. Technical report, Ecole Centrale de Lyon, 2013.

[14] T. Yasa, G. Paniagua, and R. Denos. Hot wire anemometry for non-isothermal flows and effect of "aging" of the sensor wire. Technical report, Von Karman Institute for Fluid Dynamics, 2015.

[15] D. Jung, S. Gamard, and W. K. George. Downstream evolution of the most energetic modes in a turbulent axisymmetric jet at high reynolds number. part 1. the near-field region. *J. Fluid Mechanics*, 514:173–204, 2004.

[16] A. Van Hirtum and X. Grandchamp. Near field round jet flow downstream from an extended abrupt contraction nozzle. *14th European Turbulence Conference*, 2013.

[17] C. H. Sieverding and T. Arts. The vki compression tube annular cascade facility ct3. *ASME*, 1992.

[18] G. Paniagua, C.H. Sieverding, and T. Arts. Review of the von karman institute compression tube facility for turbine research. *Proceedings of ASME Turbo Expo*, 2013.

[19] D. M. Garcia. Experimental investigation of rotor tip flows, 2016.

[20] S. B. Pope. *Turbulent Flows*. Cambridge University Press, 1998.

[21] D. H. Lenschow, J. Mann, and L. Kristensen. How long is long enough when measuring fluxes and other turbulent statistics? *American Meteorological Society*, 1994.

[22] A. Drozdz. Influence of pressure gradient on streamwise skewness factor in turbulent boundary layer. In *Fluid Mechanics conference*, 2014.

[23] P. L. O'Neill, D. Nicolaides, and J. Soria D. Honnery. Autocorrelation function and the determination of integral length with reference to experimental and numerical data. *15th Australasian Fluid Mechanics Conderence*, 2004.

[24] J. Lewalle and D. E. Ashpis. Estimation of time scales in unsteady flows in a turbomachinery rig. *NASA/TM*, 2004.

[25] P. E. Roach. The generation of nearly isotropic turbulence by means of grids. *Advanced research laboratory Rolls-Royce*, 1986.

[26] L. A. El-Gabry, D. R. Thurman, and P. E. Poinsatte. Procedure for determining turbulence length scales using hotwire anemometry. *NASA/TM*, 2014.

[27] G. Dell'Era, M. Mersinligil, and J. F. Brouckaert. Assessment of unsteady pressure measurement uncertainty part 1: Single sensor probe. *Proceeding of the ASME Turbo Expo*, 2015.

[28] R. W. Derksen ans P.J. Sullivan. Moment approximations for probability density functions. *Combustion and Flame*, 1990.

[29] B. Efron. Bootstrap methods: Another look at the jackknife. *Annals of Statistics*, 1979.

[30] H. R. Künsch. The jackknife and the bootstrap for general stationary observations. *Annals of Statistics*, 1989.

[31] B. Efron and R. J. Tibshirani. *An Introduction to Bootstrap*. Chapman and Hall, 1993.

[32] L. H. Benedict and R. D. Gould. Towards better uncertainty estimates for turbulence statistics. *Experiments in Fluids*, 22:129–136, 1996.

[33] C. M. Garcia and P. R. Jackson. Confidence intervals in the determination of turbulence parameters. *Experiments in Fluids*, 40:514–522, 2006.

[34] R. Theunissen. *Adaptive Image Interrogation for PIV*. PhD thesis, Von Karman Institute for Fluid Dynamics, 2010.

[35] D. N. Politis and H. White. Automatic block-length selection for the dependent bootstrap. *Econometric Reviews*, 23(1):53–70, 2004.